INSTITUTE
FOR
AEROSPACE STUDIES

UNIVERSITY OF TORONTO

ELECTRON BEAM STUDIES OF THE DIFFUSIVE SEPARATION OF HELIUM-ARGON MIXTURES IN FREE JETS AND SHOCK WAVES

by

Dietmar E. Rothe

JULY 1966

UTIAS REPORT NO. 114

DISCLAIMER NOTICE

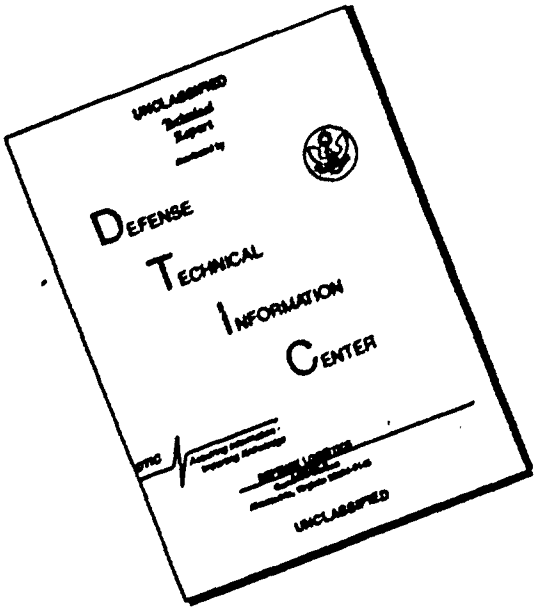

UNCLASSIFIED
Technical
Report

DEFENSE
TECHNICAL
INFORMATION
CENTER

DTIC

UNCLASSIFIED

ELECTRON BEAM STUDIES OF THE DIFFUSIVE SEPARATION OF HELIUM-ARGON MIXTURES IN FREE JETS AND SHOCK WAVES

by

Dietmar E. Rothe

Manuscript received May 1966

JULY 1966 UTIAS REPORT NO. 114

ACKNOWLEDGEMENTS

My personal thanks are expressed to Dr. G. N. Patterson, who provided the opportunity and the facilities for carrying out this research, and to Dr. J. H. de Leeuw, who suggested the problem in the first place and who contributed to this work through many enlightening discussions.

The assistance received from Mr. P.V. Marrone during the experiments is most gratefully acknowledged.

Thanks are also due to Mr. J.L. Bradbury of the Institute's shop staff for the care and precision applied to the construction of the electron gun system.

I am most grateful to my wife, Gerda, for preparing some of the figures of this report and for her continued encouragement.

This research was supported by the Defence Research Board of Canada under Grant No. 9551-02 and by the United States Air Force Office of Scientific Research under Grant No. AF-AFOSR-276-65.

SUMMARY

A narrow electron beam was used to selectively determine the component densities in rarefied helium-argon flows by spectrally analyzing the beam's luminescence. After a systematic study of the electron beam fluorescence in helium and argon had been made in a series of preliminary experiments, point-by-point measurements were made along and off the axes of underexpanded free jets and through normal shock waves produced by shock holders placed in the jets. Various argon mole fractions were used, and the jet Reynolds numbers ranged from 100 to 10,000. The argon enrichment found along the jet axis agrees well with a theory recently proposed by F. S. Sherman. Off axis tests show an argon deficiency near the jet boundary. The experimental shock profiles agree only qualitatively with one-dimensional theories. Radial diffusion destroyed the otherwise approximate one-dimensionality of the shock waves, resulting in a significant argon enrichment inside the partially stagnated shock holder.

TABLE OF CONTENTS

NOTATION

a	speed of sound
C	correction coefficient in the viscosity law (defined by Eq. 8)
D	orifice diameter
D_{12}	binary diffusion coefficient
E	Sherman's diffusion parameter (defined by Eq. 7)
f	mole fraction of the heavy species
I_b	electron beam current
I_{ph}	anode current of photomultiplier
m	atomic or molecular mass
M	Mach number
n	number density of atoms or molecules
p	gas pressure
r	radial distance measured from the axis of a free jet
R	radius of a hemispherical surface centered at the orifice
Re_o	Reynolds number based on the orifice diameter and the stagnation chamber properties of the gas
Re_r	Reynolds number based on the radius of shock curvature and the free stream properties of the gas
s	distance along a streamline
$\underline{s}$	unit vector pointing in the streamline direction
S	continuous surface everywhere normal to the streamlines
Sc_o	Schmidt number based on the stagnation chamber properties of the gas ($Sc_o \equiv \mu_o/\rho_o D_{12}$)
T	gas temperature (absolute)
$\underline{u}$	center of mass velocity of an element of gas
$\underline{v_1}$	diffusion velocity of the heavy species (defined by Eq. 3)
$\dot{V}$	volumetric pumping speed of the tunnel
x	distance along the axis of a free jet measured from the center of the sonic orifice

x_o	location of hypothetical source of the free jet expansion
x_M	axial distance to the center of the Mach disc
x'	distance normal to shock wave measured from center of shock
α	thermal diffusion factor
γ	ratio of specific heats of a gas
δ	shock thickness
δ_s	shock thickness based on the maximum slope of the density profile
ϵ	ratio of the pressure behind the Mach disc to the ambient pressure
λ	wave length of light
λ_1	"Molecular mean free path" ahead of the shock (defined by Eq.14)
μ	viscosity of the gas
ρ	mass density of the gas
ϕ	molecular number flux fraction of the heavy species (defined by Eq. 5)

Subscripts

o	stagnation chamber conditions
*	sonic conditions
∞	test section conditions outside of the free jet
A	argon
H	helium

As applied to the free jet

1	refers to the heavy species,
2	refers to the light species .

As applied to the shock wave

1	refers to the free stream conditions upstream of the shock,
2	refers to the conditions downstream of the shock.

I. INTRODUCTION

In the general field of experimental supersonic gas dynamics there occur many instances in which gas mixtures are subjected to severe accelerations and decelerations. Under these conditions the resulting gas dynamic forces are able to support large pressure gradients, accompanied by corresponding temperature and density gradients. In many cases these gradients can become quite significant over the distance of a molecular mean free path, and diffusion effects, in particular those resulting from barodiffusion, can no longer be ignored and must be included in a general description of the flow structure. Typical examples are gas dynamic shock waves and Prandtl-Meyer expansion fans in a rarefied gas mixture.

Since planetary atmospheres, in which aircraft and spacecraft have to operate, consist of mixtures of various gas components, and since the gases expelled by propulsive devices are generally made up of constituents of widely varying molecular masses, the diffusion phenomena are also of practical interest in aerodynamic problems. For example, the heat transfer to the surface of a re-entering space vehicle, the combustion characteristics of a fuel-air mixture in a supersonic flow, or the thrust characteristics of a reaction jet (rocket exhaust), are all influenced by the distribution of the gas components in the relevant gas mixture.

The present report concentrates on two specific flow configurations; the gas dynamic shock and the underexpanded free jet issuing from a circular sonic orifice. Binary gas mixtures of non-reacting inert components were used throughout. Helium and argon were chosen, because these gases are readily available, and because their atomic masses differ by a factor of ten. As will be shown in Section II a large mass difference of the atomic species makes the barodiffusion effects correspondingly large and easily detectable.

Whereas the structure of the underexpanded free jet and that of the one-dimensional shock wave in pure gases are reasonably well understood, the same cannot be said for the case of gas mixtures. Experimental investigations of the species separation in the free jet have been performed in the past for two reasons. One is the prospect of separating isotope mixtures; the other the possibility of generating high energy molecular beams. In the latter case, a light gas is seeded with a small amount of heavy gas. In the process of expansion the heavy molecules reach essentially the adiabatic escape speed of the light gas and, thus, gain a larger directed mass velocity than could be obtained by adiabatically expanding the heavy gas alone. Furthermore, the heavy molecules remain on the average closer to the jet axis than the light molecules. By introducing a suitably designed stripping baffle into the flow, the jet core, which is enriched in the high energy molecules of the heavy type, can be isolated for use in molecular beam experiments. The arrangement, consisting of a skimmer in a free jet, has also been proposed for separating isotopes.

In order to determine the most efficient combination of jet parameters and stripping baffle design and location for the purpose of isotope separation or molecular beam generation, previous experimenters used a mass spectrometer to determine the composition of the gas extracted from various regions in the free jet by means of a sampling probe or skimmer, with the hope of gaining an understanding of the diffusive separation occurring in the free jet itself. The results obtained in this fashion by Becker, Bier and Burghoff (Ref. 1) and by Waterman and Stern (Refs. 2 and 3), who compared the composition in the jet core behind the skimmer with that in the jet periphery, gave an inconsistent picture of the actual free jet separation. This is so partly because the samples were taken from a finite cross-section of the jet over which the gas composition was not constant. The measured composition, therefore, represented an average value in this case, and could not easily be related to the actual composition at any specific point in the free jet. Chow (Ref. 4), who used a small diameter sampling probe, found the gas enriched in the heavy species at all points in the free jet. This contradicted the measurements reported in Refs. 1 to 3. It is now generally believed, and the present work lends strong support to this view, that Chow's separation results were probe induced. In fact, Chow has recently shown (Ref. 5) that a curved shock, standing in front of the sampling tube, could account for the results obtained in his earlier experiments. Reis and Fenn (Ref. 6) came to the same conclusion after performing some sampling probe tests of their own. It is also suspected that the compositions measured behind skimmers in Refs. 1 to 3 were influenced by the skimmer interacting with the supersonic flow. In the present experiments all probe induced effects were avoided by analyzing the gaseous luminescence, induced by a thin 17.5 kv, 100μamp electron beam, for the determination of the component densities in the undisturbed free jet.

Recently there have appeared in the literature several attempts to give a quantitative theoretical account of the species separation in a free jet. Of these the papers by Zigan (Ref. 7) and Sherman (Ref. 8) are of interest here. In Zigan's work the results are given in integral form and allow a comparison with skimmer experiments (e.g. Refs.1 to 3). The agreement is poor; presumably because of flow disturbances introduced by the skimmer. The results of the present experiments can most readily be compared with Sherman (Ref. 8), who gives an expression for the mole fractions along the axis of symmetry of the free jet. This is done in Section VII of this report.

The structure of the one-dimensional normal shock wave in a binary gas mixture has been treated theoretically by several authors (Refs. 9 to 11). Both continuum flow concepts and kinetic theory have been applied to the problem. So far no experimental tests have been reported for the shock wave structure in gas mixtures.

The motivations for the work reported here may be summarized as follows:

(1) A non-ambiguous measurement of the diffusive separation in under-expanded free jets was in order to settle the argument as to what species separation exists in the undisturbed free jet.

(2) A direct test of Sherman's theory for the axial variation of the component mole fractions became feasible with the use of the electron beam probe.

(3) Direct experimental evidence of species separation inside shock waves could be obtained and could be compared with existing theories.

(4) By probing shock waves produced in front of a partially choked shock holder, placed in the supersonic flow of the free jet, some additional light could be shed on the "probe induced separation effects".

(5) The results could be expected to have some practical application in the design of gaseous diffusion facilities for isotope separation and in the design of seeded molecular beam devices.

II. THEORETICAL PREDICTIONS

For the isentropic flow of a diatomic gas ($\gamma = 7/5$) the Mach number variation along the axis of the underexpanded free jet, issuing from a sonic orifice, has been calculated by Owen and Thornhill (Ref. 12), using the method of characteristics. More recently similar calculations have been performed for specific heat ratios of 5/3, 7/5, and 9/7 by Wolff and have been reported by Sherman (Ref. 13). These solutions are universally applicable to free jets expanding into an ambient gas at non-zero pressure in the region bounded by the orifice and the first wave front, which registers the existence of an ambient pressure. This wave front is usually well defined by the barrel shock, formed by the coalescing Mach waves reflected from the jet boundary, and by the Mach disc. The Mach disc location is given by an empirical law (Refs. 14 and 15).

$$x_M/D = (2/3)\ (p_o/p_\infty)^{\frac{1}{2}} \quad , \qquad (1)$$

where x_M is the distance from the orifice to the Mach disc, D is the orifice diameter, and p_o and p_∞ are the stagnation chamber pressure and ambient pressure, respectively. A sketch of the general flow configuration of an underexpanded free jet is given in Fig. 2.1.

Once the Mach number is known locally, all other thermodynamic gas properties can be obtained from the isentropic relations in the inviscid case. These show that for distances larger than about two orifice diameters the gas density, ρ (or the molecular number density, n), falls off as $1/(x-x_o)^2$, where x_o is the location of a hypothetical source near the orifice, given by the intersection of the streamline asymptotes with the jet axis (see Fig. 2.1). It should be noted, however, that this variation of the density is not dependent on the flow being isentropic, but is strictly a result of the geometry of the source-flow-like expansion and the fact, that at $x/D = 2$ the velocity has virtually reached its maximum value of the escape speed. For this reason density measurements which agree with the isentropic density profile cannot be used to establish whether the free jet flow is isentropic or not.

In his treatment of the underexpanded free jet of a binary gas mixture Sherman (Ref. 8) combines the continuum flow conservation equations (Navier-Stokes), written for a two component mixture, with the binary diffusion equation based on the Chapman-Enskog theory of diffusion. The latter equation may be written in the form

$$\rho_1 \underline{v}_1 = \frac{m_1 m_2}{m^2}\ \rho D_{12} \left[f(1-f) \left(\frac{m_1 - m_2}{m}\ \nabla \ell n\ p - \alpha\ \nabla \ell n\ T \right) - \nabla f \right] , \qquad (2)$$

where the subscript "1" refers to the heavier species; f is the mole fraction of the heavier species; $m = fm_1 + (1-f)\ m_2$ is the mean molecular mass; D_{12} and α are the binary diffusion coefficient and the thermal diffusion factor, respectively; $\underline{v}_1$ is the diffusion velocity of the heavy species defined by

$$\underline{v}_1 = \underline{u}_1 - \underline{u} \quad , \qquad (3)$$

where $\underline{u}_1$ is the mass velocity of the heavy species and $\underline{u}$ is the center of mass velocity of an element of the gas mixture.

In the free jet expansion and in the shock transition the temperature gradient is in the same direction as the pressure gradient. Thermal diffusion opposes barodiffusion under these circumstances. An order of magnitude analysis of Eq. (2), as applied to the free jet or the shock wave, reveals that barodiffusion is by far the dominant separating agent. In barodiffusion the heavy molecules diffuse towards the high pressure regions. In the free jet, because of the streamline curvature near the orifice, high pressures occur on the jet axis. Radial barodiffusion, therefore, causes an enrichment of heavy molecules along the jet centerline. Once a separation between the component species has taken place, ordinary diffusion tends to homogenize the mixture again.

In order to obtain a solution for the set of equations, Sherman expands all variables in terms of inverse powers of the Reynolds number, based on the stagnation conditions and the orifice diameter: e.g.

$$f = f^{(o)} + f^{(1)}/Re_o + f^{(2)}/Re_o^2 + \dots \quad ,$$

where the jet Reynolds number* is defined by the expression,

$$Re_o = \rho_o \, a_o \, D/\mu_o = m_o \, n_o \, (\gamma R T_o)^{\frac{1}{2}} \, D/\mu_o \quad . \tag{4}$$

In the zeroth approximation the flow is isentropic, and the mixture remains homogeneous. Neglecting all terms of second and higher order Sherman then solves for the first order perturbation terms in the mole fraction, f, and the molecular number flux fraction,

$$\phi \equiv n_1 \, \underline{u}_1 \cdot \underline{s} / (n_1 \underline{u}_1 + n_2 \underline{u}_2) \cdot \underline{s} \quad , \tag{5}$$

along the axis of the jet by integrating the equations along the central streamline ($\underline{s}$ is a unit vector along the streamline). Using the expressions derived in this manner in Ref. 8 the change in the mole fraction of the heavy component along the axis can be written:

$$(f - f_o) \frac{Re_o}{EC} = (\gamma - 1) \left[M^2 \left(1 + \frac{\gamma - 1}{2} M^2\right)^{(5-3\gamma)/2(\gamma-1)} \frac{dM}{d(x/D)} \right.$$

$$\left. - \frac{1}{2} \int_0^M \frac{(M^2 - 1)(3 + M^2)}{M} \left(1 + \frac{\gamma - 1}{2} M^2\right)^{(7-5\gamma)/2(\gamma-1)} \frac{dM}{d(x/D)} \, dM \right] . \tag{6}$$

In this relation M represents the Mach number,

$$E \equiv \frac{f_o (1 - f_o)}{Sc_o} \left[\frac{m_1 - m_2}{m_o} \left(\frac{\gamma}{\gamma - 1} \right) - \alpha_o \right] \quad , \tag{7}$$

---

* The Reynolds number used here is twice that used by Sherman.

and

$$C \equiv \mu_* T_o/\mu_o T_* \approx 1 \quad . \tag{8}$$

The Schmidt number is defined as $Sc_o \equiv \mu_o/\rho_o D_{12}$, and the starred quantities are those at sonic conditions. For a monatomic gas mixture ($\gamma = 5/3$) Eq. (6) reduces to

$$(f-f_o)\,\frac{Re_o}{EC} = \frac{2}{3} M^2 \frac{dM}{d(x/D)} - \int_0^M \frac{M^2 - 1}{M} \frac{dM}{d(x/D)}\, dM \quad . \tag{9}$$

The difference between the molecular number fraction and the number flux fraction on the jet axis is given by

$$(f-\phi)\,\frac{Re_o}{EC} = (\gamma-1)\,\left(1 + \frac{\gamma-1}{2} M^2\right)^{(5-3\gamma)/2(\gamma-1)} \frac{dM}{d(x/D)} \ , \tag{10}$$

which for $\gamma = 5/3$ reduces to

$$(f-\phi)\frac{Re_o}{EC} = \frac{2}{3}\,\frac{dM}{d(x/D)} \quad . \tag{11}$$

The fact that $f - \phi$ does not vanish is a consequence of the gas components having different mass velocities in the x-direction.

Equations (6),(9),(10), and (11) are subject to the following assumptions and limitations:

(1) Sherman's analysis has been based on the assumption of large Reynolds numbers, so that second order terms (of order Re_o^{-2}) in the asymptotic expansion could be neglected. This is equivalent to stating that the free jet expansion of the gas mixture as a whole is reasonably well described by the isentropic theory, and that the diffusion effects, as well as the viscosity and heat conduction effects, introduce only small perturbations around the isentropic solution. Furthermore, as a consequence of retaining first order perturbation terms only, ordinary concentration diffusion is neglected. Because the local Reynolds number per unit length decreases with increasing x/D, it is evident that this analysis cannot be valid for arbitrarily large values of x/D.

(2) Since relatively few experimental data exist for the temperature dependence of the diffusion coefficient, the product ρD_{12} in Eq. (2) has been replaced by μ/Sc. In the subsequent analysis the local Schmidt number has then been considered independent of temperature, and it has been assumed that the temperature dependence of the diffusion processes are adequately taken into account by the temperature variation of the viscosity, for which sufficient data are available. In this connection, a linear viscosity-temperature relation ($\mu/\mu_o = CT/T_o$) has been assumed which becomes increasingly inaccurate with increasing x/D and the consequent very low temperatures, since for a real gas the relation is better described by a power law dependence, the exponent of which is less than unity.

Reference 8 presents an explicit numerical solution for the case of diatomic gases. In order to find the corresponding result for a monatomic gas mixture, Eq. (9) has been integrated numerically by the author. For the integration Wolff's calculated Mach number curve for $\gamma = 5/3$ was used from one nozzle diameter out to infinity. In lieu of other available data this curve was extended backwards through the orifice using impact probe data (see Ref. 15) for the case of air. This apparently inconsistent patchwork can be justified on two accounts.

(1) The isentropic expansion of a gas up to about Mach 2 is primarily a function of the geometry of the constraints on the flow and is only a weak function of γ .

(2) It has been demonstrated in Ref. 8 that the calculated downstream separation is almost insensitive to the shape of the axial Mach number profile through the nozzle.

The calculated results are shown in Fig. 2.2. These indicate that for a monatomic gas mixture the species separation takes place more rapidly and reaches a slightly higher value than for the diatomic case. Thus, it appears that for a helium-argon mixture almost all of the species separation in the expansion takes place over an initial distance of about three orifice diameters, and remains relatively constant thereafter. Furthermore, the theory predicts an inverse proportionality of $f - f_o$ to the flow Reynolds number. In fact, the species separation will be insignificantly small for $Re_o > 5000$ for all mixtures. For a given Reynolds number, on the other hand, the change in the mole fraction of argon appears to be a maximum for a mixture consisting of about equal numbers of helium and argon atoms. This is so, because the parameter E varies from zero, for $f_o = 0$, to a maximum value of about three at $f_o = 0.5$, and back to zero again, for $f_o = 1$.

In order to compare any experimental data with the theoretically predicted species separation, the jet Reynolds number and the parameters E and C must be calculated for the particular jet under investigation. In this connection, the product p_oD serves as a convenient parameter for defining the experimental conditions, since for any given gas or gas mixture this number is proportional to the jet Reynolds number. To facilitate an easy conversion of the experimental p_oD value to the jet Reynolds number and to Re_o/EC, the quantities Re_o/p_oD and $Re_o/EC\ p_oD$ have been calculated as a function of f_o for helium-argon mixtures at a stagnation temperature of 300°K (see Fig. 2.3 for these curves). In deriving these curves Wilke's formula (Ref. 16) was used to estimate the viscosities of the gas mixtures from the pure gas viscosities. The latter were calculated according to the Chapman-Enskog theory assuming an atomic interaction potential of the Lennard-Jones type (see e.g. Ref. 17).

For a theoretical treatment of the shock structure in binary gas mixtures the reader is referred to the papers by Sherman (Ref. 9). Fujimoto (Ref. 10) and Oberai (Ref. 11). The following two features, common to these theories, should be noted.

(1) Owing to the fact that barodiffusion tends to accelerate the heavy molecules in the downstream and the light molecules in the upstream direction, the light species compresses ahead of the heavier species, resulting in an enrichment of the light gas throughout most of the shock.

(2) The overall thickness of the shock transition, in terms of the upstream flow properties, is larger than for a pure gas under similar conditions.

One, very unexpected result is peculiar to Sherman's analysis, however, and is a consequence of the application of the Navier-Stokes equations to the shock structure problem. For a helium-argon mixture containing two per cent argon, Sherman finds the heavy gas accelerating in the upstream portion of a steady flow Mach 2 shock wave before undergoing the expected deceleration. Oberai, who uses a Mott-Smith type analysis, also calculates the shock profiles for the case of very small mole fractions of the heavy gas, but does not anywhere observe this peculiar behaviour of the heavy species. Since, by necessity, both these theoretical methods are approximate treatments of an inherently complex phenomenon, it is not possible at this time to discard one analysis in favour of the other on purely theoretical grounds. The answer will have to be provided by experiment. In fact, the initial behaviour of the heavy component at low concentrations may turn out to be a very sensitive test for the adequacy of any theoretical model.

III. THE ELECTRON BEAM DENSITY PROBE

The optical electron beam density probe was suggested and developed by Schumacher and Gadamer (Ref. 18) and was first applied to an actual flow investigation by Gadamer (Ref. 19), who showed that it can be used to accurately determine the local densities in a rarefied gas flow. The technique employs a narrow, well-collimated, high energy electron beam, which is projected at right angles to the flow through the region of interest. Because of the relatively small collision cross-section of the gas atoms for 20 kv electrons, the interaction of the beam with the gas is weak and results mainly in the scattering at small angles of some of the primary electrons. For gas densities below 4×10^{15} atoms per cm^3 (120μ Hg at room temperature) the beam remains well defined and virtually unattenuated over distances of the order of 10 cm. At the electron energy used many of the electron-atom interactions are of the elastic type. There occur, however, sufficient inelastic collisions, resulting in electronic excitation and subsequent de-excitation, to give rise to a luminescence, which is largely confined to the beam region itself. By focusing the luminescence onto an optical slit, which is at right angles to the beam, the light issuing from a small elemental gas volume is selected and can subsequently be analyzed by photomultipliers. The photocurrent measured is a direct indication of the molecular number density in the elemental volume under consideration. The component densities in a gas mixture can be measured selectively by spectrally separating the light emitted by the gas components.

It should be pointed out, that at gas densities corresponding to a gas pressure of 0.2 torr at room temperature, the average time between atomic collisions (of order 10^{-6} sec for most gases) becomes comparable to the life times of the excited states of the atoms (of order 10^{-8} sec for allowed transitions). Under these conditions, a measurable fraction of the electron beam excited atoms collide with other atoms (ground state atoms), before they can emit the excitation energy in the form of radiation. In this connection, it is quite unlikely, that in the collision all of the excitation energy (of order 10 ev) is converted to kinetic energy of the two colliding atoms. On the other hand, it is not difficult to think of collision processes, in which the excited atom is knocked into a different energy level, from which radiative de-excitation takes place in a spectral region, that lies outside the spectral range observed (e.g. in the ultra-violet). This makes the observed intensity of the electron beam luminescence less than one would otherwise predict. The effect is generally referred to as "collisional quenching" of the radiation concerned.

Since the collision frequency and, therefore, the collisional quenching effects are temperature dependent as well as density dependent, it is almost imperative to work with gas densities, at which collisional quenching can be neglected. For the visible spectrum of nitrogen Gadamer (Ref. 19) found no quenching effects up to 0.1 torr, and Muntz and Marsden (Ref. 20) found that for the green line of helium (λ 5016 Å) the quenching effects became important only above 0.25 torr.

IV. DESCRIPTION OF APPARATUS

4.1 The Low Density Tunnel

All experiments described in Sections V, VII, and VIII of this report were performed in the UTIAS steady flow low density tunnel, the basic design of which has been described by Enkenhus (Ref. 21). The primary pumping system of the tunnel consists of nine booster type oil vapour diffusion pumps, which have a total maximum pumping capacity of about 10,000 liters/sec of air at 0.03 torr. The pumping speed is somewhat lower for argon, but nearly twice that value for helium. Since the speed of sound in helium is about three times that in air, however, the exit diameter of a helium nozzle cannot be made as large as that of an air nozzle (producing the same Mach number jet at the same jet pressure) in order to not exceed the tunnel's pumping capacity. In the present tests the mass flow of helium was also limited by the mechanical backing pumps, which have a combined pumping speed of a nominal 485 cubic feet/minute at a pressure of about 1 torr, regardless of the gas used.

The pumping speed limitations of a low density tunnel define the maximum size of the expansion field of an underexpanded free jet, which can be produced in the tunnel. As was pointed out by Ashkenas and Sherman (Ref. 15), the distance from the sonic orifice to the Mach disc is simply proportional to the square root of the volumetric pumping speed, $\dot{V}$, of the tunnel, independent of the orifice diameter; i.e.

$$x_M = \frac{4}{3\sqrt{\pi}} \left(\gamma R T_o\right)^{-\frac{1}{4}} \left(\frac{\gamma+1}{2}\right)^{(\gamma+1)/4(\gamma-1)} \dot{V}^{\frac{1}{2}} \quad . \qquad (12)$$

With the present pumping capacity of the UTIAS tunnel the following maximum distances from the orifice to the Mach disc can be achieved:

air, x_M = 18 cm,
argon, x_M = 18 cm,
helium, x_M = 13 cm.

If the tunnel pressure, p_∞, is kept constant at the value at which the volumetric pumping speed is a maximum, in order to maximize the size of the test region, then the mass flow (which is proportional to $p_o D^2$) is fixed. In this case the jet Reynolds number is inversely proportional to the orifice diameter. For example, if the orifice diameter is decreased from D_1 to D_2, the stagnation chamber pressure has to be raised by a factor of $(D_1/D_2)^2$, for the equilibrium test section pressure, p_∞, to remain unchanged. The new jet Reynolds number is then larger by a factor of D_1/D_2. Furthermore, since x_M is unchanged, x_M/D has increased, and the maximum Mach number in the jet (just in front of the Mach disc) is correspondingly larger. Therefore, a wide variety of Mach number ranges and jet Reynolds numbers can easily be achieved by using a suitable selection of orifice sizes.

4.2 The Electron Gun

The electron gun assembly, complete with diffusion pumps and gauges, is mounted on a traversing table, which makes a sliding seal with the top of the test section of the UTIAS low density tunnel. An external traversing mechanism allows the electron beam, which passes through the test section from top to bottom, to be moved parallel to itself within a 15 cm by 15 cm square. A schematic diagram of the low density tunnel with the electron gun in place is given in Fig. 4.1. An external view of the gun and the traversing table, with the power supplies and the instrumentation in the background, is shown in Fig. 4.2.

The electron beam is produced by a commercial television tube gun (Philips, Part No. 902-564) housed in the inner of two concentric tubes, which pass through the traversing table into the test section of the tunnel, where the normal operating pressure is between 10^{-2} and 10^{-1} torr. To prevent deterioration of the electron gun cathode and to eliminate scattering of the electron beam before it enters the test section, the gun chamber (formed by the inner stainless steel tube) must be maintained at a vacuum of about 10^{-6} torr during operation. This is achieved by passing the electron beam through an intermediate pressure chamber before ejecting it into the test section. The intermediate pressure chamber is formed by the outer tube, which projects somewhat farther into the tunnel than the gun chamber. The gun chamber as well as the intermediate chamber are constantly evacuated by two separate 80 liters/sec oil vapour diffusion pumps (Edwards, Model 203B). A flexible backing line connects the diffusion pumps to a two stage rotary pump. The pressure in the intermediate chamber is less than 5×10^{-4} torr under normal operating conditions.

From the gun chamber into the intermediate chamber and from there into the test section the electron beam has to pass through two apertures of low gas conductance. These restrict the inflow of gas from the test section and confine the electron beam geometrically. The upper aperture is 2 mm in diameter and 12.5 mm long. The lower aperture is 1 mm in diameter and 15 mm long and is followed by a copper block with a $\frac{1}{2}$ mm wide slit to reduce the beam width as seen by the optical apparatus for a good spatial resolution. In both cases the apertures consist of cylindrical holes drilled through copper inserts, which can easily be replaced. The lower one is electrically insulated from ground by means of ceramic washers so that the electron beam current intercepted by it can be measured with a micro-ammeter.

Careful alignment and focusing of the beam is necessary to allow it to pass through both apertures. A system of eight electrostatic deflection plates mounted below the gun electrodes has proved to be an invaluable aid for bringing out the beam and for keeping the beam current constant during the tests. The voltage between the plates of any pair can be varied between -400 and +400 volts. The deflecting plates are 4 cm wide, 4 cm long, and 1cm apart. With the aid of the control circuit shown in Fig. 4.3 it is possible to shift the beam parallel to itself by a single adjustment for each of the two horizontal dimensions. Similarly, the beam can be tilted about its point of incidence at the upper aperture by adjusting a single control dial.

Any defocusing effect due to the transverse electric fields is minimized by always keeping the electric potentials of the plates of each pair equal in magnitude, but opposite in polarity, with respect to ground, so that the region traversed by the beam is effectively at ground potential.

The alignment of an originally misaligned beam is effected as follows. First the beam is shifted parallel to itself until the sum of the currents intercepted by the bottom aperture and the collecting cup is a maximum. This ensures that the beam passes freely through the top aperture. Then the beam is tilted around the top aperture until the current collected by the Faraday cup is a maximum. If, at this point, it is felt that the beam alignment can still be improved further, small trimming adjustments can be made by repeating the above sequence of operations. With this rapidly converging procedure a perfect alignment of the electron beam can be achieved with relative ease. As a final step the electron gun lens voltages are adjusted such as to minimize the current intercepted by the bottom aperture for an optimum focusing of the beam.

The cathode potential is supplied by an NJE high voltage, regulated, DC power supply and may be varied between zero and minus 30 kilo volts. The anode is kept at ground potential. The grid and lens voltages are obtained from a voltage divider circuit, which allows ample adjustment of the lens voltages (up to 15% of cathode potential). A rectifying and filtering network, which floats at cathode potential, supplies the filament current (see Fig. 4.3). A separate regulated 400 volt DC power supply (Kepco ABC 425 M) furnishes the deflection plate voltages.

A mechanical gun tilting mechanism is also provided in case a coarse alignment of the electron beam becomes necessary (see Fig. 4.4). This mechanism consists of two mutually perpendicular pairs of loops made from spring steel. These are attached to the glass pumping stem of the electron gun and bear against the inner wall of the gun chamber. When one of the loops is compressed or elongated by turning a threaded rod, the gun tilts around the anode clips, which rest in grooves machined in the anode block of the gun chamber.

To shield the electron beam from the earth's magnetic field and from any stray fields in the laboratory, the outer tube surrounding the gun chamber is made of mild steel. The fact that the tunnel itself is constructed from mild steel plate also helps in this respect.

The bottom aperture in the electron gun assembly can be closed by a remote-controlled door in order to isolate the electron gun chambers between tests, when the tunnel may be at atmospheric pressure. The electron gun elements are protected against back-streaming oil vapour (CVC Convalex-10) from the diffusion pumps by water cooled baffles and liquid nitrogen traps. Protective automatic valves have been built into the electron gun pumping system to guard it against the detrimental effects of electric power failures. The pumping connections and protective control circuits are shown in Fig. 4.5.

At the instant the electricity to the pumps is turned off, purposely or accidentally, a magnetic isolation valve between the mechanical pump and the diffusion pumps isolates the system from the rotary pump, and the rotary pump is automatically vented. In addition, the gun chambers are isolated from the diffusion pumps by two self-closing 2" butterfly valves. To close the valves the valve handles are turned through 90° by falling weights, which are released when the electric current ceases to flow through the solenoids that normally support the weights.

When the electric power is turned on again the venting valves close and the mechanical pump starts up. A slip clutch is provided to protect the motor from starting overloads. A time delay relay keeps the magnetic isolation valve closed for 120 seconds, by which time the pressure in the pipe between the mechanical pump and the isolation valve has dropped to 10^{-3} torr or less. After these two minutes the isolation valve opens, and the mechanical pump resumes pumping on the backing line and the diffusion pumps. The diffusion pumps remain off until the starting relays are activated again by a push button control. Similarly, the 2" butterfly valves have to be opened by hand, and the solenoids holding the weights have to be switched on. The above devices have been designed to keep the activated electron gun cathode under a high vacuum at all times and to keep the inner gun chamber from becoming contaminated with pump oil.

A hot cathode ionization gauge and a Pirani gauge are used to monitor the pressures in the gun chamber and in the backing line, respectively.

4.3 The Optical Analyzer

The function of the optical analyzer is to measure the intensity of the helium and argon radiation issuing from a small gas volume in the electron beam. In accordance with this requirement the instrument must have a high sensitivity to analyze a basically very weak light source, and it must spectrally discriminate between the light emissions from the helium and the argon. Furthermore, only light which originates in a well defined region of the electron beam should be allowed to enter the analyzer.

Good sensitivity is obtained by using an optical system of low f-number in conjunction with high gain photomultiplier tubes, selected for a maximum signal-to-noise ratio in the relevant spectral regions. Two achromatic f/2 lenses are used in an approximately symmetric configuration to form a real image of the electron beam. In the image plane a slit, normal to the electron beam, is used to spatially define the height of the section at the electron beam, from which light is received for analysis. To spectrally separate the helium radiation from the argon radiation, the light beam, emerging from the slit, issplit into two parts, each of which is transmitted through an optical filter and onto the cathode of a photomultiplier.

A narrow band interference filter (Baird-Atomic, Inc., Type B-11) is used to select the helium line at λ 5016Å. The half width of the filter's transmission band is 12Å. The intensity of the transmitted light is then measured with an EMI-9502S tube. The argon signal is obtained from an EMI-9558A tube used in conjunction with a red filter (Kodak, Wratten Filter No. 88A), which transmits light only at wave lengths above 7200Å. The EMI-9558A tube is insensitive to light above 8500Å. Several intense ArI lines exist in the spectral region between 7200Å and 8500Å, but practically no helium lines are located there. The spectral response curves of the photomultiplier-filter combinations are given in Fig. 4.6. These curves were obtained by multiplying the quantum efficiencies of the photocathodes with the transmission factors for the filters, as given by the manufacturers.

The photomultiplier tubes and the optics are contained in a light tight housing (constructed from $\frac{1}{4}$" thick black "Arboron" panels), which is rigidly supported from the outer electron gun tube inside the tunnel. This arrangement has the advantage that the optics remain aligned with the electron beam as the beam is moved from point to point in the flow field under study. Furthermore, the f-number of the instrument can be kept at a favourably low value by putting the analyzer inside the tunnel close to the beam. On the other hand, the typical gas densities (between 10^{-2} and 10^{-1} torr) inside the tunnel are such as to favour electrical breakdown between bare conductors, and suitable precautions have to be taken to prevent a glow discharge between the high voltage connections leading to the photomultipliers.

Originally the light was directed from the optical slit to the photomultipliers via a lens, a splitter plate, and a prism. As will be discussed in the following paragraph, this set-up proved unsatisfactory and was later revised. The original design is shown in Fig. 4.7. In this version the electron beam image is of the same size as the actual electron beam. The light emerging from the 2mm high slit, S, is bundled into a parallel beam by the lens, C. A dichroic splitter plate (Bausch & Lomb, Inc., Type 45-1-600), D, at an angle of 45° with respect to the light beam, transmits light of wave lengths between 3500Å and 6000Å and reflects the red light above 6500Å toward the argon detector (red filter + EMI-9558A). A right angled prism, P, is used to reflect the "green" light beam toward the helium detector (interference filter + EMI-9502 S).

Preliminary tests have shown that this optical arrangement is sensitive to small changes in optical alignment. For example, a small lateral shift of the electron beam of $\frac{1}{2}$mm, due to stray magnetic fields, causes the beam of light to shift over one cathode radius (5mm) at the EMI-9502 S tube, with a resulting attenuation of the helium signal of about 50 per cent. Owing to the large photocathode (44 mm in diameter) of the EMI-9558A tube the argon signal is affected less severely. It is evident that this arrangement is not very satisfactory, since the calibration curves for such a system are subject to change according to the space and time variations of the stray magnetic fields in the tunnel. Of the results discussed in this report the only measurements made with this optical arrangement are the preliminary tests discussed in Section 5.6.

To overcome the difficulties outlined in the foregoing paragraph, the optical components, S,C,D, and P, have been replaced by a fiber optical light guide (American Optical Co.). This light guide consists of two separate bundles of 0.076 mm diameter coated glass fibers. For each bundle the entrance section is rectangular (1.2 mm x 15 mm) and forms the horizontal slit. The exit sections are circular and rest directly on the optical filters (see Fig. 4.8). The dimensions of the light guide are such that the front face of the fiber optics is located about 3 cm ahead of the original slit plane, requiring a shift of the electron beam image plane by that distance. This makes it necessary to use the achromatic lenses in a slightly non-symmetrical arrangement resulting in an image "magnification" factor of 0.69. Hence, the 15 mm width of the fiber bundles in the image plane corresponds to a width of 22 mm at the actual electron beam.

An "ultra-stable" Keithley, Model M-242,power supply provides the cathode and dynode voltages for the multiplier tubes. Purely resistive voltage dividing chains (about 200 k-ohms between dynodes) are used for obtaining the dynode voltages. An additional voltage attenuating circuit,built from wire-wound precision resistors, allows for the possibility of applying different cathode potentials to the two tubes, using a common power supply (see Fig. 4.9 for the wiring diagram of the photomultiplier circuits). The anode currents are measured with the aid of a Keithley, Model 414, pico-ammeter. The photomultiplier bases and the voltage dividers are immersed in diffusion pump oil to prevent a glow discharge between the tube pins or across the dynode resistors. The latter are contained in a separate oil filled box. This prevents the heat dissipated by these resistors from raising the temperature of the photomultipliers which, in turn, would cause an increase in the dark currents of the tubes. The tubes are screened against external magnetic fields by mu-metal shields.

4.4 Nozzles and Shock Holder

The underexpanded free jets investigated were produced by letting the gas expand from the "high" pressure stagnation chamber into the "low" pressure test section through a sharp edged orifice. The orifice diameter consisted of a 5 mm, 15 mm, or 47.5 mm diameter hole machined in a brass end plate, which was fitted onto an existing converging nozzle of larger exit diameter. The 5 mm and 15 mm orifice plates were attached to a converging nozzle of 47.5 mm exit diameter. The 47.5 mm orifice plate was fitted to a subsonic nozzle of 140 mm diameter. The wall thickness at the orifice was equal to 0.03 times the orifice diameter in all cases.

The normal steady-flow shock waves studied were produced by means of a shock holder placed in the supersonic jet flow. The shock holder is depicted in Fig. 4.10. It consists of a cylindrical tube, 50 mm in diameter, with its axis parallel to the flow. The downstream end of this tube can be partially closed by means of a conical plug, in order to choke the flow through the tube just enough to produce a normal shock at the entrance lip of the shock holder. Four narrow slits are cut into the front lip of the shock holder, so that electron beam measurements can be made throughout the entire shock wave. Each slit is 3 mm wide and 12.5 mm long. The slits at the top and the bottom allow for the electron beam to be moved into the shock holder, whereas the slits in the side make it possible for the optical analyzer to "see" the beam, when it is probing the downstream portion of the shock transition inside the shock holder. Because the width of the slits is small with respect to the typical shock thickness encountered and with respect to the shock holder diameter, the influence of the slits on the shock geometry is believed to be negligible.

A photographic view of the spatial arrangement in the test section of the shock holder, the nozzle (5 mm), the electron gun, and the optical analyzer is given in Fig. 4.11. The photograph shows the bottom end of the electron gun (with the remote controlled door closed). The support arm, clamped around the gun tube, holds the optical analyzer (on the right) and the bracket for the Faraday cup (vertical rod on the left). A separate view of the optical analyzer (original version) is furnished in Fig. 4.12.

V. PRELIMINARY TESTS

5.1 Static Calibration Using Pure Gases

The photomultiplier anode currents, I_{ph}, were calibrated against helium and argon densities by admitting pure gases into the tunnel and by measuring the test section pressure with a McLeod gauge and the temperature with a thermocouple. All calibration tests were performed with a 17.5 k volt electron beam energy and a 100 μ amp beam current. In these tests the gases were leaked into the tunnel at a steady rate (monitored by a flow rater) through the auxiliary test section at point A (see Fig. 4.1), while one or more diffusion pumps kept the tunnel pressure at a steady value. The calibration curves for argon and helium, obtained in this manner, are shown in Fig. 5.1. The slight non-linearity of these curves is caused by the presence of a fluorescent halo around the electron beam, which at very low densities extends beyond the field width observed by the optical analyzer. The scatter of the calibration points is due to the uneven pumping of the diffusion pumps, causing small fluctuations in the tunnel pressure and a corresponding uncertainty in the McLeod gauge readings.

The optical filters used were not completely effective in separating the argon lines from the helium lines. There existed some degree of "cross-talk" between the filters producing small error signals, which had to be calibrated as well. This was easily done, for example, by recording the small argon signal obtained when calibrating for the helium radiation with pure helium in the tunnel. Likewise, the helium error signal, due to the presence of argon, was obtained simultaneously with the argon calibration. These erroneous signals were one to two orders of magnitude smaller than the "true" signals. The calibration curves for these error signals are given in Fig.5.2.

It is believed that the two ArII lines at λ 5009Å and λ5017Å were responsible for the helium error signal in the presence of argon. On the other hand, the "argon signal" observed in the static helium calibration cannot be attributed entirely to helium lines between λ 7200Å and λ 8500Å. The only helium line listed in this range in the "MIT Wavelength Tables" (Ref. 22) is the HeI line at λ 7281Å. Being very close to the cut-off wavelength of the red filter, the intensity of this line would have to be an order of magnitude above that given in Ref. 22 to fully account for the observed signal. It appears, therefore, that the "argon error signal due to the presence of helium" was caused to a large extent by impurity gases present in the tunnel during the static calibrations. With only one diffusion pump evacuating the tunnel, background gas pressures as "high" as 10^{-3} torr were observed in the tunnel. This background gas was the result of small leaks and of desorption of gases from the tunnel walls. In this connection it should be realized, however, that any atmospheric argon leaking into the tunnel cannot account for the observed argon error signal either, since the amounts of argon, which could possibly have been present in the test section, are at least two orders of magnitude below those indicated by the argon error signal. Although it is now believed, that most of the argon signal observed during the static helium calibrations was caused by N_2, no specific attempt has been made to identify the excitation mechanisms, or even the spectral bands, involved.*

---

* The band or bands, responsible for the observed light between λ 7200Å and λ 8500Å, probably belong to the first positive system of N_2.

This type of argon error signal could be expected to be practically absent in the free jet flows, because the level of impurity gases was significantly lower under these conditions than it was in the static tests. In the free jet runs 9 diffusion pumps were used (as compared to 1 or 2 in the static calibrations) to pump away the large volume flow of gas, thereby significantly reducing the impurity level in the test section. In addition, the test section gas could not penetrate into the supersonic jet. Free jet calibrations of the error signals could easily be made by observing simultaneously the helium and argon signals, obtained while moving the electron beam along the axes of pure helium and pure argon jets. In a pure helium jet, for example, the local helium density was obtained from the helium signal and the static calibration curve for helium (Fig. 5.1).* The argon error signal, caused by the radiative emission of the helium in the free jet at the indicated helium density, has then been plotted in Fig. 5.2. It is evident from Fig. 5.2 that the argon error signal, observed in the pure helium jet, is very much smaller than that obtained in helium containing small amounts of N_2. This remaining small argon error signal, which increases linearly with helium density, can be associated with the HeI line at $\lambda 7281.3\text{Å}$ ($3s\ {}^1S_0 - 2p\ {}^1P_1^o$). For the purpose of reducing the free jet and shock wave results, presented in Sections VII and VIII of this report, the free jet calibration of the argon error signal has been used. On the other hand, for the case of the helium error signal, measurements obtained in a free argon jet are in perfect agreement with the static calibrations (Fig. 5.2).

When the electron beam was near or inside the lip of the shock holder the observed beam intensity diminished, because the shock holder surfaces intercepted some of the light which would otherwise have entered the lens of the optical analyzer. Some light reflection from the shock holder surfaces occurred as well, increasing the amount of light received by the lens somewhat above that reaching the lens directly. The measurements very close to the nozzle were similarly affected. It is also conceivable that these grounded metallic objects could have actively influenced the intensity of the fluorescent halo (e.g. by removing metastable and ionized atoms from the beam surroundings, or by absorbing or emitting secondary electrons, or by absorbing or reflecting ultra-violet photons, which are involved in producing the helium halo). The changes in the helium and argon signals, which occurred when the electron beam was moved into the shock holder, were calibrated for various helium and argon densities under static conditions. Some such calibration curves are given in Fig. 5.3. These show that the main effect was a signal attenuation due to light interception by the shock holder lip. The solid curve in Fig. 5.3 gives the expected signal attenuation for an ideal point-source of light located on the axis of the shock holder (assuming non-reflecting surfaces). Because of the presence of a halo around the electron beam the experimental attenuation factors for the helium and argon signals are density dependent and lie above the theoretical point-source curve.** Furthermore, these calibrations had to be repeated every time the shock holder was adjusted or moved, because the optical alignment of the slit in the side of the shock holder critically influenced the amount of light received by the optical fibers in the analyzer. The signal attenuation for electron beam positions very close to the nozzle was also calibrated.

---

* It is shown in Section 5.4, that the static calibration curves can be used to infer gas densities in a high speed flow without introducing a significant error.

** A calibration of this effect was also made using nitrogen as a test gas and an interference filter centered around the N_2^+ band at $\lambda 3914\text{Å}$. In this case the signal attenuation followed the theoretical point-source curve closely. No halo has been observed for this N_2^+ band.

5.2 Electron Beam Excited Spectra in Helium and Argon

Before these calibration curves, obtained with pure gases under stagnant conditions, could be applied with any confidence to measure partial densities in gas mixtures flowing at supersonic speeds, the following questions had to be dealt with:

(1) What are the life times of the excited states involved? Are these short enough ($<10^{-6}$ sec), so that the excited atoms are not swept downstream, and are not lost from the field of observation, before they radiate?

(2) How do density gradients affect the symmetry of the fluorescent halo? Are accurate density measurements still possible when gradients are present?

(3) Is the radiation from the helium influenced by the presence of the argon in a gas mixture (or vice versa), giving rise to erroneous measurements of the species concentrations?

In order to answer these questions, it was necessary to have an understanding of the excitation processes involved. In particular an adequate knowledge of the nature of the fluorescent halo was required in this respect. The fluorescent mechanisms are, therefore, discussed in some detail here. In the following discussions the word "luminescence" is used to describe the light emission in the electron beam region resulting from the primary excitation of the gas by the high energy electrons. The term "fluorescence" is reserved for the halo resulting from secondary excitation by photons or secondary electrons.

For the helium line at λ 5015.7Å it has been shown conclusively by the work of Lees and Skinner (Ref. 23) and Wolf and Maurer (Ref. 24) that the fluorescent halo is caused almost entirely by the resonance spreading of the ultra-violet radiation of wave length 537Å resulting from the transition 3p $^1P_1^o$ - 1s $^1S_0$, (Fig. 5.4). For every thousand 3p $^1P_1^o$ states produced by primary excitation in the electron beam, 24 atoms de-excite to the metastable 2s $^1S_0$ state with the emission of green light at λ 5016Å, whereas 976 atoms de-excite down to the ground state with the emission of ultra-violet light at λ 537Å. The mean life time of the 3p $^1P_1^o$ state is only 1.74×10^{-9} sec (Ref. 25). When a neutral helium atom in the vicinity of the beam absorbs a λ 537Å photon this atom is raised to the 3p $^1P_1^o$ state and may again emit green light at λ 5016Å with a 0.024 probability. Because the λ 537Å photons have a relatively short mean free path, the radial outward flux of the ultra-violet light is rapidly attenuated. Consequently, the visual intensity of the helium fluorescence falls off faster than with the inverse distance from the beam, as would be appropriate for the cylindrical geometry alone. Before all the excitation energy of the original 3p $^1P_1^o$ states is completely converted to λ 5016Å radiation and metastable 2s $^1S_0$ states, the average ultra-violet photon is absorbed and re-emitted 40 times, as is evident from the ratio of the transition probabilities involved. Because the re-emission events are completely random with respect to direction, however, the photon does not diffuse more than a few optical mean free paths away from the electron beam in the process. The fact, that the helium calibration curve (Fig. 5.1) becomes linear at 5×10^{14} atoms per cm^3, is an indication that at higher densities essentially all the λ 5016Å photons produced reach the photomultiplier. This means that the ultra-violet resonance spreading is confined to a radial distance of about 1 cm at an atomic number density of 5×10^{14} atoms per cm^3. Consequently, the atomic absorption cross-section for this ultra-violet radiation is of the order of 10^{-14} cm^2.*

With respect to isolating the mechanisms involved in the helium fluorescence the work of Wolf and Maurer (Ref. 24) is of particular interest. For this reason a short outline of their experiments and conclusions is presented. The vacuum system used by Wolf and Maurer was divided into two chambers connected by a small aperture. The lower chamber was traversed by a high intensity, low energy electron beam (0.5 to 2.0 amp and 35 to 80 ev) parallel to the dividing wall. The analysis concentrated on the ray of fluorescence penetrating through the aperture into the upper chamber. The helium pressures ranged between 0.01 and 0.25 torr. The most conclusive parts of this study are itemized hereunder.

(1) A spectrographic survey revealed that most of the observed fluorescence consisted of HeI lines due to transitions from the np $^1P^o_1$ states to the 2s $^1S_0$ state (e.g. λ 3613Å, λ 3965Å, and λ 5016Å). Other weaker lines, however, were observed as well in the fluorescence, e.g.

λ 4388Å	(5d $^1D_2$ - 2p $^1P^o_1$)
λ 3889Å	(3p $^3P^o_{0,1,2}$ - 2s $^3S_1$)
λ 3820Å λ 4026Å λ 4472Å λ 5876Å	(nd ^3D - 2p $^3P^o$)

The lines in this second group became more intense relative to the lines in the first group with increasing helium pressure.

(2) In all tests a strong magnetic field of 1000 gauss parallel to the electron beam forced the scattered beam electrons and the secondary electrons to move in tight spirals, and thereby prevented these from moving away from the beam and into the upper observation chamber. Furthermore, an electric field of 330 volt/cm, applied normal to the ray of fluorescence, was found to have no influence on the spatial and spectral intensity distribution of the fluorescence. It could, thus, be concluded that secondary electrons and ions played at most a very minor role in producing the helium fluorescence in this configuration.

(3) A quartz plate, which absorbed the far ultra-violet but not the visible light, was placed across the observation chamber. In this case no fluorescence appeared above the quartz plate. This strongly suggested that all the observed helium fluorescence owed its existence to the ultra-violet resonance lines between 500Å and 600Å.

(4) The intensities of all lines found in the helium fluorescence increased linearly with electron beam current, indicating that a fluorescence of metastable helium atoms, diffusing away from the electron beam, could not

---

* Lees and Skinner estimate an experimental value of 2×10^{-15} cm^2 and derive a theoretical cross-section of 10^{-13} cm^2.

have been involved.

The observations, described above, conclusively showed that the strong lines (np $^1P_1^o$ - 2s $^1S_0$) observed in the helium fluorescence resulted from the resonance spreading of the ultra-violet transitions (np $^1P_1^o$ - 1s $^1S_0$), as described previously for the line at λ 5016Å. The presence in the fluorescence of the other "unexpected" lines (corresponding to transitions from excited levels such as ^1D, $^3P^o$, ^3D, etc.) could only be explained by assuming that the responsible terms are produced in the "halo" by collisions of the second kind of excited atoms in the $^1P_1^o$-states with neutral helium atoms in the ground state, e.g.,

$$\mathrm{He}\ (3p\ ^1P_1^o) + \mathrm{He}\ (1s\ ^1S_0) \rightarrow \mathrm{He}\ (1s\ ^1S_0) + \mathrm{He}\ (3d\ ^3D).$$

An actual spectrogram of the helium spectrum, excited by an electron beam, is presented in Fig. 5.5. Here the electron beam energy and current are 17.5 kv and 200 μ amp; the beam width is ½ mm. The helium pressure is about 0.1 torr, and the gas is at rest. The slit of the f/14 spectrograph (Hilger, Model E498) is normal to the electron beam image. The distance between the two vertical lines drawn across the spectrogram corresponds to the width of the electron beam. In the spectrograms* of Fig. 5.5 all HeI lines between λ 3800Å and λ 5900Å show some fluorescent spreading. This spreading is very pronounced for the lines at λ 3965Å and λ 5016Å. A relatively weak fluorescent halo is observed for the lines at

λ 3820Å	(6d ^3D - 2p $^3P^o$)
λ 3889Å	(3p $^3P^o$ - 2s ^3S)
λ 4026Å	(5d ^3D - 2p $^3P^o$)
λ 4144Å	(6d ^1D - 2p $^1P^o$)
λ 4388Å	(5d ^1D - 2p $^1P^o$)
λ 4472Å	(4d ^3D - 2p $^3P^o$)
λ 4922Å	(4d ^1D - 2p $^1P^o$)
λ 5876Å	(3d ^3D - 2p $^3P^o$)

It is, therefore, evident that for a 17.5 kv electron beam the characteristics of the helium fluorescence are very similar, if not identical, to those observed by Wolf and Maurer for an 80 ev beam. The nitrogen bands in Fig. 5.5 are caused by the background impurity level of about 10^{-3} torr in the tunnel.

The electron beam excited spectrum of argon differs markedly from that of helium. Whereas for the case of helium there exist practically no HeII lines in the electron beam induced luminescence, a substantial portion of the radiation from the electron beam excited argon results from transitions between excited levels of the argon ion. Since in the present experiments only ArI lines were utilized, the following discussion will concentrate on the spectrum of the neutral argon atom.

---

* The exposure time was about 1 hour.

A simplified energy level diagram for neutral argon is presented in Fig. 5.6. Only those levels are shown which account for most of the observed radiation in the blue and red parts of the spectrum. The wave lengths of spectral lines resulting from transitions from the $3p^5\,4p$ and $3p^5\,5p$ configurations to the levels of the $3p^5\,4s$ configuration are tabulated in Fig. 5.7. It should be noted that for neutral argon the spectral terms cannot easily be designated by the usual symbols established for atoms, which exclusively exhibit LS-coupling (Russell-Saunders) between the orbit and spin angular momenta of the excited electrons, because in many instances the electrons of the argon atom exhibit various degrees of jj-coupling. For this reason the energy levels for a given electronic configuration are often simply numbered consecutively in the order of increasing excitation energy. The information presented in Figs. 5.6 and 5.7 has been derived from Refs. 22, 26 and 27.

A spectrogram showing the electron beam excited argon lines in the blue and violet regions of the spectrum is given in Fig. 5.8*. This spectrogram was obtained in a high speed argon jet with a 1 mm wide electron beam perpendicular to the spectrograph slit and the flow. It shows a number of ArI and ArII lines, many of them exhibiting a halo-like fluorescence (e.g. the ArI line at λ4200.7), which extends farther on the downstream side than on the upstream side. Almost all the ArI lines in Fig. 5.8 are the result of transitions from the levels of the electronic $3p^5\,5p$ configuration to those of the $3p^5\,4s$ configuration. These lines are subject to the same excitation modes and transition rules, and should, therefore, exhibit the same characteristics, as the red lines belonging to the $3p^5\,4p \rightarrow 3p^5\,4s$ system of transitions. The characteristics of any red ArI line (contributing to the argon signal of the optical analyzer), can, thus, be inferred from the characteristics of a corresponding blue line in Fig. 5.8. Pairs of corresponding lines can easily be determined from the table in Fig. 5.7. Figure 5.8 is presented here primarily because of this close correspondence, and because of the fact, that a good spectrogram of the red argon lines, resulting from electron beam excitation, was not obtained, owing to a lack of sensitivity of easily available spectroscopic films in this region. Nevertheless, the red argon lines are significantly more intense, on an absolute scale, than the blue lines, as can easily be seen from Fig. 5.9A, which gives a spectrum obtained in an arc heated argon plasma jet. Figure 5.9B shows some of these same lines obtained from the argon luminescence produced by an electron beam. The strongest lines excited by the electron beam in this spectral region appear to be those at

λ 7504Å ,
λ 7515Å ,
λ 8104Å ,
λ 8115Å (strongest line),
λ 8408Å ,
and λ 8425Å .

---

* The author is indebted to D.J. Marsden, formerly at UTIAS and presently at the University of Alberta, for this spectrogram.

All these lines are the result of transitions from the electronic $3p^5\,4p$ configuration to the $3p^5\,4s$ configuration. The Einstein transition probabilities for these intense red argon lines are all about 5×10^7 sec^{-1} (Ref. 28). In the case of argon the even terms of the $3p^5\,4p$ configuration cannot be excited from the even ground state by resonance absorption of electric dipole radiation. Outside of the region traversed by the primary electrons the excited $3p^5\,4p$ states involved can, therefore, only be produced by secondary electron excitation and/or by resonance absorption of red light by excited atoms in the $3p^5\,4s$ configuration. The electronic $3p^5\,4s$ configuration gives rise to four terms, two of them metastable (see Fig. 5.6). It is believed that light absorption and re-emission by metastable argon atoms accounts for a substantial fraction of the observed intensity in the argon halo (some evidence for this is presented in the following sections). Atoms in the metastable $4s\ 1^o\ (^3P^o_2)$ and $4s\ 3^o\ (^3P^o_0)$ states, which originate in the electron beam, diffuse into the surrounding gas where they can absorb and re-emit red light of wave lengths 7635.11, 7723.76, 8014.79, 8115.31Å and 7724.21, 7948.18Å, respectively. Since this type of fluorescence depends on the diffusion field of the metastables, the red argon halo should, thus, show a definite non-symmetry in a high speed flow.

It is also conceivable that excited argon atoms in the short lived states, $4s\ 2^o\ (^3P^o_1)$ and $4s\ 4^o(^1P^o_1)$, contribute to the fluorescence, since these states can be produced outside of the beam from neutral argon atoms in the ground state by the absorption of the ultra-violet resonance lines of wave lengths 1066Å and 1048Å. During the short life times of 1.05×10^{-8} sec and 3.0×10^{-9} sec (Ref. 29) of the $4s\ 2^o$ and $4s\ 4^o$ states the argon atoms can absorb and later re-emit the red argon lines of wave lengths 7272.94, 7383.98, 7514.65, 8006.16, 8103.69, 8424.65Å and 7503.87, 8264.52, 8408.21, 8521.44Å, respectively. The part of the fluorescent halo, which is due to this cause, should have cylindrical symmetry in a uniform argon flow. The fluorescent mechanisms discussed above will, of course, also apply to the corresponding blue argon lines (see Fig. 5.7).

Having discussed the possible fluorescent mechanisms for helium and argon, it is now feasible to predict how the intensity per unit volume of the fluorescence should vary with electron beam current and with gas density. For this purpose let I_b be the electron beam current, n_b the number density of atoms of the relevant gas in the electron beam, and n_f the number density of atoms at the point outside of the beam at which the fluorescent intensity is to be considered. In cases where strong density gradients exist the values of n_b and n_f may well be different, and it is important under these conditions (with regard to the spatial resolution of the electron beam probe) to know , whether the fluorescence observed is proportional to n_b or n_f. On account of previous arguments the gaseous luminescence and fluorescence per unit volume should exhibit the following dependence on beam current and gas density.

(1) The intensity of the primary beam luminescence per unit length of beam is proportional to $n_b I_b$ for both gases.

(2) At very low helium densities, when the ultra-violet radiation flux is not attenuated appreciably by absorption, the intensity of the green helium fluorescence per unit volume, at a given position in the halo, is approximately proportional to $n_b n_f I_b$.

(3) For the argon line at λ 8115Å (for example) the local fluorescence per unit volume, due to absorption and re-emission by metastable argon atoms, is approximately proportional to $n_b^2 I_b^2$, since the radial diffusion flux of metastables and the radiation flux of λ 8115Å photons, originating in the electron beam, are both separately proportional to $n_b I_b$. Similarly, the local fluorescence due to ultra-violet excited argon atoms (e.g. λ 7504Å) can be shown to be proportional to $n_b^2 n_f I_b^2$.

(4) If it is assumed that the secondary electrons, resulting from primary ionization events in the beam, have energies in excess of 13 ev for argon and in excess of 20 ev for helium, then the fluorescence per unit volume due to excitation by secondary electrons (at a given point within the range of the secondaries) is proportional to $n_b n_f I_b$.

(5) If the secondary electrons have, on the average, energies below those cited above, they can only excite the metastable atoms, and the resulting local fluorescence per unit volume is approximately proportional to $n_b^2 I_b^2$. For the case of argon this fluorescence would have features, which are very similar to those discussed for the first mechanism in statement no. 3.

(6) The total intensity per unit length of the beam luminescence plus the fluorescence, integrated from the beam center to infinity, is again proportional to $n_b I_b$, since it is a direct function of the beam energy transferred to the gas by primary electron-atom collisions.

To obtain a photomultiplier signal which, for a given beam current, increases linearly with gas density, it is necessary to either look at the beam luminescence alone or, otherwise, include all of the fluorescent halo. The first alternative is impossible to achieve in practice, since there is always some fluorescence along the line of sight. Also, the signal would be a function of the electron current density in the beam, rather than of the total electron beam current. The second alternative can be approached closely by using a long slit at right angles to the electron beam, as was done in the present case. In this configuration the spatial resolution in the direction normal to the beam is still equal to the width of the primary electron beam, because the total light output is proportional to n_b and not n_f. As a third alternative a spectral line could be chosen which is known not to occur in the halo, but which is present in the primary luminescence. Since none of the intense helium and argon lines exhibits this property, this would mean working with extremely low light levels.

The dependence of the local fluorescence on n^2 (for some mechanisms even on n^3) causes the calibration curves in Fig. 5.1 to curve upward at the low density end. At higher density levels the fluorescence does not reach significantly beyond the field width of 22 mm observed with the optical analyzer, and the calibration curves approach a linear density dependence in accordance with statement no. 6, above. It is interesting to note that according to statement no. 3, above, the local argon fluorescence should vary as the square of the electron beam current. A somewhat non-linear behaviour of the argon signal with changing beam current was indeed observed. Consequently, it became necessary to work consistently with the same beam current for both calibration and experiment. In contrast with this behaviour, the helium signal varied linearly with beam current for all helium densities, indicating, in agreement with Wolf and Maurer (Ref. 24), that resonance absorption and re-emission by atoms in excited states do not play an important role for helium.

5.3 Optical Profiles of the Electron Beam in a High Speed Gas Flow

In order to study the characteristics of the halo, a series of tests were performed, in which a narrow slit (0.3 mm wide), parallel to the beam, was traversed at a uniform rate across the electron beam image, while the photomultiplier output currents were simultaneously displayed on an oscilloscope screen. In this fashion the profiles of the electron beam induced light, as seen through the optical filters, were obtained in the supersonic flow of helium and argon jets. Some of these profiles are reproduced in Fig. 5.10 showing the effect of pressure gradients and flow velocities normal to the beam on the symmetry of the optical radiation field. Figures 5.10a to 5.10e give the intensity profiles of the argon and helium radiation at various points along the axes of underexpanded helium and argon jets. The stagnation chamber pressure and temperature are 25 torr and 300°K. The orifice diameter is 5 mm. The flow is from right to left. The length scales have been determined from the ratio of the oscilloscope sweep speed to the scanning speed. It should be noted that under normal operation the field of view of the optical analyzer corresponds to 2.5 times that covered by the oscilloscope screen in Figs. 5.10b to 5.10e. The high intensity peaks, corresponding to about a 1 mm width, must be ascribed to the primary luminescence in the electron beam. The lack of asymmetry of these peaks indicates a mean life time of less than 10^{-7} sec for the upper excited states involved, as expected. In Fig. 5.10a the beam luminescence shows a considerable spreading due to small angle scattering of primary electrons by argon atoms. At a concentration of 2×10^{16} argon atoms/cm^3 (or 600 μ Hg at room temperature) this effect can be expected to dominate over the fluorescent light spreading, which cannot be discerned here. At an equivalent room temperature pressure of 145 μ Hg (Fig. 5.10b), however, the argon halo is clearly evident. The higher intensity of the halo on the downstream side is caused by the non-symmetrical diffusion field of argon metastables, which are apparently responsible for most of the fluorescence. As expected from the predominantly n^2 dependence of the argon fluorescence the relative local intensity in the argon halo at an equivalent room temperature pressure of 34 μ Hg (Fig. 5.10c) is only about 1/5 of that at 145 μ Hg. Figures 5.10d and 5.10e indicate that the symmetry of the green helium fluorescence is relatively unaffected by the gas velocities and density gradients in the free jet. It is also evident that the ultra-violet penetration into the surrounding gas decreases (i.e. the halo contracts) with increasing helium density.

Figure 5.10f shows the intensity profile observed through the helium filter in an argon jet. The light is believed to be due to the ArII lines at λ 5009.35Å ($4p\ ^4P^o_{5/2} - 4s\ ^4P_{3/2}$) and λ 5017.16Å ($4p'\ ^2F^o_{5/2} - 3d\ ^2D_{3/2}$), which are close enough to the helium line at λ 5016Å to pass through the helium interference filter. The "helium error signal" due to the presence of argon varies linearly with argon density (see Fig. 5.2). There exists, therefore, no halo due to secondary processes for the above two ArII lines. The delayed light emission evident in Fig. 5.10f must be associated with a relatively long life time of one of the two upper states involved. The mean life time in question is about 10^{-5} sec. Since the $4p\ ^4P^o_{5/2}$ state is known to have a mean life time of less than 6×10^{-8} sec (Ref. 28), the long life time probably belongs to the $4p'\ ^2F^o_{5/2}$ state.

5.4 Axial Density Measurements in Pure Gas Jets

The calibrated electron beam probe was used to determine the density along the axes of underexpanded free jets of pure helium and pure argon. Within the range of the static calibration curves the measured densities followed the theoretical density curve quite well (Fig. 5.11). This meant that the possible error, caused by the halo distortion due to a flowing gas with density gradients, could be neglected. These free jet runs were then used to extend the calibration curves to higher densities (Fig. 5.12). As is evident from Fig. 5.11, the density rise due to the Mach disc sets in relatively early, even though the Mach disc location is approximately that given by the accepted empirical law (Eq. 1). This suggests that the barrel shock and Mach disc are quite diffuse for the Reynolds number range covered. A flow visualization study of the free jets (Fig. 5.13) substantiates this. The photographs were obtained by uniformly traversing the electron beam in a plane defined by the flow axis and the beam itself during the exposure of the film. The technique has been described by the author in Ref. 30.

5.5 Shock Profiles in Pure Gases

Since normal shock waves in pure gases hav in the past been extensively studied, both theoretically and experimentally (see e.g. the survey paper by Talbot, Ref. 31), it can be assumed that the one-dimensional shock structure in a pure gas is reasonably well described (at least experimentally). In connection with early experimental shock structure studies, the Ph.D. work of F.S. Sherman (Ref. 32) deserves some mentioning at this point. In his report (and thesis) he describes the development and operation of various shock holders. The ideas, which he put forth on this subject, were used in the design of the shock holder described in Section 4.4. Sherman determined temperature profilesthrough steady flow shock waves (produced by shock holders placed in a supersonic wind tunnel flow) with a free-molecule equilibrium temperature probe. Most experimental shock structure work since then has been performed in shock tubes and shock tunnels.

For the present work the normal shock wave in a pure gas appeared to be a convenient flow configuration for testing the accuracy of the electron beam probe under the extreme conditions of strong streamwise gradients. There existed some doubt, whether the spatial resolution of the electron beam probe was sufficient to give a true density profile through the shock. In this context it should be kept in mind that the spatial resolution in the flow direction was determined by the electron beam width, which was between $\frac{1}{2}$mm and 1 mm. Furthermore, it could be expected that the distortion of the fluorescent halo (see Section 5.3), caused by the severe density gradient in the shock resulted in a possible error in the measured density.

To obtain an idea of the limits imposed by the spatial resolution (or the lack of it) of the electron beam probe, density measurements were made through plane shock waves produced by means of the shock holder, which was placed into free jets of pure argon and pure helium. Figure 5.14 is a flow visualization photograph of the flow configuration obtained by mapping out the density field with the electron beam. It depicts a Mach 4.5 shock in argon. The density profile through this shock (along the axis of symmetry), as measured with the optical analyzer, is given in Fig. 5.15.

The flow in the free jet is not uniform; it has streamwise gradients, and the streamlines diverge. It is, therefore, difficult to establish a close correspondence of the measured shock profile with that of a one-dimensional shock transition. On the other hand, an approximate comparison can be made by referring the measured density profile to a free stream base, which follows closely the axial density profile of the undisturbed free jet (the isentropic expansion curve for the free jet has been used here). On the downstream side of the shock this reference curve is allowed to asymptotically approach a constant downstream value, which is determined in such a way as to give the correct theoretical density ratio across a normal shock of a given Mach number (see Fig. 5.15). An approximate shock Mach number has been inferred from the position of the shock in the free jet expansion, which has been assumed to be close to isentropic.

Previous experimental shock thickness measurements made in argon (see e.g. Ref. 33 and 34) indicate that the one-dimensional maximum slope thickness, based on the density profile, ranges between 4 and 5 upstream mean free path lengths for shock Mach numbers between 3 and 10. For the argon shock in Figs. 5.14 and 5.15 the equivalent upstream mean free path, based on the asymptotic value of the reference density curve, is about 1 mm. On this basis, the experimental maximum slope thickness (δ_s) of 6 mm, as measured with the electron beam, appears to be about 30% too large. Although this discrepancy is still within the scatter of the experimental shock thicknesses reported in the literature, it is perhaps an indication that the spatial resolution of the electron beam densitometer prohibited the exact analysis of shocks, which were thinner than about 1 cm. On the other hand, this discrepancy could just as well be explained by the fact that, strictly speaking, the shock was not one-dimensional, because of shock curvature with respect to the streamlines, non-uniform upstream flow conditions, and the finite diameter of the shock holder. From this point of view there is thus no conclusive evidence that the limits, imposed by the spatial resolution of the electron beam probe, result in any artificial broadening of the shock transition. Since all other shock waves discussed in this report are wider than 6 mm, this matter has been given no further consideration.

The measured density profile through a Mach 8.5 shock in helium is given in Fig. 5.16. In this case the "equivalent" maximum slope thickness of the shock of 19 mm (as compared to an upstream mean free path of 4.7 mm) is in good agreement with other results reported in the recent literature ($\delta_s/\lambda_1 \approx 4$).

5.6 Static Calibration of Gas Mixtures with the Aid of a Mass-Spectrometer

The fact that secondary processes are responsible for spreading the light emission in a pure gas, strongly suggests the possibility that the helium signal observed in a gas mixture might be influenced by the presence of argon and vice versa. This could come about by the transfer of primary excitation energy from one atomic species to the other by radiative resonance coupling, by interatomic collisions, or by secondary electrons. Radiative resonance coupling can be eliminated immediately on the grounds that the energy levels of the excited states of helium are widely separated from those of argon. It turns out, that all excited ArI states are more than 4 ev below the first excited state of helium. Furthermore, all excited ArII states are at least 4.5 ev above the ionization limit of HeI and more than 20 ev below the first excited state of HeII. This state of affairs makes an inter-species energy transfer by atomic collisions also very unlikely, except, perhaps, by some rare "collisions of the third kind", in which the colliding atoms are both in excited states. This leaves the possibility of cross-excitation by secondary electrons.

A series of experiments, using gas mixtures of known composition and at known densities, were performed to test for any cross-excitation. The helium-argon mixtures were again introduced into the tunnal at point A (Fig. 4.1). Separate helium and argon supplies were used. The flow rate of each gas could be accurately controlled and was measured by a separate flow rater. Since at low tunnel pressures (below 50 μ Hg) the diffusion pumps pump away the helium faster than the argon, it follows that the helium to argon ratio in the tunnel was not identical with the ratio of the flow rates into the tunnel. It was, therefore, necessary to obtain an independent measurement of the gas composition in the tunnel. This was done by sampling the stagnant gas mixture from a point near the electron beam with a free molecule extraction tube (0.15 mm dia. x 5 cm lg. hypodermic stainless steel tubing). The sampling tube was connected to a "VEECO-MS-9 AB" mass spectrometer type leak detector. The experimental arrangement is shown schematically in Fig. 5.17. In all tests performed with this system the pressure behind the sampling tube, as measured by a hot cathode ionization gauge, was relatively independent of the tunnel pressure and ranged between 5×10^{-5} torr and 10^{-4} torr at all times. The helium ion current obtained from the mass spectrometer was calibrated against helium pressure in the test section by admitting pure helium into the tunnel and by measuring the helium pressure accurately with a McLeod gauge. This calibration curve is reproduced in Fig. 5.18.

The calibrated system was then used to determine the partial pressure of helium in the gas mixtures studied. The calibration curve for the helium ion current could be used directly to this effect, provided the flow through the sampling tube was free molecular, in which case the flow of argon atoms through the tube did not influence the flow of helium atoms through the tube. For the case of helium the Knudsen number based on the mean free path in the tunnel and the sampling tube diameter was larger than 5 for tunnel pressures below 200 μ Hg; for the case of argon this was so for pressures below 110 μ Hg. The molecular mean free path in the 1" copper tube* connecting the sampling tube to the leak detector was larger than 60 cm at all times.

The mixture composition in the tunnel was varied from 1% helium to 90% helium, and the total pressure in the test section, which was measured with the McLeod gauge, ranged from 5 μ Hg to 150 μ Hg. The helium and argon signals from the electron beam densitometer were calibrated for these helium-argon mixtures as follows: Through a control valve and a flow rater pure helium was admitted into the tunnel while one or two oil booster pumps kept the tunnel pressure at an equilibrium value. The test section pressure (McLeod), the helium ion current from the mass spectrometer, and the helium and argon signals from the optical analyzer were recorded. Then a specified amount of argon was added to the inflow through a second control valve. The helium flow rate was adjusted until the helium ion current from the mass spectrometer was again at the previously recorded value (i.e. the partial

---

* This tube had been thoroughly cleaned with hot detergent, with acetone, and with chlorothene, and had been baked out with a heat gun at about 300°C to reduce outgassing.

pressure of helium in the tunnel was the same). The new test section pressure and the electron beam densitometer readings were recorded. Then the inflow of argon was increased again following the same procedure. In this manner the partial pressure of argon was increased step by step, while keeping the partial pressure of helium constant, until the total pressure exceeded 100μHg. At the end of each run the pure helium calibrations were checked again at the particular helium pressure.

The procedure described above offered the most direct way of testing for any influence of the argon on the helium radiation measured by the optical analyzer. Several runs were made starting with different helium pressures. After subtracting the photomultiplier dark currents and the error signals it was found that within the experimental error the helium radiation at 5016Å remained constant for each run, independent of the amount of argon present.

In order to test whether the presence of helium had any influence on the argon fluorescence, the same data could be used. For each test the partial pressure of argon in the test section was obtained by subtracting the partial pressure of helium (leak detector) from the total pressure (McLeod). By comparing the argon signals obtained in the helium-argon mixtures with the corresponding pure argon calibration values, no influence of the helium on the argon signal could be detected.

The experimental results of these tests are summarized in Figs. 5.19 and 5.20. The magnitude of the probable error is indicated by the vertical "error bar" drawn through each experimental point. These errors are based on an estimate of the following effects, which are believed to be responsible for most of the scatter of points in Figs. 5.19 and 5.20:

(1) Small fluctuations of the tunnel pressure occurred during each test because of the somewhat uneven pumping of the oil vapour booster pumps on the tunnel. Owing to their different time constants the instruments used indicated different average densities or pressures. The time constants involved were:

electron beam densitometer	$\tau < 1$ sec
McLeod gauge	$\tau \approx 1$ min
mass spectrometer	$3 \text{ min} < \tau < 6$ min

(2) The ion current amplifier in the leak detector showed signs of drift and of instability with respect to power line fluctuations.

It is interesting to note that, in order to keep the helium pressure constant during a run, the helium inflow into the tunnel had to be reduced as more argon was added. This can be attributed to the fact that above 30 μ Hg the volumetric pumping speed of the booster pumps decreased with increasing pressure. At lower pressures this must be attributed to a decrease in the preferential pumping of helium with increasing pressure. The latter effect has been investigated by leaking a constant composition gas mixture (57.5% He - 42.5% Ar) from a high pressure cylinder into the tunnel and by measuring the equilibrium composition in the tunnel with the mass-spectrometer for various tunnel pressures. The results are plotted in Fig. 5.21, which seems to indicate that the effect has virtually disappeared at pressures above 50 μ Hg.

Since the tests discussed in this section indicate no noticeable coupling between the helium radiation and the argon radiation, it must be concluded that the secondary electrons, which originate in the electron beam from ionizing collisions with one atomic species, have on the average, not enough kinetic energy to excite atoms of the other species. In this connection it is of interest to note that for 17.5 kv electrons the ionization cross-section of the argon atom is about ten times that of the helium atom (see Ref. 35). In mixtures containing more than 10% argon, therefore, the majority of the secondary electrons produced result from argon ionization events. Hence, the data presented in Figs. 5.19 and 5.20 provide strong evidence for the conclusion that secondary electrons originating from argon atoms have energies of less than 20 ev.* On the other hand, they provide relatively weak evidence for the secondary electrons originating from helium atoms to have energies of less than 12 ev.**

VI. DISCUSSION OF SYSTEMATIC ERRORS

On the basis of the preliminary calibration and validity tests the following remarks can be made about some of the possible sources of error in the final results.

(1) If no spurious background, like N_2 is present, the helium and argon "error signals" due to cross-talk between the optical filters present no problem, since these can be accurately calibrated and subtracted from the final readings. Owing to their relative smallness (see Fig. 5.2), these error signals become significant only for the rare component in mixtures containing very small amounts of either helium or argon.

(2) In a high speed flow the downstream drift of metastable argon atoms, resulting in a partial "loss" of the argon halo, causes the argon signal to be lower than the calibrated value for a given density. The free jet tests in pure gases show this effect to be small, and it has therefore, been ignored.

(3) Simple density gradients across or along the electron beam "distort" the halo. The observed signal is, however, not appreciably affected, since the effects of the low density region on the one side approximately compensate for the effects of the high density region on the other side. Second spatial density derivatives across or along the electron beam may, on the other hand, influence the observed signals significantly. Second density derivatives across the beam are not serious, provided almost all of the light in the halo is collected for the analysis. Those occurring along the beam, however, invariably introduce an error in the measured density. In the present case the most severely affected measurements are those made on the axis of the free jets close to the 5 mm orifice. Here a high density region is closely surrounded by a region of low density, resulting in a diminished halo intensity. For the argon density measurements small corrections have been applied in these

---

* Energy above the ground state of the first excited state of the helium atom is 19.86 ev.

** Energy above the ground state of the first excited state of the argon atom is 11.5 ev.

severe cases, based on an estimate of the effect. For the helium this effect has been ignored.

(4) The mass-spectrometer tests have shown that any coupling between the helium and argon fluorescence, through secondary electron excitation (or any other mechanism), does not introduce any significant error into the partial density measurements of the component gases in helium-argon mixtures.

(5) The reflection and interception of light by the nozzle face and the shock holder surfaces has been found to affect the density readings near these objects (see Section 5.1). This effect has been calibrated for the relevant spectral lines in the density range encountered. Corresponding correction factors have been applied.

(6) The dark currents of the photomultiplier tubes were measured before and after every run and have been subtracted from every reading. The magnitudes of the average dark currents were

5×10^{-10} amp for the EMI-9502 S tube, and
2×10^{-9} amp for the EMI-9558A tube .

In most instances these currents were completely negligible when compared to the normal signal strengths (see Fig. 5.1).

At this point a word is in order about the possibility of condensation occurring in the free jets, since this might complicate the free jet structure and influence the diffusion processes taking place in the free jet and the shock waves produced therein. In the free jet expansions (stagnation temperature was about 300°K) the local temperatures and pressures decreased such that under equilibrium conditions the argon should have condensed (into the solid state) between Mach numbers of 4 and 5 in the jet. Owing to the low densities and the high rates of expansion occurring in these free jets, however, condensation does not easily take place, and a high degree of supersaturation can be obtained. For nucleation to occur in the free jet "Ar_2-molecules" have to be formed first by triple collisions (a third particle is needed to carry away the heat of sublimation). Anderson, Andres, Fenn, and Maise (Ref. 36) have made a calculation, based on kinetic theory, of the mole fraction of Ar_2 to be found in free argon jets expanding from room temperature to the collisionless state. The predicted values are in agreement with experimental values obtained by Milne (Refs. 37 and 38), who observed "cluster populations" in free jets using a mass spectrometer. On the basis of these studies it is estimated that the mole fraction of Ar_2 in any of the jets, used in the present work, is below 5×10^{-5}. Accordingly, it is believed that condensation effects can be ignored.

VII. FREE JET RESULTS (Helium-Argon Mixtures)

Having gained sufficient confidence in the technique by the foregoing tests the optical electron beam probe was used to study the density distribution in the free jet expansion of helium-argon mixtures. The mole fraction of argon in the stagnation chamber ranged from 0.05 to 0.5. The gas mixtures were bought in pressurized cylinders from the Union Carbide Corporation. Although the gas composition in these cylinders was known approximately, a separate quantitative analysis (see Appendix A) of these gas mixtures had to be performed, since the reduction of the free jet data required an accurate knowledge of the f_o-values. The cylinders used were found to contain the following mole fractions of argon.

$$\left.\begin{array}{ll} \text{cylinder 1} & f_o = 0.12 \\ \text{cylinder 2} & f_o = 0.21 \\ \text{cylinder 3} & f_o = 0.425 \\ \text{cylinder 4} & f_o = 0.11 \\ \text{cylinder 5} & f_o = 0.49 \end{array}\right\} \pm 0.005$$

Other mixtures were metered into the tunnel from separate gas supplies. The stagnation temperature was approximately 300°K for all runs. The jet Reynolds numbers varied between 100 and 10,000. The range covered by each nozzle was as follows:

$D = 47.5$ mm - $100 < Re_o < 500$,
$D = 15$ mm - $200 < Re_o < 2000$,
$D = 5$ mm - $500 < Re_o < 10{,}000$.

The Reynolds number ranges overlap sufficiently, so that, for some free jet runs, Reynolds numbers could be duplicated with different orifices.

It may be argued, on account of the non-zero value of $\phi - f_o$ at the center of the orifice (Fig. 2.2), that the mole fractions of the gas components in the stagnation chamber could well be different from those in the supply cylinder. This would indeed be true if the integral of $\phi - f_o$, integrated over the orifice area, were non-zero. For the reduction of the experimental data it has been assumed, that in the orifice the value of $\phi - f_o$ is sufficiently negative off the axis to exactly balance the positive contribution on the jet axis. An argument is presented in Appendix B to support this assumption. Consequently, the stagnation chamber value of f_o has been taken to be identical with that in the supply cylinder (or with the value derived from the volume flow rates metered in).

Figure 5.13 shows the general structure of the jet flow fields. As is evident from these photographs, the lower Reynolds number jets exhibit a very diffuse shock envelope. For these jets the barrel shock and the Mach disc have become broadened to the point, where the extent of the undisturbed central flow field is considerably reduced. In agreement with the photographs the axial density surveys, performed with the electron beam probe, indicate a density deviation from the isentropic behaviour somewhat ahead of the expected Mach disc location.

An attempt has been made to account for the different appearances of these jets in terms of the flow parameters. The general features of an underexpanded jet are characterized by the size of the first expansion cell and by the diffuseness of the barrel shock and Mach disc. The distance [illegible] The relative thickness of the barrel shock at any point, or that of the Mach disc, may be defined by the ratio formed by the shock thickness, δ , and the streamline distance, s, from the orifice plane to the center of the shock. If it is assumed that the density along the jet axis falls off as $(x/D)^{-2}$ (corresponding to a simple source flow model with the source located near the orifice), and if the shock thickness is assumed to be equal to 4.5 times the distance of a molecular mean free path ahead of the shock (a value, which agrees reasonably well with experimental data for $M_1 > 4$), then the relative thickness of the Mach disc can be shown (see Appendix C) to vary inversely as the jet Reynolds number and directly as the jet pressure ratio raised to a power, which falls between 1/3 and 1/2, depending on the viscosity-temperature law assumed. If $\mu_1/\mu_o = (T_1/T_o)^{\frac{1}{2}}$ is assumed, then the relative thickness of the Mach disc becomes,

$$\frac{\delta}{x_M} = 69 \quad \frac{\gamma^{3/2}}{(\gamma+1)^2\,(\gamma-1)} \quad Re_o^{-1} \left(\frac{p_o}{p_\infty}\right)^{\frac{1}{2}} \quad . \qquad (13)$$

This equation applies to a pure gas. For a gas mixture the shock may be several times wider. When the jet Reynolds number and the jet pressure ratio are such that δ/x_M becomes approximately unity, then no region in the jet remains undisturbed by the ambient gas. For the barrel shock δ/s can be considered proportional to $(p_o/p_\infty)^{\frac{1}{2}}\ Re_o^{-1}$ in a very approximate sense only. A qualitative analysis of a number of flow visualization photographs confirms the above dependence.

Some of the experimental density profiles obtained along the axes of various free jets are presented in Figs. 7.1 to 7.8. In these figures the partial number densities of helium and argon atoms, normalized with respect to the corresponding partial number densities in the stagnation chamber, have been plotted against axial distance in terms of x/D. The original mole fraction of argon, the jet Reynolds number, the orifice diameter, and the pressures on either side of the orifice, are stated for each run. The gas mixtures as a whole follow the isentropic expansion curve quite well, which drops off approximately as the inverse square of the axial distance for x larger than 2D. The first experimental downstream deviation from this dependence for any one run indicates the point at which the surroundings start to affect the axial flow. The apparent discrepancy between the shape of the isentrope and the experimental curves, very close to the orifice ($x/D < 0.5$), is simply a consequence of the fact, that the isentropic expansion through a sonic orifice is not exactly known. In all cases the argon curve is above the helium curve, indicating an argon enrichment along the jet centerline. It is evident from these figures that the axial argon enrichment decreases with increasing jet Reynolds number. As shown by Figs. 7.7 and 7.8 the diffusive component separation on the jet axis becomes very small indeed for Reynolds numbers of 2000 and 3000. For jet Reynolds numbers above 5000 the separation was smaller than the experimental error and could not be detected. For all density profiles shown, the density increase caused by the "Mach disc" (i.e. the diffuse shock envelope closing in) is clearly evident. As predicted by one-dimensional shock theory the helium compresses ahead of the argon, resulting in a helium enrichment in the Mach disc. The corrected and smoothed out experimental density data are believed to be accurate to within one or two percent.

From these experimental density profiles, the local mole fractions of argon can easily be determined. For the free jets starting out with original mole fractions of argon of 0.12 and 0.425 these mole fractions have been plotted against $(x/D)^{\frac{1}{2}}$ for various Reynolds numbers in Figs. 7.9 and 7.10. The solid curves give the theoretical mole fractions as per Fig. 2.2 The downstream "tails", indicating a sudden decrease in the mole fraction of argon, are caused by the Mach discs. It should be noted that free jets originating from different stagnation conditions and emerging through different sized orifices, but having approximately the same Reynolds number (and the same f_o), show identical species separation effects. Also, in the undisturbed portions of the free jet expansions the agreement with theory is quite reasonable.

In Fig. 7.11 the experimental data for gas mixtures ranging from 5% to 50% argon and for Reynolds numbers between 100 and 1000 have been summarized and are compared with Sherman's theory (Ref. 8). Only those portions of the free jets which were not affected by the shock envelope have been used in this graph. Note that in this representation the experimental errors are multiplied by the Reynolds numbers of the jets, resulting in a fair amount of experimental scatter. It is evident that Sherman's first order approximation predicts the actual species separation on the jet axis quite well, even for Reynolds numbers as small as 100.

Point-by-point measurements of the partial densities of helium and argon were made throughout the free jet, off the axis as well as on the axis, for two cases:

Jet 1: $f_o = 0.12$, $Re_o = 533$, $D = 15$ mm, $p_o/p_\infty = 150$.

Jet 2: $f_o = 0.21$, $Re_o = 224$, $D = 15$ mm, $p_o/p_\infty = 188$.

For jet 1 the radial number density profiles at various axial positions are given in Fig. 7.12. The mole fraction of argon throughout the jet is shown in Fig. 7.13. The "depression" in the downstream direction after the initial increase in f is caused by the Mach disc. A pronounced argon deficiency exists also near the edge of the jet. This is believed to be partially due to the presence of the barrel shock and partially due to the fact that radial pressure diffusion causes an argon enrichment on the axis and a corresponding argon deficiency off the axis of the jet. The gas in the test section outside of the jet is slightly more enriched in argon than the stagnation chamber gas, because the diffusion pumps remove the helium at a somewhat faster rate. A flow visualization of jet 1 is given by the bottom left photograph of Fig. 5.13. The radial partial density profiles for jet 2 are presented in Fig. 7.14; the mole fractions of argon throughout the flow field are plotted in Fig. 7.15. The results indicate the same general features for jet 2 as were observed for jet 1. Throughout the jet the separation effects are somewhat more pronounced because of the lower Reynolds number. Furthermore, the features which can be related to the barrel shock and Mach disc are considerably more diffuse.

VIII. SHOCK WAVE RESULTS (Helium-Argon Mixtures)

Normal shock waves were produced in front of the partially choked shock sholder placed in the free jets. Figure 8.1 shows the general appearance of the shock waves investigated. It is a flow visualization photograph of a Mach 9 shock in a 49% argon mixture. The shock appears to be quite plane, perhaps slightly "dished in". It should be kept in mind, however, that a plane shock in a diverging flow corresponds to a curved convex shock in a parallel flow. From this point of view the shock in Fig. 8.1 is not dished in enough to be perpendicular to the incoming streamlines at all points and corresponds, therefore, to a shock which has a small convex curvature with respect to the streamlines. This is also true for the other shock waves studied. Furthermore, the shock diameter is only about three times the shock thickness. The shocks can, thus, hardly be considered one-dimensional.

Figures 8.2 to 8.4 give the normalized partial density profiles along the axes of the underexpanded jets and through the shock waves for 49%, 11% and 1% original argon mixtures, respectively. The corresponding profiles of "f" are given in Figs. 8.5 to 8.7. The initial argon enrichment is caused by the free jet expansion. In all cases the helium compresses ahead of the argon in concord with theory. Radial diffusion in and behind the shock is believed to be responsible for the pronounced argon surplus inside the shock holder. For the 1% argon case the general features are as for the other cases, except for the behaviour of the argon density in the upstream portion of the shock. The partial argon density, which originally is significantly above the isentropic expansion curve, decreases below the isentrope prior to compression. This can be interpreted as an acceleration of the argon atoms beyond the free stream value, in which case it would verify the effect described by Sherman (Ref. 9). It should be noted, however, that the scatter of the experimental argon densities in Fig. 8.4 is relatively large because of the smallness of the argon signals measured in this case. Furthermore, the argon error signals subtracted, due to the presence of helium, were larger than the true argon signals. On account of this there exists some uncertainty about the argon density curve drawn in Fig. 8.4. The effect, however, appears to be real, and it remains a matter of interpretation, whether it is ascribed to a one-dimensional acceleration of the argon or to a three-dimensional effect, hitherto unexplained.

In order to get a rough comparison of the experimental shock profiles with the existing one-dimensional theories an attempt has been made to compensate for the fact that the shock is embedded in a flow with considerable streamwise gradients. To this effect an arbitrary reference curve has been drawn in each of Figs. 8.2, 8.3 and 8.4. This reference curve follows the isentropic expansion curve into the shock and then levels out smoothly toward a constant downstream reference density, which was chosen to be equal to the isentropic free jet density at the centre of the helium shock. Of course, this procedure has to be viewed with serious reservations and is offered here only in an attempt to compare the salient features in a qualitative way.

Figure 8.8 gives the total mass density divided by the local reference density through the shock. The total mass density has been calculated from the density curves for the individual species. The distance is given in terms of the upstream mean free path defined by

$$\lambda_1 = \frac{16}{5}\left(\frac{\gamma}{2\pi}\right)^{\frac{1}{2}} \frac{\mu_1}{\rho_1 u_1} M_1 , \qquad (14)$$

where the subscript 1 refers to conditions just ahead of the shock. Equation (14) is the accepted formula for the mean free path of smooth elastic spheres. Even though this "mean free path" has no direct microscopic meaning for a gas mixture, it serves as a convenient reference length. In calculating this reference length the shock Mach number, M_1, was estimated from the position of the shock in the free jet. The free stream quantities, ρ_1, T_1, and u_1 were then obtained from ρ_o, T_o and M_1, using the isentropic relations. The pure helium and pure argon viscosities at T_1 were estimated according to the Chapman-Enskog theory, assuming an atomic interaction potential of the Lennard-Jones type. Wilke's formula (Ref. 16) was then used to calculate μ_1 for the gas mixture, using the pure gas viscosities. For the purpose of displaying several shock profiles in one figure, the zero point of the axial length scale has been relocated at the position, at which the total mass density has reached half the theoretical density increase for the given shock Mach number. To distinguish this shifted length scale from the previously defined x-scale (with the zero point at the orifice), a new symbol, x', has been introduced in Fig. 8.8.

The increase in the non-dimensional shock thickness with increasing mole fraction of argon, from pure helium (curve 1) to 50% argon (curve 4), is evident from the shock profiles in Fig. 8.8, which are all for an upstream Mach number of about 9. The compression ratio across the experimental pure helium shock agrees quite well with one-dimensional shock theory and provides some "justification" for the use of the somewhat arbitary reference curve. In the case of the gas mixtures the total mass density on the downstream side of the shock turns out to be too high, because there is too much argon due to radial diffusion in the "curved" shock.

It can be expected that both the shock Mach number and the Reynolds number, based on the free stream conditions and the radius of shock curvature (i.e. $Re_r = \rho_1 u_1 r_c/\mu_1$), become scaling parameters for the radial diffusion effect behind curved shocks. A third parameter is needed to describe the dependence of the effect on the free stream composition. Since no appropriate function has as yet been derived for the curved shock problem, it is assumed here that the function E_1, based on the free stream composition, adequately describes the composition dependence of the radial diffusion effect. In parallel with Sherman's free jet analysis one might then expect, that, for a given shock Mach number, the quantity $(f_2-f_1)Re_r/E_1$ is approximately constant for all curved shocks (f_2 is the mole fraction of argon behind the normal part of the shock). Furthermore, the Mach number dependence of the argon enrichment is probably insignificant for $M_1 > 5$.

For the experimental shock waves discussed here, it is difficult to estimate, what the equivalent shock curvature would be, if the shocks were embedded in a parallel flow. An approximate transformation from the diverging flow of the free jet to a parallel flow can be obtained, if one imagines the incident streamlines rigidly attached to the shock surface, and if one then rotates these streamlines into a parallel configuration, thereby forcing the shock surface into a more convex shape (the angle of incidence of each streamline remaining constant in the process). On this basis it has been estimated from flow visualization photographs, that the equivalent radii of shock curvature ranged between 10 cm and 20 cm, and that the quantity $(f_2-f_1)Re_r/E_1$ is of the order of 100 for these shocks.

It is also difficult to define a meaningful shock thickness for the shocks of Fig. 8.8, since the downstream halves of the shock waves 2, 3, and 4 differ radically from any corresponding one-dimensional shocks. The upstream halves of the shock waves, on the other hand, should not be significantly influenced by radial diffusion and should correspond closely to those of one-dimensional shocks. This appears to be a reasonable assumption, because in the supersonic part of the shock the downstream influences are expected to produce no significant curvature of the streamlines. An approximate "equivalent 1D-shock thickness", δ_s, has therefore been defined by taking the slope of the total mass density profile at $x' = 0$ and extending it down to $\rho/\rho_{REF} = 1$ and up to the theoretical density ratio. Thus δ_s is defined by

$$\delta_s = \frac{(\rho_2/\rho_1)_{TH} - 1}{[d(\rho/\rho_{REF})/dx']_{x'=0}} \qquad (15)$$

The values of δ_s and δ_s/λ_1 obtained in this fashion are tabulated in Fig. 8.8. These values indicate, that for a shock of $M_1 = 9$ and $f_1 = 0.5$ the shock thickness, in terms of λ_1, is about three times that in a pure gas ($f_1 = 0$ or 1).

IX. CONCLUSIONS

Based on the reported experiments and discussionsthe following concluding remarks can be made.

(1) The method of using a thin electron beam and a set of interference filters for a spectroscopic study of the composition of rarefied gases has been shown to give accurate results for argon-helium mixtures. Other mixtures may presumably be analyzed in a similar manner, provided that the excitation processes involved are reasonably well understood. It appears to be necessary to make preliminary tests, similar to those outlined in Section V, for each new gas mixture and for each new set of spectral lines selected in order to interpret the beam intensity measurements correctly. The electron beam provides, at the same time, a convenient means of mapping out photographically the density field under study.

(2) No radiative coupling between the helium and the argon fluorescence has been detected in helium-argon mixtures. Any interspecies transfer of excitation energy by secondary electrons must evidently be insignificant.

(3) Sherman's theory for the species separation along the centerline of an underexpanded free jet has been substantiated experimentally for a binary mixture of monatomic gases. According to this theory and the experimental tests the species separation in the undisturbed free jet is smaller than has previously been observed by investigators, such as Stern and Waterman or Chow, who analyzed the gas sampled by a skimmer or sampling tube placed in the jet. The species separation is inversely proportional to the jet Reynolds number and takes place almost entirely over the first three diameters downstream of the orifice. For Reynolds numbers above 5000 the species separation becomes insignificantly small.

(4) The salient features predicted for the one-dimensional shock structure in a binary non-reacting gas mixture have been observed. For all shock waves encountered the light gas has been found to compress significantly ahead of the heavy gas, resulting in an enrichment of the light atomic species throughout most of the shock. In terms of the upstream gas properties the shock transition for a gas mixture has been observed to be up to three times as wide as for a pure gas. For a Mach 9 shock in a 1% argon mixture the argon has been observed to expand beyond the free stream value in the upstream portion of the shock transition. If this is interpreted as a one-dimensional effect it means an argon acceleration as predicted by Sherman. It is felt, however, that for a definite proof of the existence of this effect, is is necessary to repeat the experiment in a truly uniform one-dimensional high Mach number flow, which was not attainable with the present UTIAS low density facility.

(5) The shock wave results indicate that shock curvature may produce very significant radial diffusion effects, resulting in an enrichment of the heavy gas on the centerline behind the shock. This effect might be used to explain, at least partially, the unrealistically large species separation observed when sampling tubes are introduced into a supersonic flow field.

There remain a number of interesting gas dynamical problems for the study of which the optical electron beam densitometer is ideally suited. A short list of the most obvious extensions of the present experiments is given hereunder.

(1) A study could be made of the diffusion effects in the free jet expansion and the shock compression of a mixture of diatomic gases (say, N_2 and H_2). This is of particular interest, since the rotational temperatures of the component species could also be obtained using the electron beam technique (Ref. 39). The component temperatures are not expected to be equal at a point inside a shock wave, for example.

(2) Along similar lines, a study of the diffusive separation in gas mixtures, the components of which having different specific heat ratios (γ), should be of interest. This problem also remains to be solved theoretically.

(3) A systematic study should be made of the effect of shock curvature on the degree of heavy species enrichment behind the curved shock.

(4) In the present study an attempt was made to verify one-dimensional shock structure theory for binary gas mixtures. The present experiments have shown that this cannot be done accurately in a free jet flow field. These studies should be repeated in a truly uniform flow.

(5) Species concentration measurements should be of value in countless applications involving reacting gas mixtures.

(6) A detailed spectroscopic study of the radiation resulting from electron beam excitation in various gases is of interest in itself, since it may lead to a better understanding of atomic physics and to improvements in the electron beam technique.

(7) It is self-evident that the optical electron beam density probe can be applied to numerous gas dynamical problems in pure gases (e.g. for a study of boundary layers, wakes, turbulence, shocks etc.).

For electron beam studies in helium-argon mixtures or in pure argon the spatial resolution can be improved by choosing spectral lines, which do not show a fluorescent halo. In retrospect of the present study it appears to be advantageous to sacrifice intensity in favour of spatial resolution, thereby avoiding needless corrections. From that point of view the ArII lines between λ 4300Å and λ4500Å appear to be suitable. In the case of helium the fluorescent halo observed at λ 5016Å appears to have little effect on the spatial resolution except at very low densities.

REFERENCES

1.	Becker, E.W. Bier, K. Burghoff, H.	Die Trenndüse, ein neues Element zur Gas-und Isotopentrennung, Zeitschrift für Naturforschung, Vol. 10a, p. 565-572, 1955.
2.	Waterman, P.C. Stern, S.A.	Separation of Gas Mixtures in a Supersonic Jet, Journal of Chemical Physics, Vol. 31, p. 405-419, Aug. 1959.
3.	Stern, S.A. Waterman, P.C. Sinclair, T.F.	Separation of Gas Mixtures in a Supersonic Jet II. Behaviour of Helium-Argon Mixtures and Evidence of Shock Separation, Journal of Chemical Physics, Vol. 33, p. 805-813, Sept. 1960.
4.	Chow, R.R.	On the Separation Phenomena of a Binary Gas Mixture in an Axisymmetric Jet, University of California, Institute of Engineering Research Report HE-150-175, Nov. 1959.
5.	Chow, R.R.	Separation of Binary Gas Mixtures Behind a Curved Shock, Grumman Research Department Memorandum RM-295, Sept. 1965.
6.	Reis, V.H. Fenn, J.B.	Separation of Gas Mixtures in Supersonic Jets, Journal of Chemical Physics, Vol. 39, p. 3240 - 3250, Dec. 1963.
7.	Zigan, F.	Gasdynamische Berechnung der Trenndüsenentmischung, Zeitschrift für Naturforschung, Vol. 17a, p. 772-778, 1962.
8.	Sherman, F.S.	Hydrodynamical Theory of Diffusive Separation of Mixtures in a Free Jet, The Physics of Fluids, Vol. 8, p. 773-779, May 1965.
9.	Sherman, F.S.	Shock-Wave Structure in Binary Mixtures of Chemically Inert Perfect Gases, Journal of Fluid Mechanics, Vol. 8, p. 465-480, July 1960.
10.	Fujimoto, Tetsuo	Shock Wave Structure in Binary Gas Mixtures with no Chemical Reaction, Proceedings of the 4th International Symposium on Rarefied Gasdynamics at Toronto, 1964, edited by J.H. deLeeuw, Academic Press, N.Y. 1966.
11.	Oberai, M.M.	Kinetic-Theory Approach to the Problem of Shock-Wave Structure in a Binary Mixture, The Physics of Fluids, Vol. 8, p. 826-833, May 1965.
12.	Owen, P.L. Thornhill, C.K.	The Flow in an Axially Symmetric Supersonic Jet from a Nearly-Sonic Orifice into a Vacuum, Aero. Res. Council Report, R & M No. 2616, Great Britain, 1948.
13.	Sherman, F.S.	Self Similar Development of Inviscid Hypersonic Free-Jet Flows, Lockheed Report 6-90-63-61 (1963).
14.	Bier, K. Schmidt, B.	Zur Form der Verdichtungsstösse in frei expandierenden Gasstrahlen, Zeitschrift für angewandte Physik, Vol. 13, p. 493-500, 1961.

15.	Ashkenas, H. Sherman, F.S.	The Structure and Utilization of Supersonic Free Jets in Low Density Wind Tunnels, Proceedings of the 4th International Symposium on Rarefied Gasdynamics at Toronto, 1964, edited by J.H. deLeeuw, Academic Press, N.Y., 1966.
16.	Wilke, C.R.	A Viscosity Equation for Gas Mixtures, Journal of Chemical Physics, Vol. 18, p. 517-519, April 1950.
17.	Bird, R.B. Stewart, W.E. Lightfoot, E.N.	Transport Phenomena, John Wiley & Sons, New York, 1960.
18.	Schumacher, B.W. Gadamer, E.O.	Electron Beam Fluorescence Probe for Measuring the Local Gas Density in a Wide Field of Observation, Canadian Journal of Physics, Vol. 36, p. 659-671,1958.
19.	Gadamer, E.O.	Measurement of the Density Distribution in a Rarefied Gas Flow Using the Fluorescence Induced by a Thin Electron Beam, UTIA Report No. 83, University of Toronto, March 1962 - also AFOSR TN60-500
20.	Muntz, E.P. Marsden, D.J.	Electron Excitation Applied to the Experimental Investigation of Rarefied Gas Flows, Proceedings of the 3rd International Symposium on Rarefied Gasdynamics, Academic Press, Inc., New York, 1963.
21.	Enkenhus, K.R.	The Design, Instrumentation and Operation of the UTIA Low Density Wind Tunnel, UTIA Report No. 44, University of Toronto, June 1957.
22.	Harrison, G.R.	M.I.T. Wavelength Tables, Technology Press, Massachusetts Institute of Technology, John Wiley & Sons, New York,1939.
23.	Lees, J.H. Skinner, H.W.B.	Notes on the Excitation Processes in Helium, Proceedings of the Royal Society of London, Series A, Vol. 137, p. 186-198, 1932.
24.	Wolf, R. Maurer, W.	Versuche über Helium-Fluoreszenz und über die Gültigkeit des Spinerhaltungssatzes bei Stössen zweiter Art von angeregten mit normalen Helium-Atomen, Zeitschrift für Physik, Vol. 115, p. 410-430, 1940.
25.	Allen, C.W.	Astrophysical Quantities, University of London, Athlone Press, 1955.
26.	Bacher, R.F. Goudsmit, S.	Atomic Energy States, McGraw-Hill, 1932.
27.	Merrill, P.W.	Lines of the Chemical Elements in Astronomical Spectra, Carnegie Institution of Washington Publication 610, Washington, D.C.,1956.

28.	Olsen, H.N.	Measurement of Argon Transition Probabilities Using the Thermal Arc Plasma as a Radiation Source, Journal of Quantitative Spectroscopy and Radiative Transfer, Vol.3, p. 59-76, 1963.
29.	Knox, R.S.	Excited-State Wave Functions, Excitation Energies, and Oscillator Strengths for Argon ($3p^5$ 4s), Physical Review, Vol. 110, p. 375-381, 1958.
30.	Rothe, D.E.	Flow Visualization Using a Traversing Electron Beam, AIAA Journal, Vol. 3, p. 1945-1946, October 1965.
31.	Talbot, L.	Survey of the Shock Structure Problem, ARS Journal, Vol. 32, p. 1009-1016, July 1962.
32.	Sherman, F.S.	A Low Density Wind Tunnel Study of Shockwave Structure and Relaxation Phenomena in Gases, University of California, Institute of Engineering Research Report No. HE-150-122, May 1954.
33.	Hansen, K. Hornig,D.F. Levitt, B. Myers, B.F. Linzer, M.	Thickness of Shock and Detonation Fronts and Rotational Relaxation at High Temperatures, Rarefied Gasdynamics, edited by L. Talbot, Academic Press, N.Y. 1961,p.593
34.	Camac, M.	Argon and Nitrogen Shock Thicknesses, Aerospace Sciences Meeting at New York, Jan. 1964, AIAA Preprint No. 64-35.
35.	Kieffer, L.J. Dunn, G.H.	Electron Impact Ionization Cross-Section Data for Atoms, Atomic Ions, and Diatomic Molecules, Reviews of Modern Physics, Vol. 38, p. 1 - 35, Jan. 1966.
36.	Anderson, J.B. Andres, R.P. Fenn, J.B. Maise, G.	Studies of Low Density Supersonic Jets, Proceedings of the 4th International Symposium on Rarefied Gasdynamics at Toronto, 1964, edited by J.H. de Leeuw, Academic Press, N.Y. 1966.
37.	Milne, T.A.	Mass Spectrometer Study of Metal - Containing Flames, 7th Quarterly Technical Summary Report, Midwest Research Institute, Kansas City, 1963.
38.	Greene, F.T. Milne, T.A.	Mass Spectrometric Detection of Polymers in Supersonic Molecular Beams, Journal of Chemical Physics, Vol. 39, p. 3150 - 3151, December 1963.
39.	Muntz, E.P.	Measurement of Rotational Temperature, Vibrational Temperature, and Molecule Concentration in Non-Radiating Flows of Low Density Nitrogen, UTIA Report No. 71, University of Toronto, April 1961. Also, Physics of Fluids, Vol. 5, p. 80, 1962.

BLANK PAGE

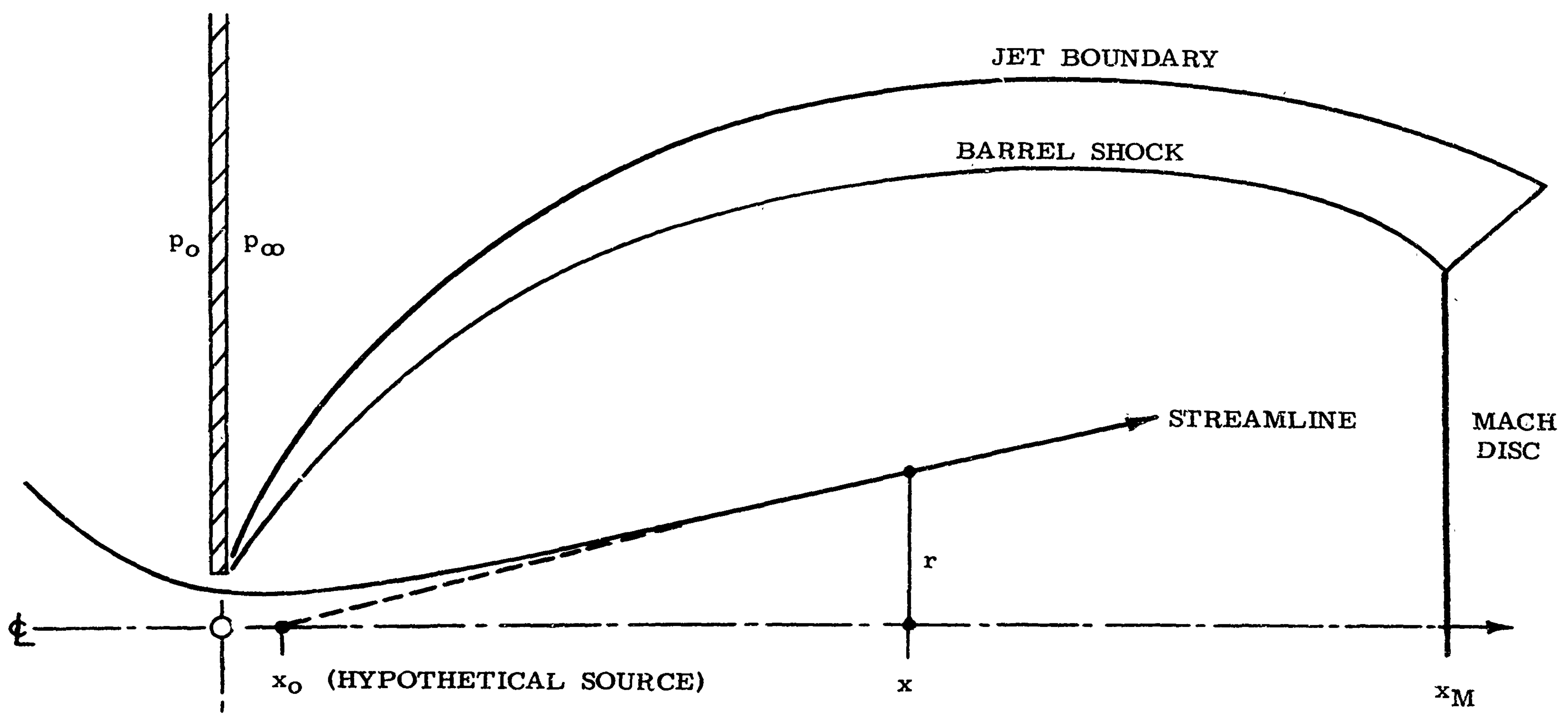

FIG. 2.1 SKETCH OF FREE JET FLOW FIELD

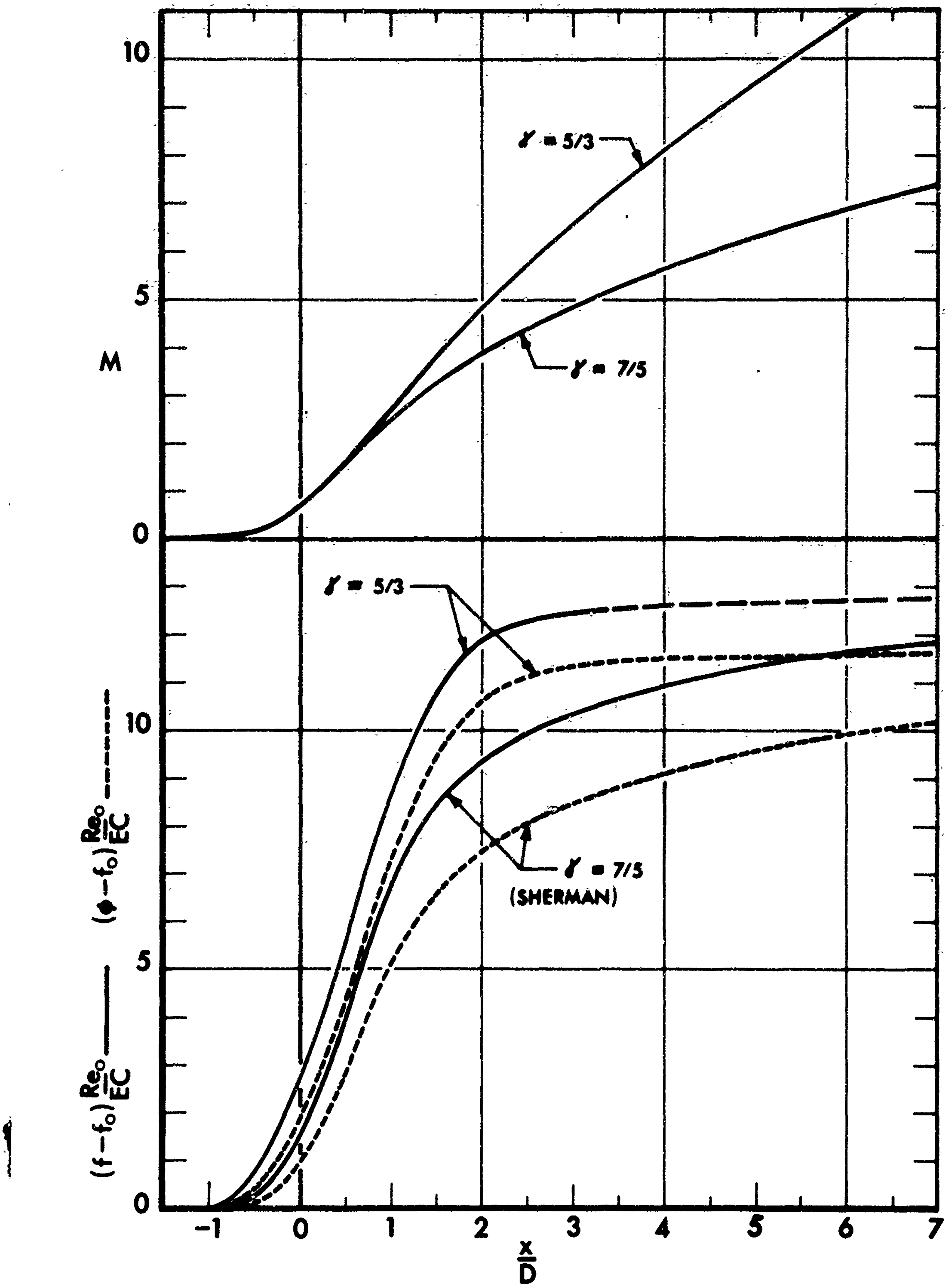

FIG. 2.2 THEORETICAL MACH NUMBER VARIATION AND DIFFUSIVE SEPARATION EFFECTS ALONG THE AXIS OF AN UNDER-EXPANDED FREE JET

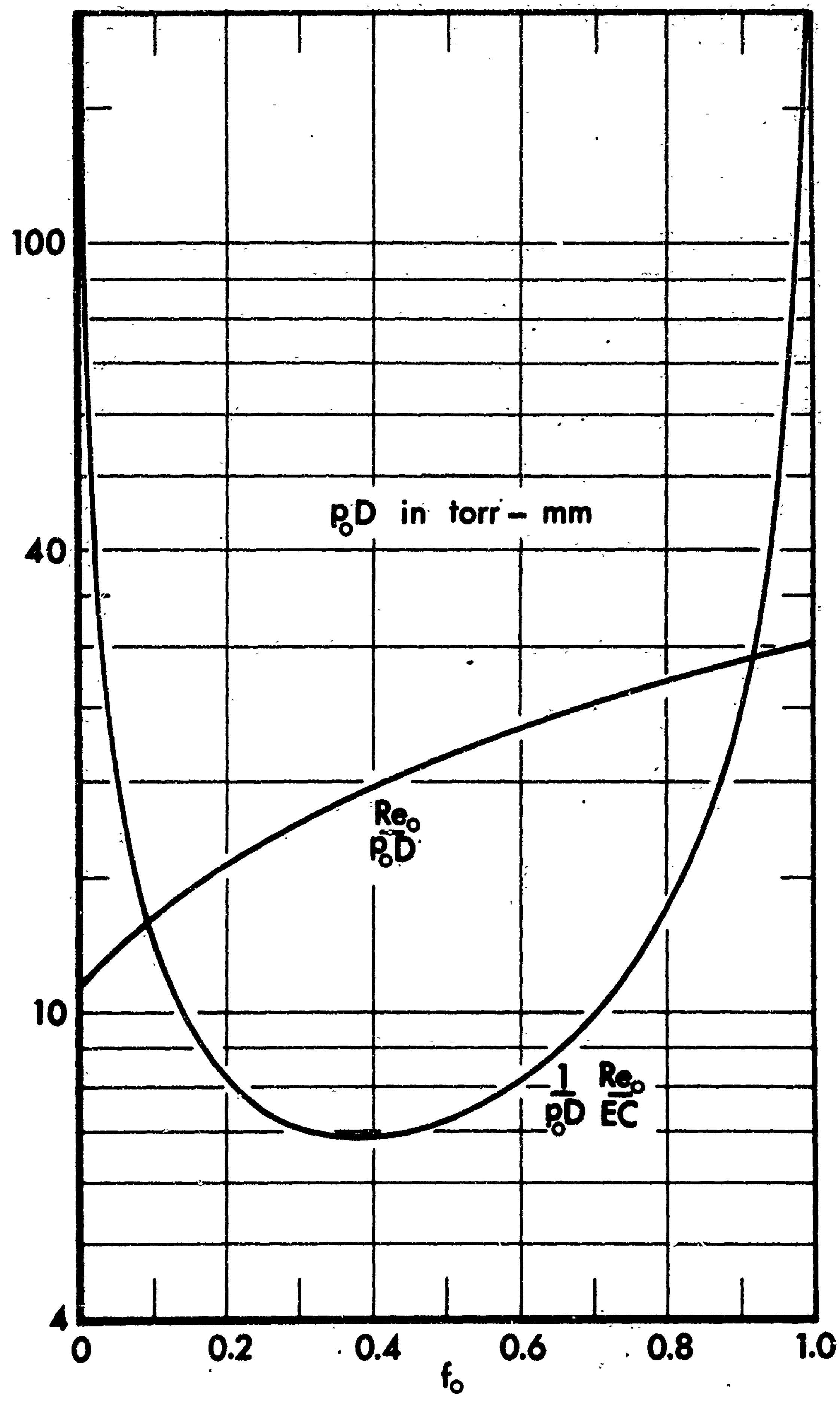

FIG. 2. 3 THEORETICAL DEPENDENCE OF THE REYNOLDS NUMBER AND OF THE PARAMETER Re_o/EC ON THE GAS COMPOSITION FOR ARGON-HELIUM MIXTURES

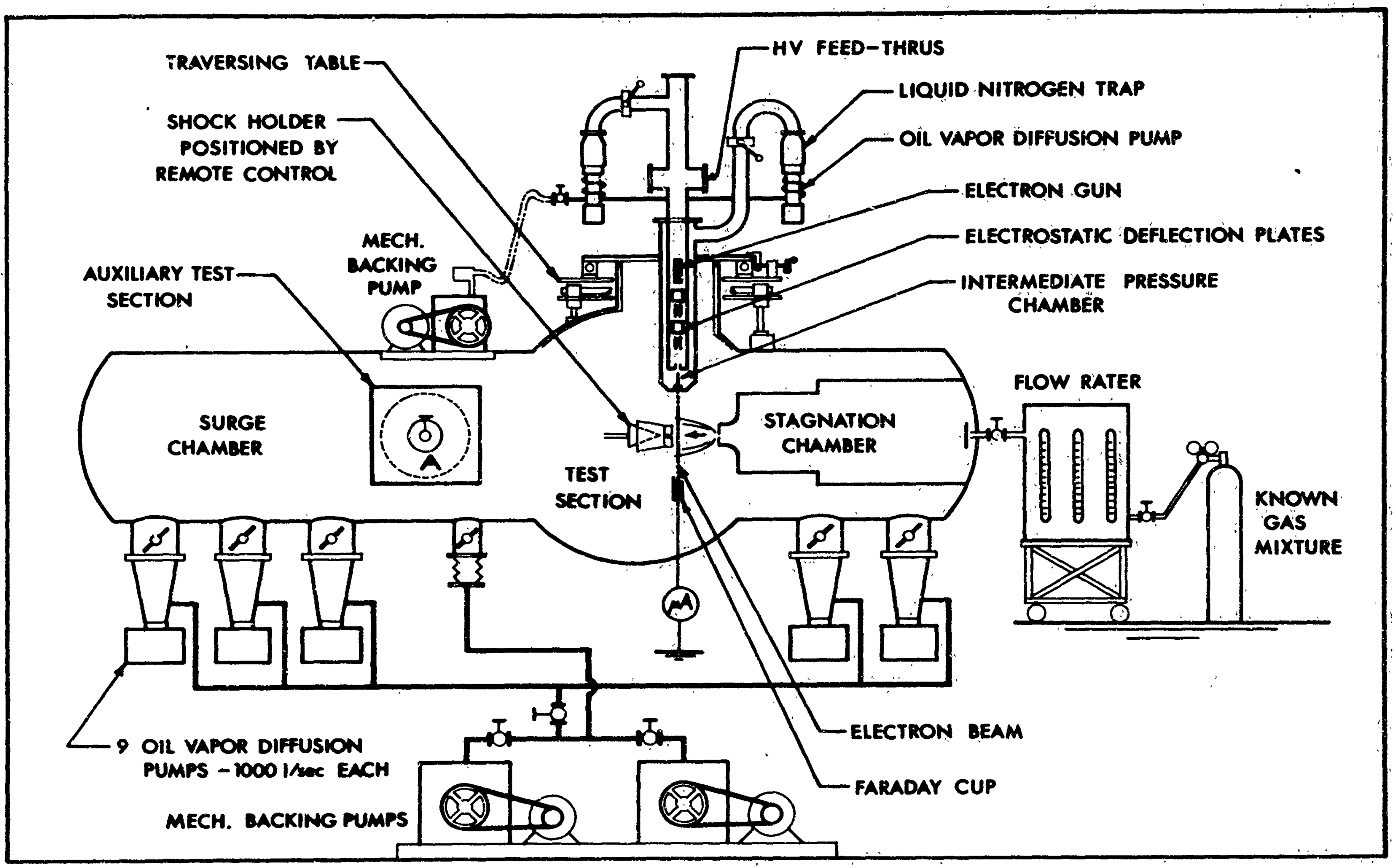

FIG. 4.1 SCHEMATIC DIAGRAM OF THE LOW DENSITY TUNNEL WITH ELECTRON GUN

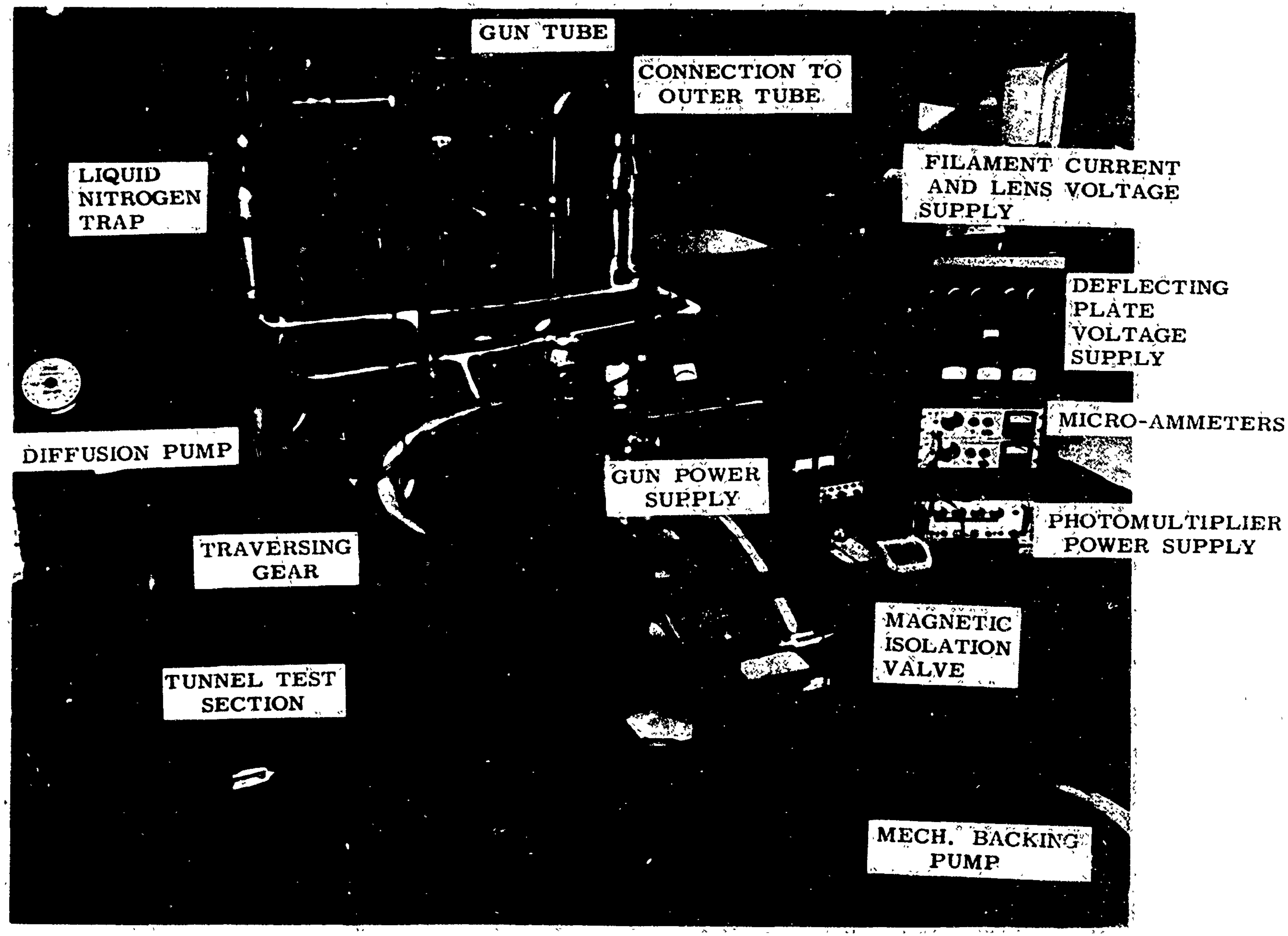

FIG. 4.2 EXTERNAL VIEW OF GUN ASSEMBLY AND INSTRUMENTATION

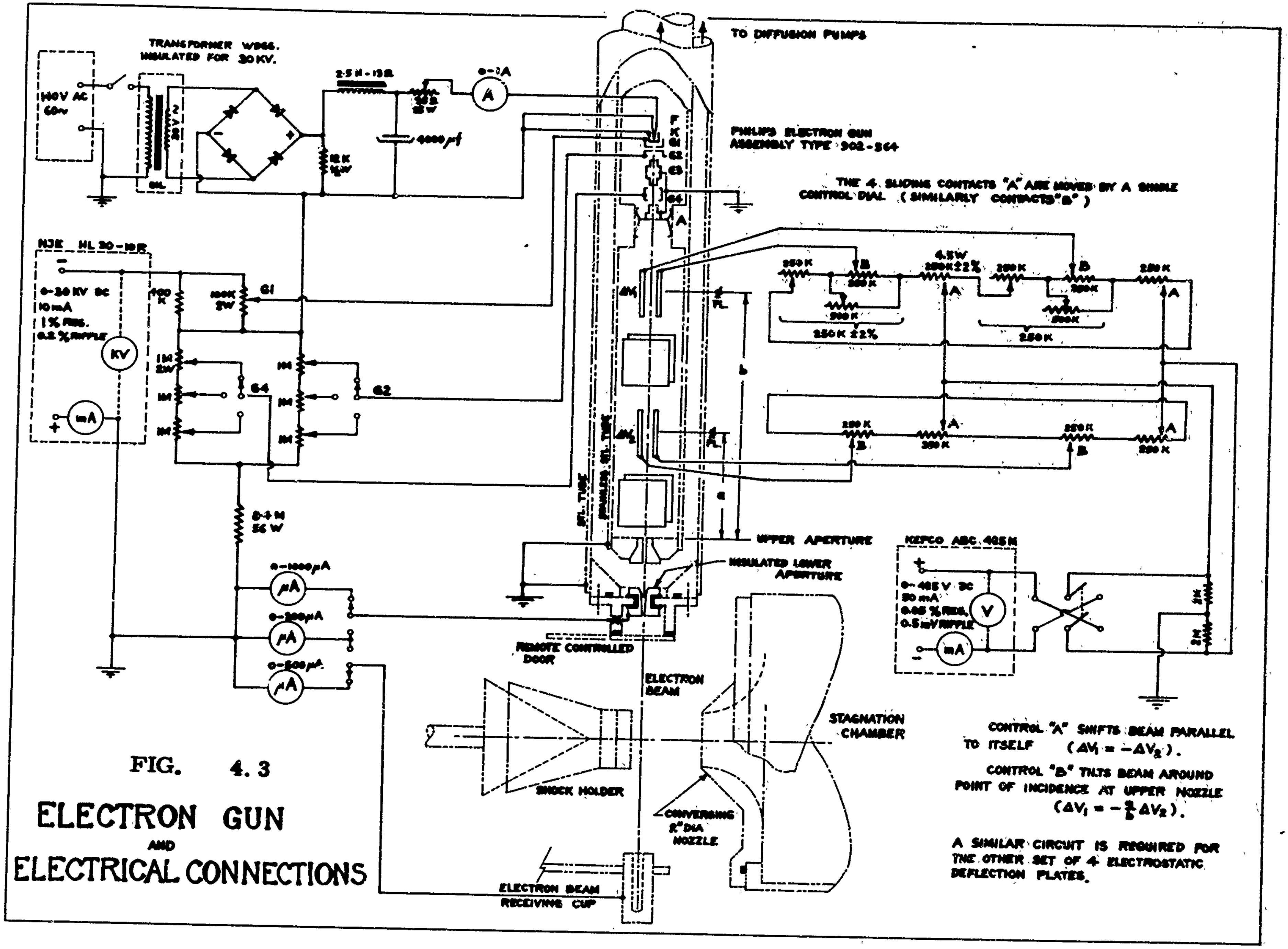

FIG. 4.3

ELECTRON GUN
AND
ELECTRICAL CONNECTIONS

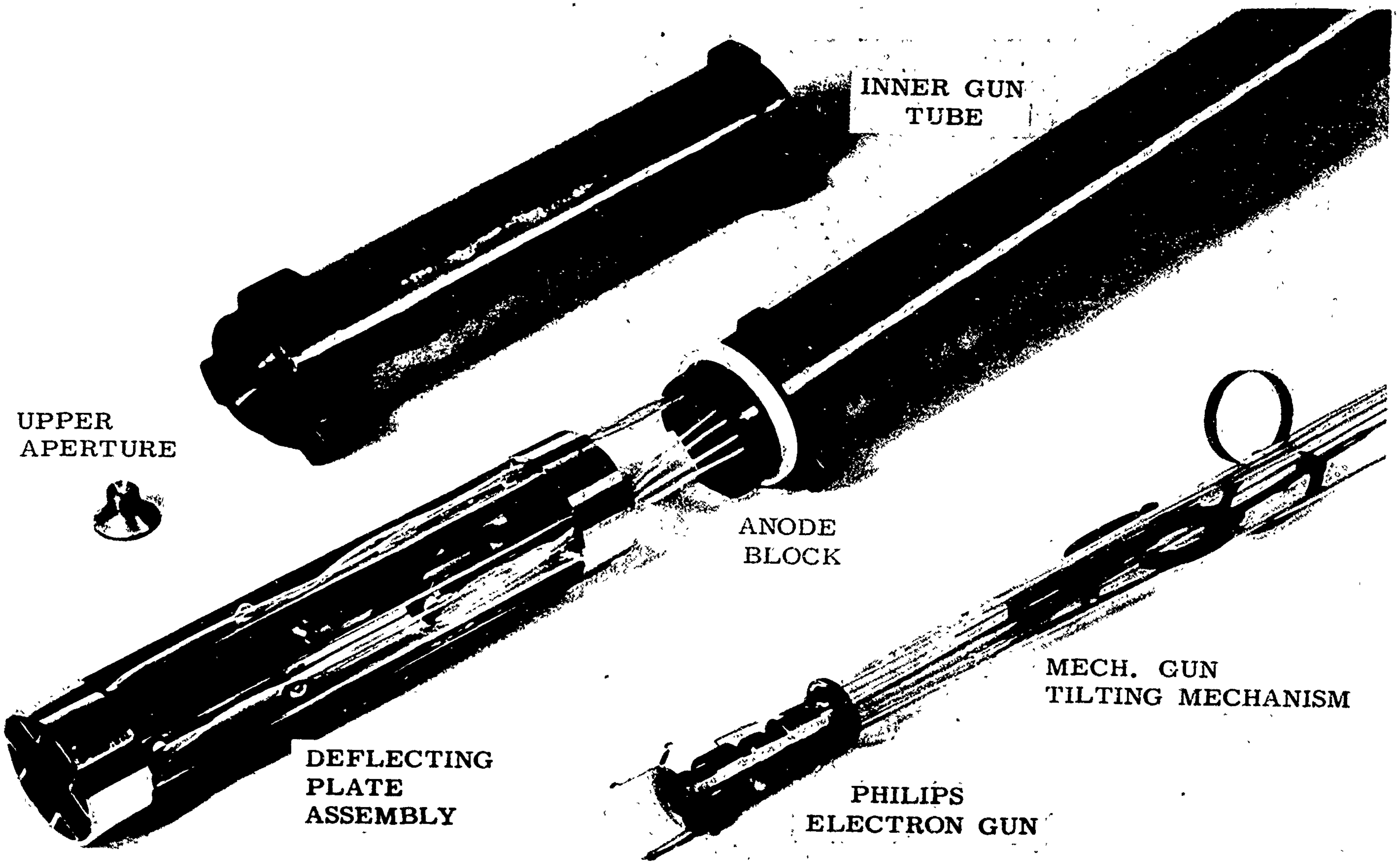

FIG. 4.4 DEFLECTING PLATE ASSEMBLY AND INNER GUN CHAMBER

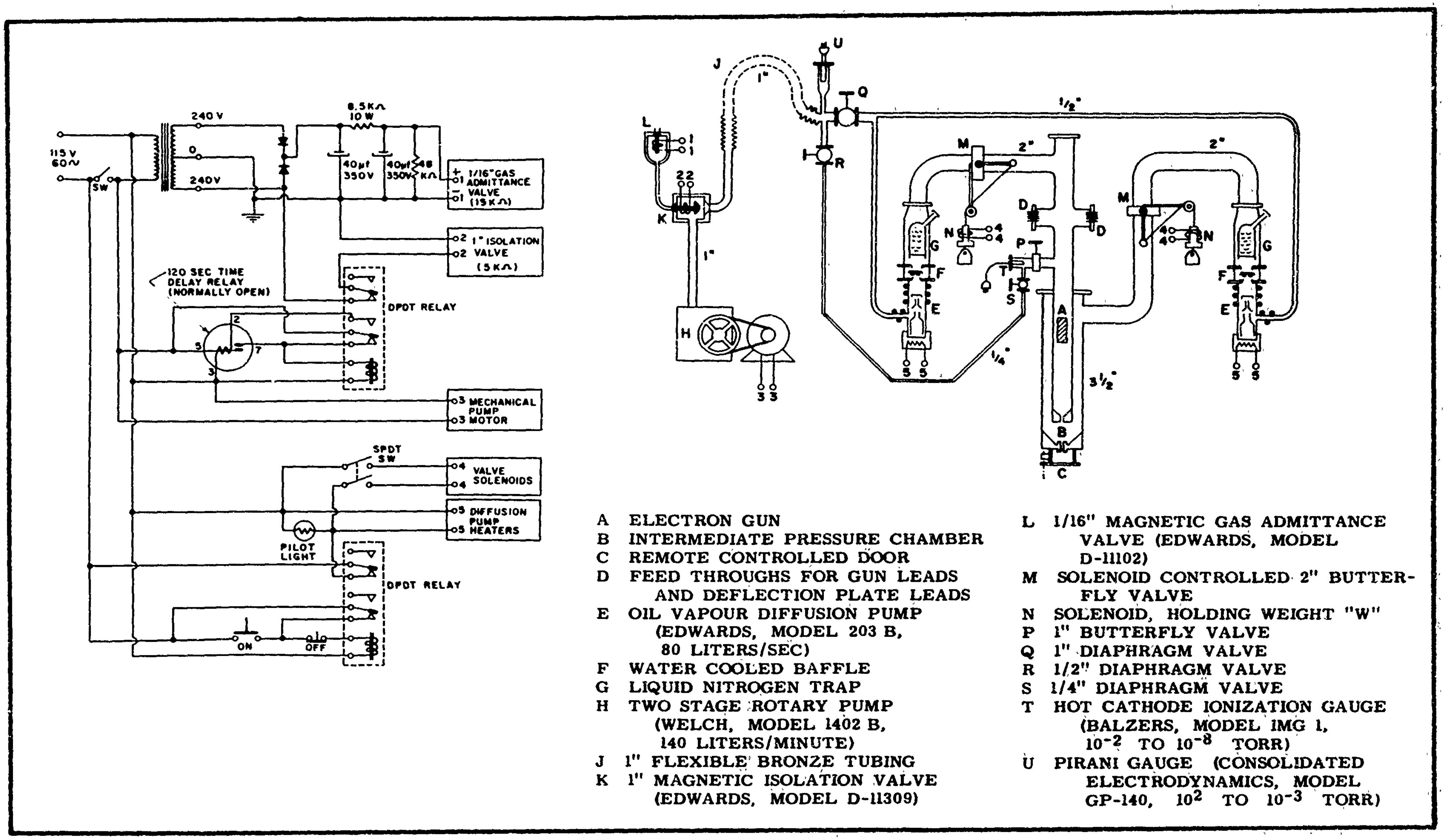

A	ELECTRON GUN
B	INTERMEDIATE PRESSURE CHAMBER
C	REMOTE CONTROLLED DOOR
D	FEED THROUGHS FOR GUN LEADS AND DEFLECTION PLATE LEADS
E	OIL VAPOUR DIFFUSION PUMP (EDWARDS, MODEL 203 B, 80 LITERS/SEC)
F	WATER COOLED BAFFLE
G	LIQUID NITROGEN TRAP
H	TWO STAGE ROTARY PUMP (WELCH, MODEL 1402 B, 140 LITERS/MINUTE)
J	1" FLEXIBLE BRONZE TUBING
K	1" MAGNETIC ISOLATION VALVE (EDWARDS, MODEL D-11309)
L	1/16" MAGNETIC GAS ADMITTANCE VALVE (EDWARDS, MODEL D-11102)
M	SOLENOID CONTROLLED 2" BUTTERFLY VALVE
N	SOLENOID, HOLDING WEIGHT "W"
P	1" BUTTERFLY VALVE
Q	1" DIAPHRAGM VALVE
R	1/2" DIAPHRAGM VALVE
S	1/4" DIAPHRAGM VALVE
T	HOT CATHODE IONIZATION GAUGE (BALZERS, MODEL IMG 1, 10^{-2} TO 10^{-8} TORR)
U	PIRANI GAUGE (CONSOLIDATED ELECTRODYNAMICS, MODEL GP-140, 10^{2} TO 10^{-3} TORR)

FIG. 4.3 SCHEMATIC DIAGRAM OF PUMPING CONNECTIONS AND PROTECTIVE DEVICES

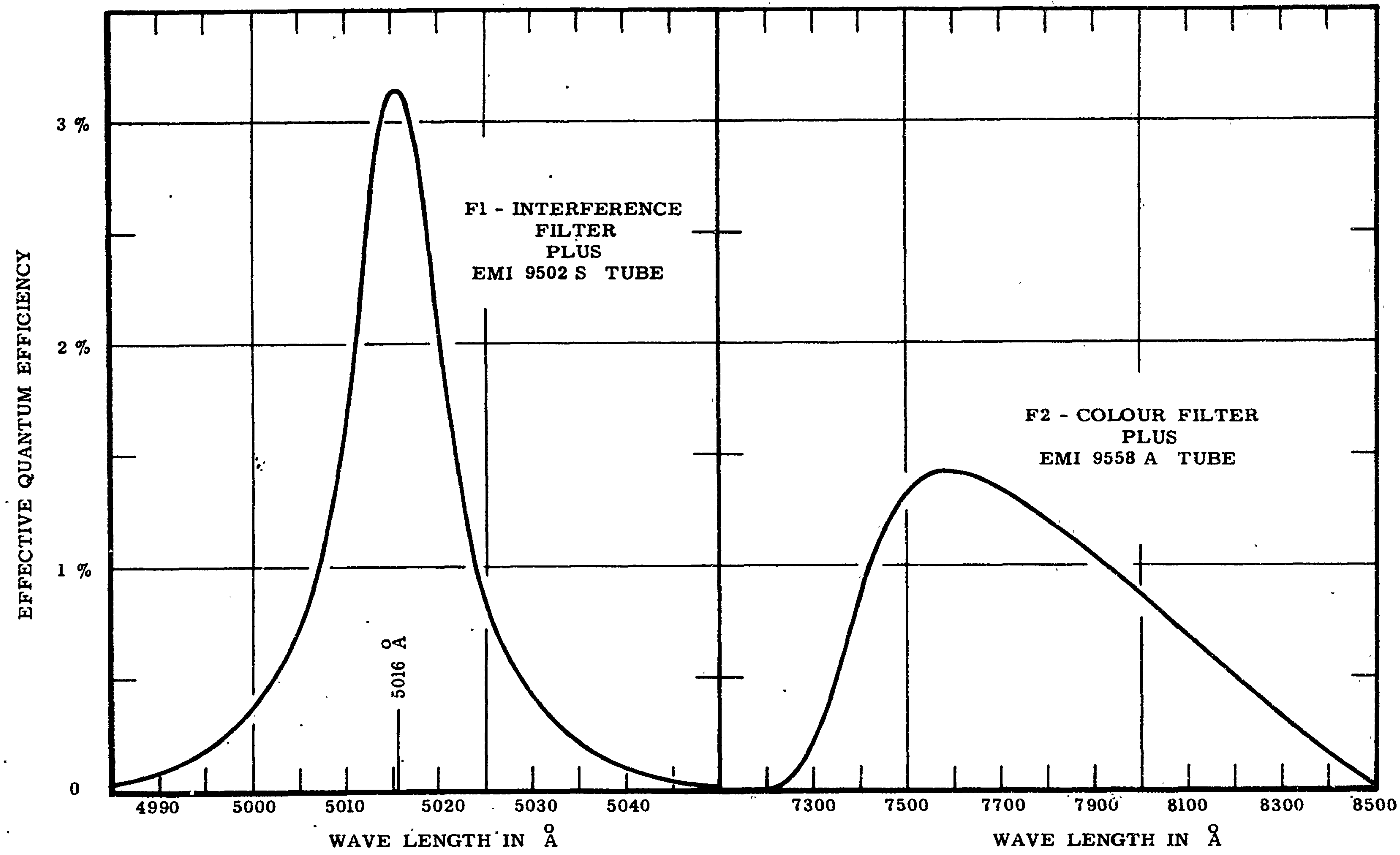

FIG. 4.6 SPECTRAL SENSITIVITY CURVES FOR THE PHOTOMULTIPLIER - FILTER COMBINATIONS

FIG. 4.7 ORIGINAL DESIGN OF THE OPTICAL ANALYZER

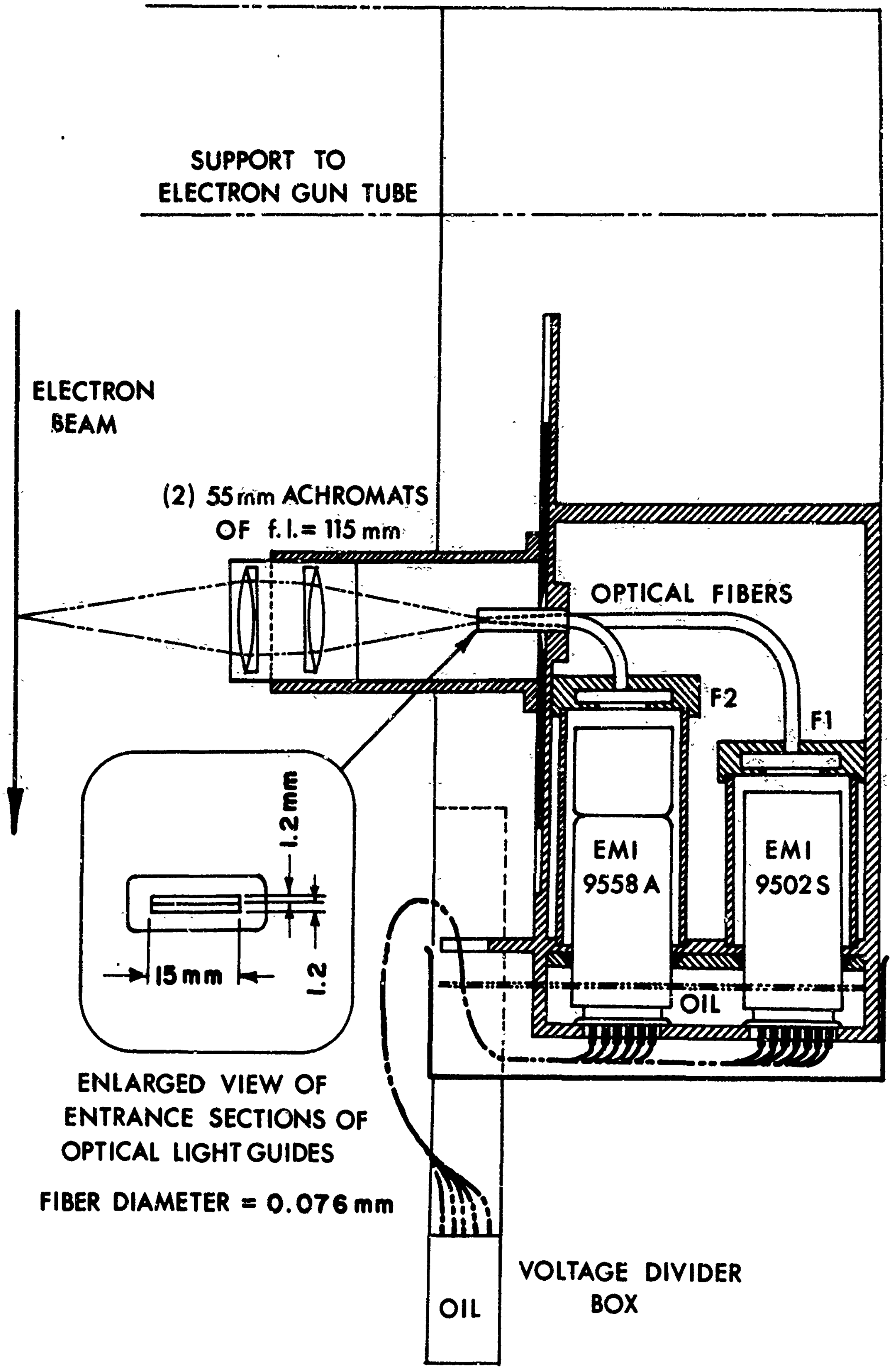

FIG. 4.8 MODIFIED VERSION OF THE OPTICAL ANALYZER AS USED FOR MOST OF THE EXPERIMENTAL TESTS

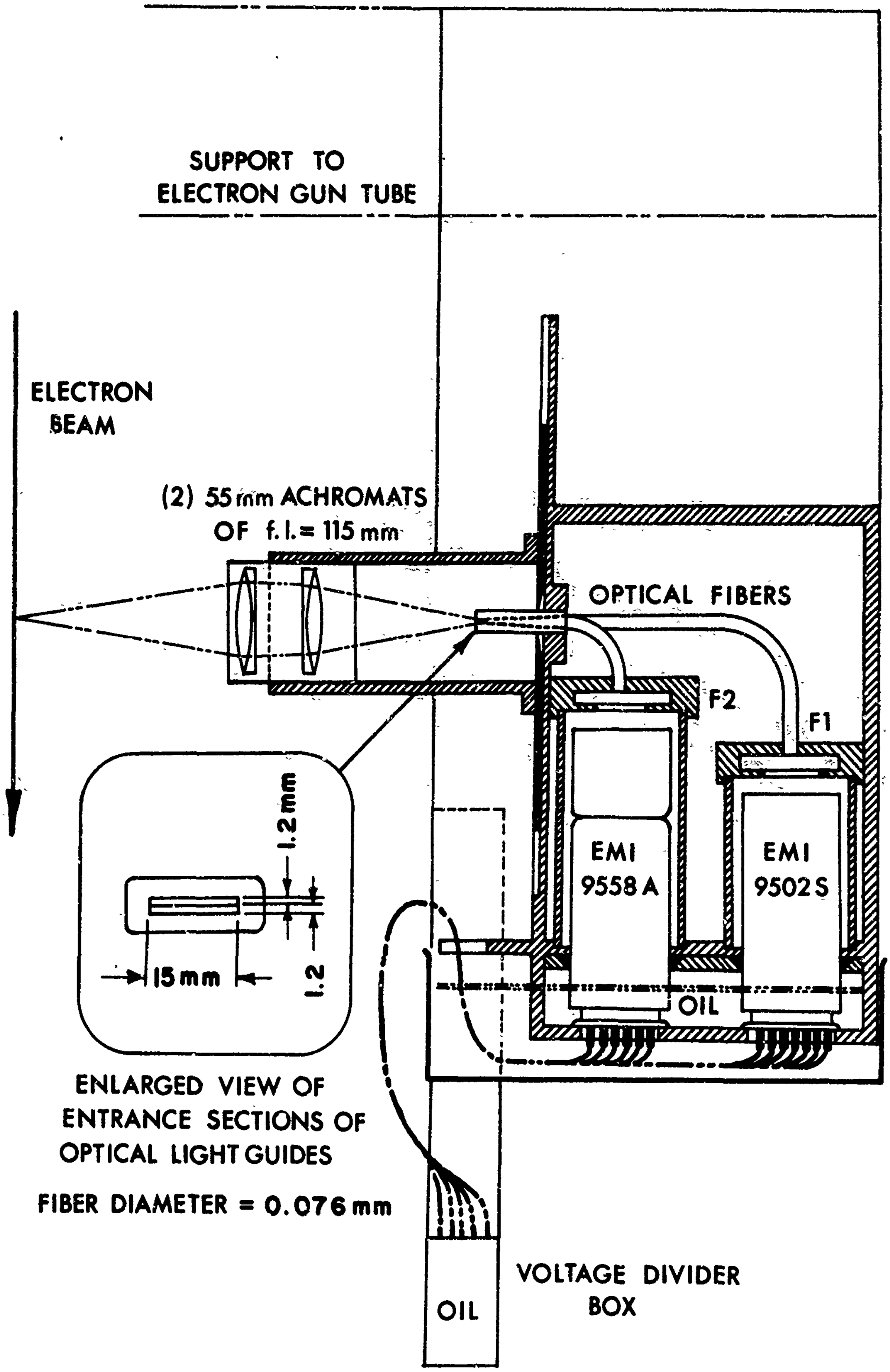

FIG. 4.8 MODIFIED VERSION OF THE OPTICAL ANALYZER AS USED FOR MOST OF THE EXPERIMENTAL TESTS

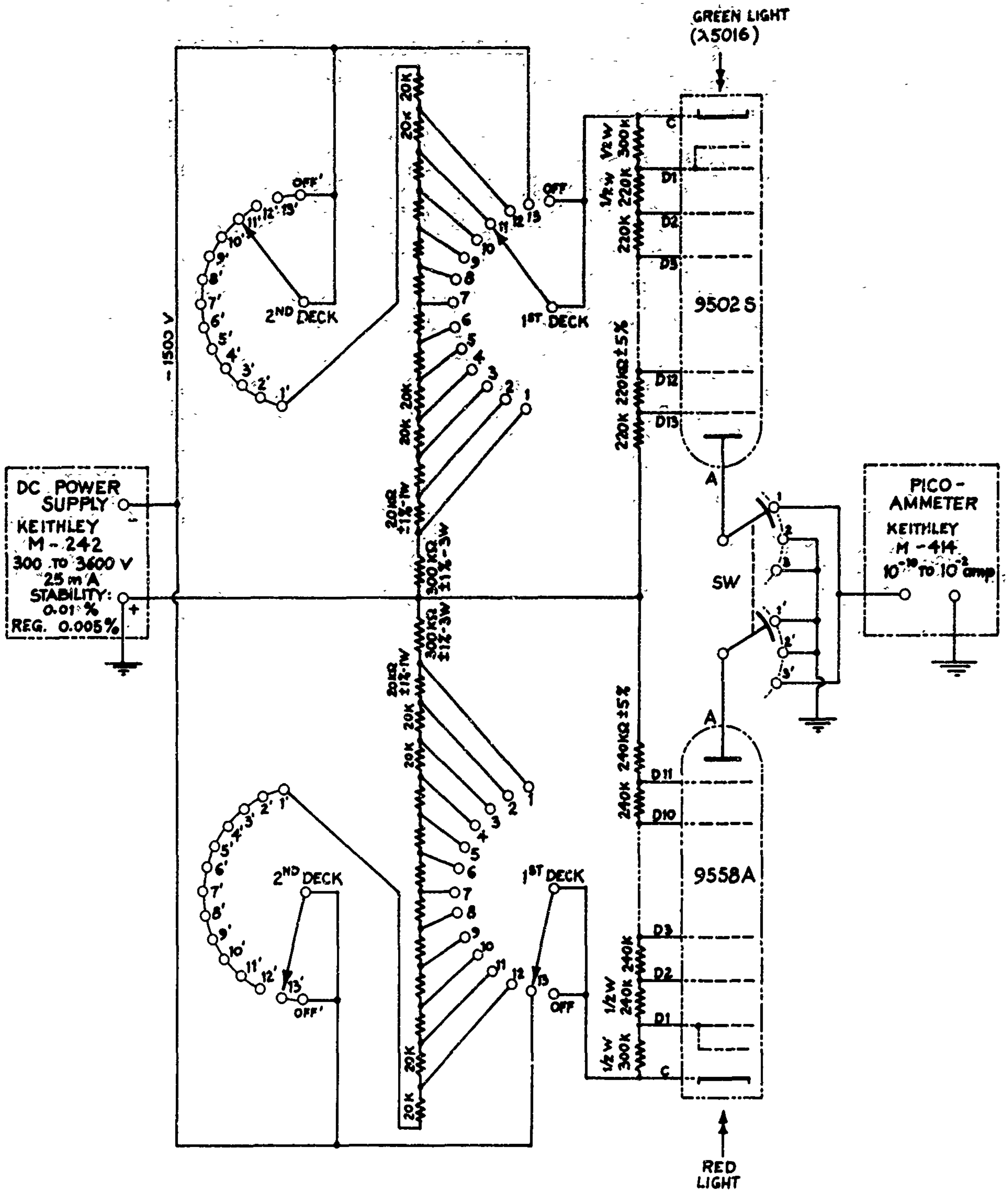

FIG. 4.9 WIRING DIAGRAM FOR PHOTOMULTIPLIER TUBES

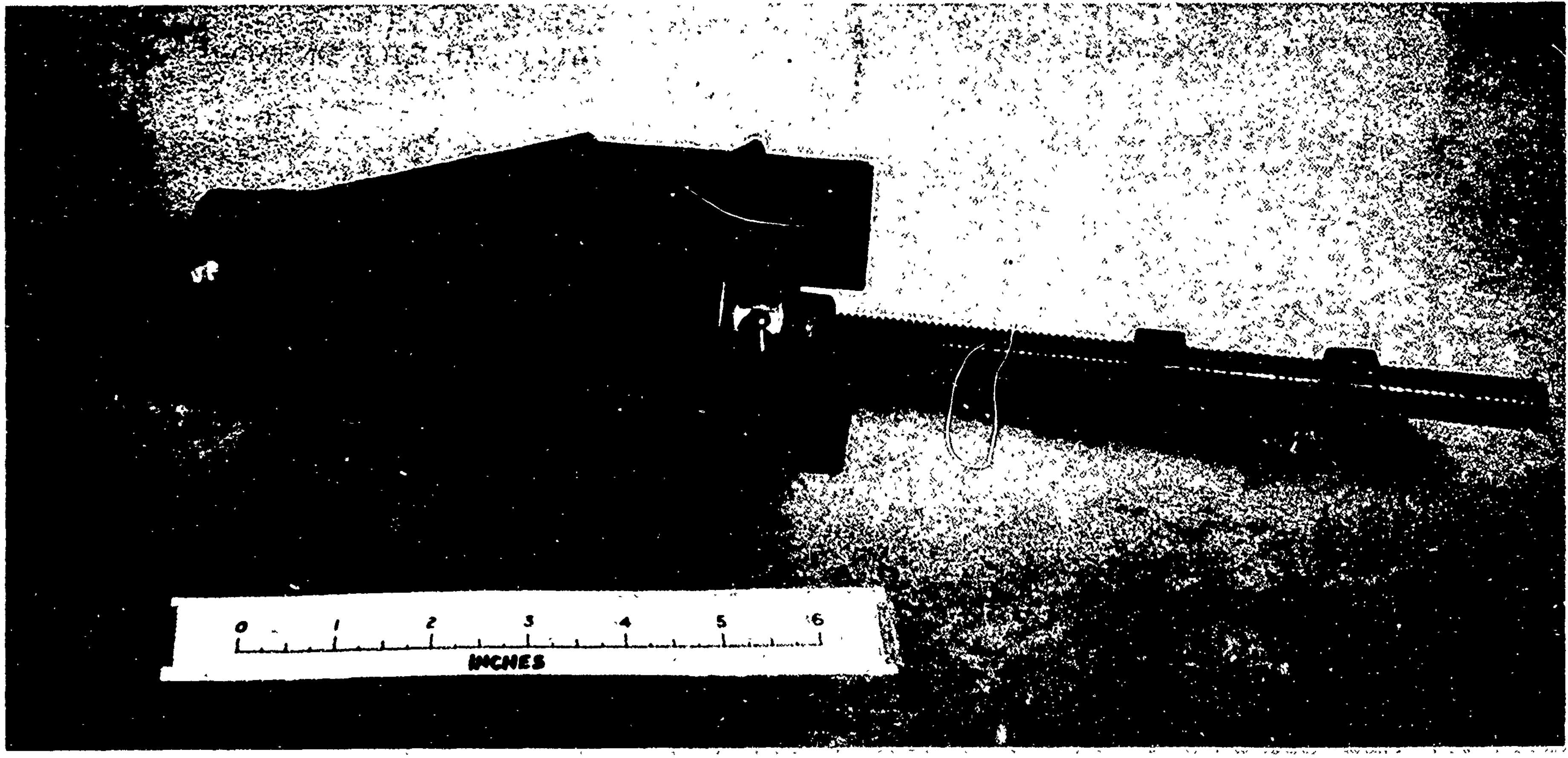

FIG. 4.10 SHOCK HOLDER

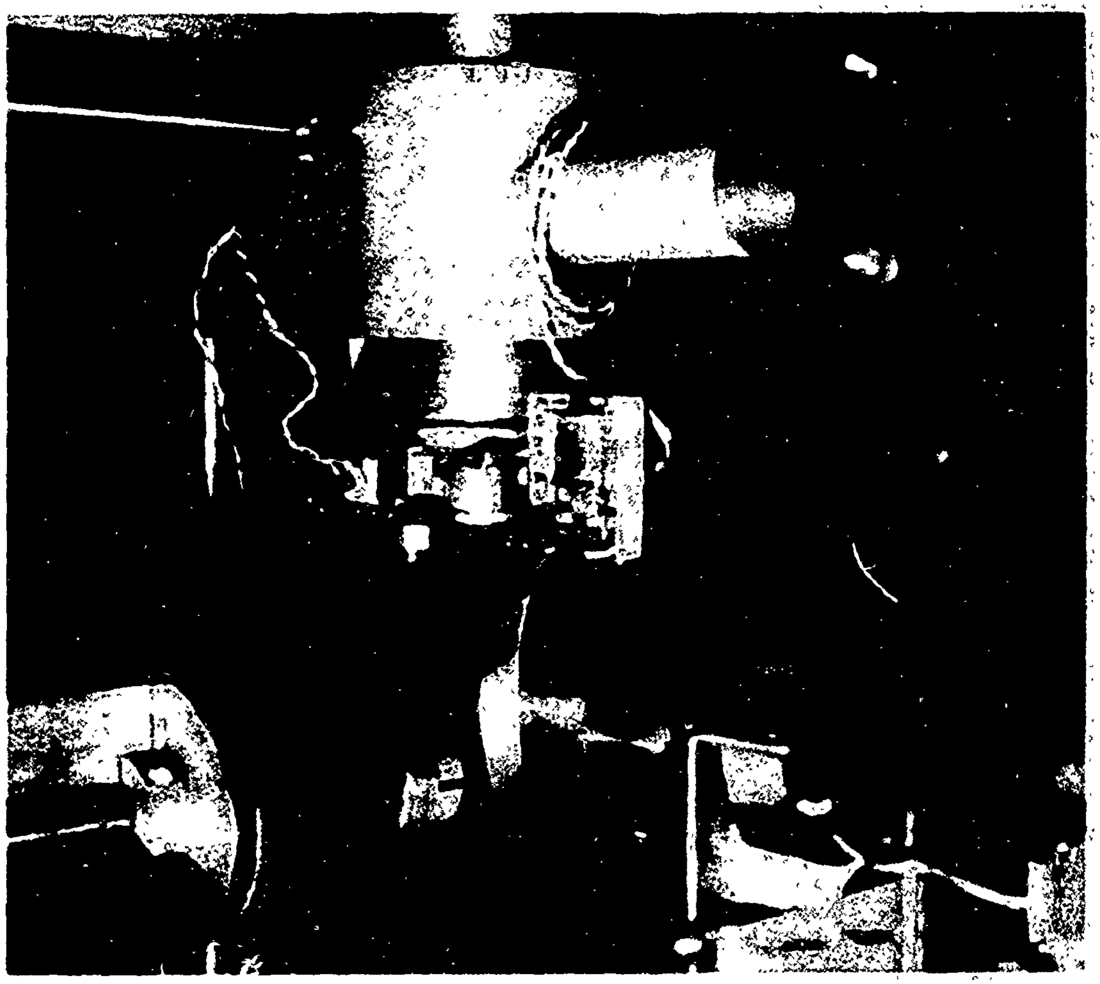

FIG. 4.11 VIEW SHOWING THE RELATIVE POSITIONS OF ELECTRON GUN, NOZZLE, SHOCK HOLDER, AND OPTICAL ANALYZER

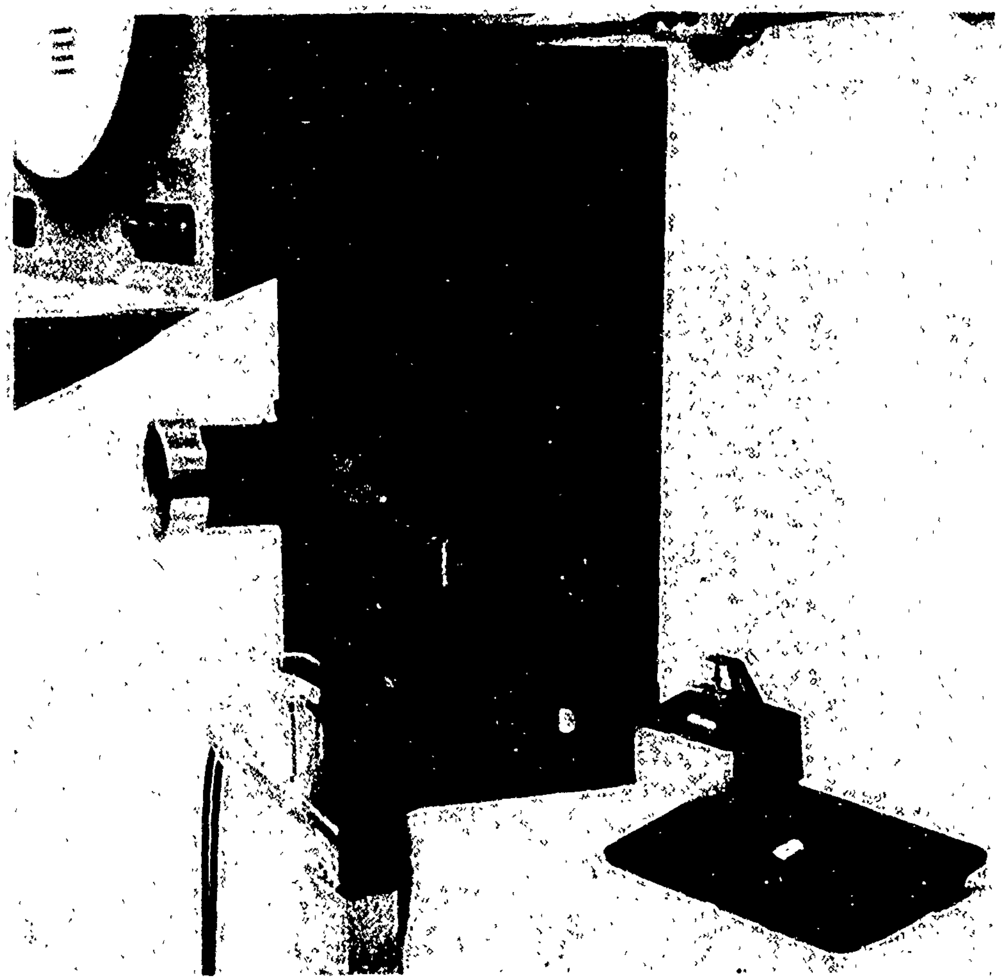

FIG. 4.12 EXTERNAL VIEW OF OPTICAL ANALYZER (ORIGINAL VERSION) WITH HANDHOLE COVER REMOVED

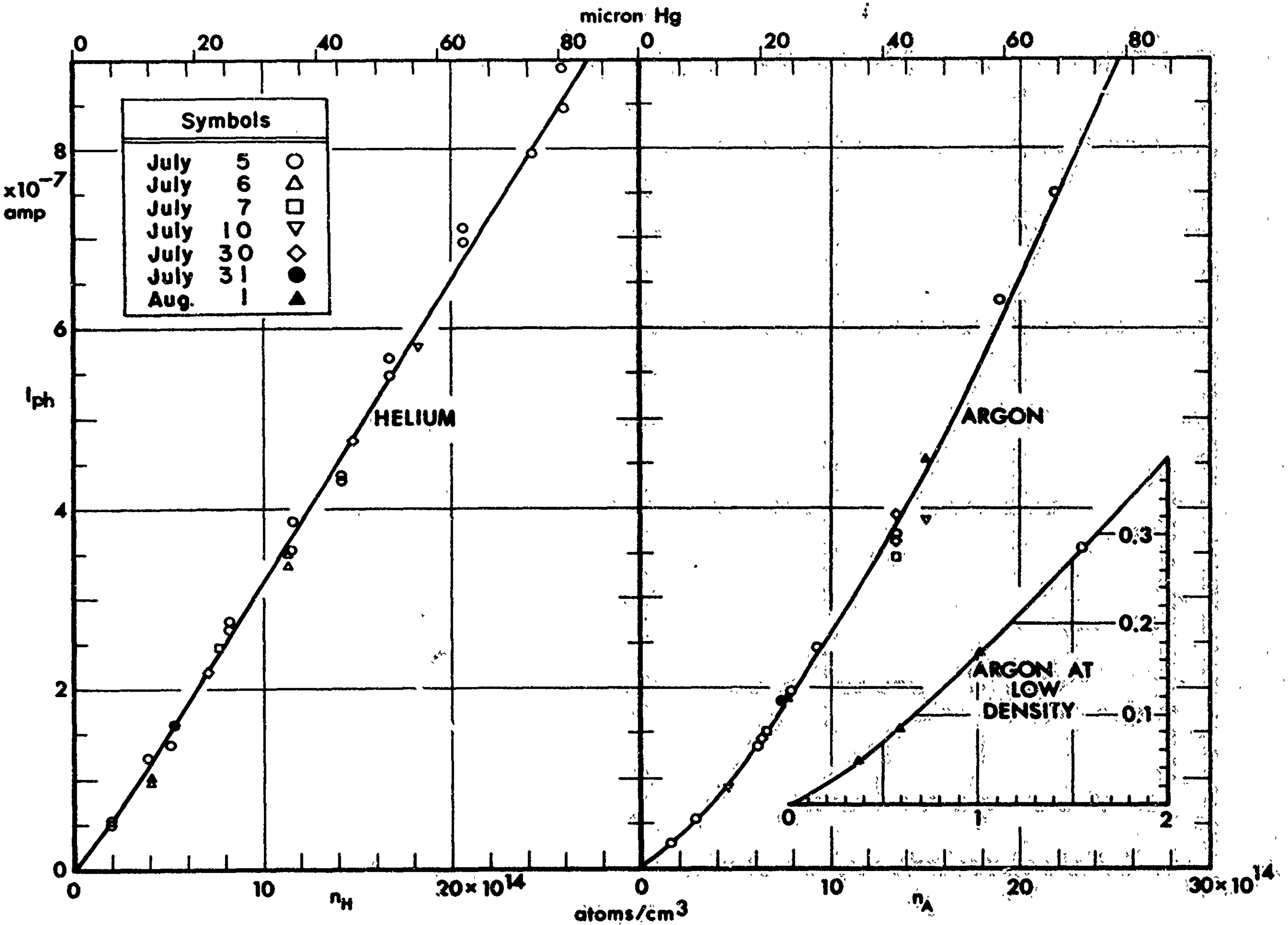

FIG. 5.1 PURE GAS CALIBRATION CURVES OF PHOTOMULTIPLIER CURRENT AGAINST GAS DENSITY

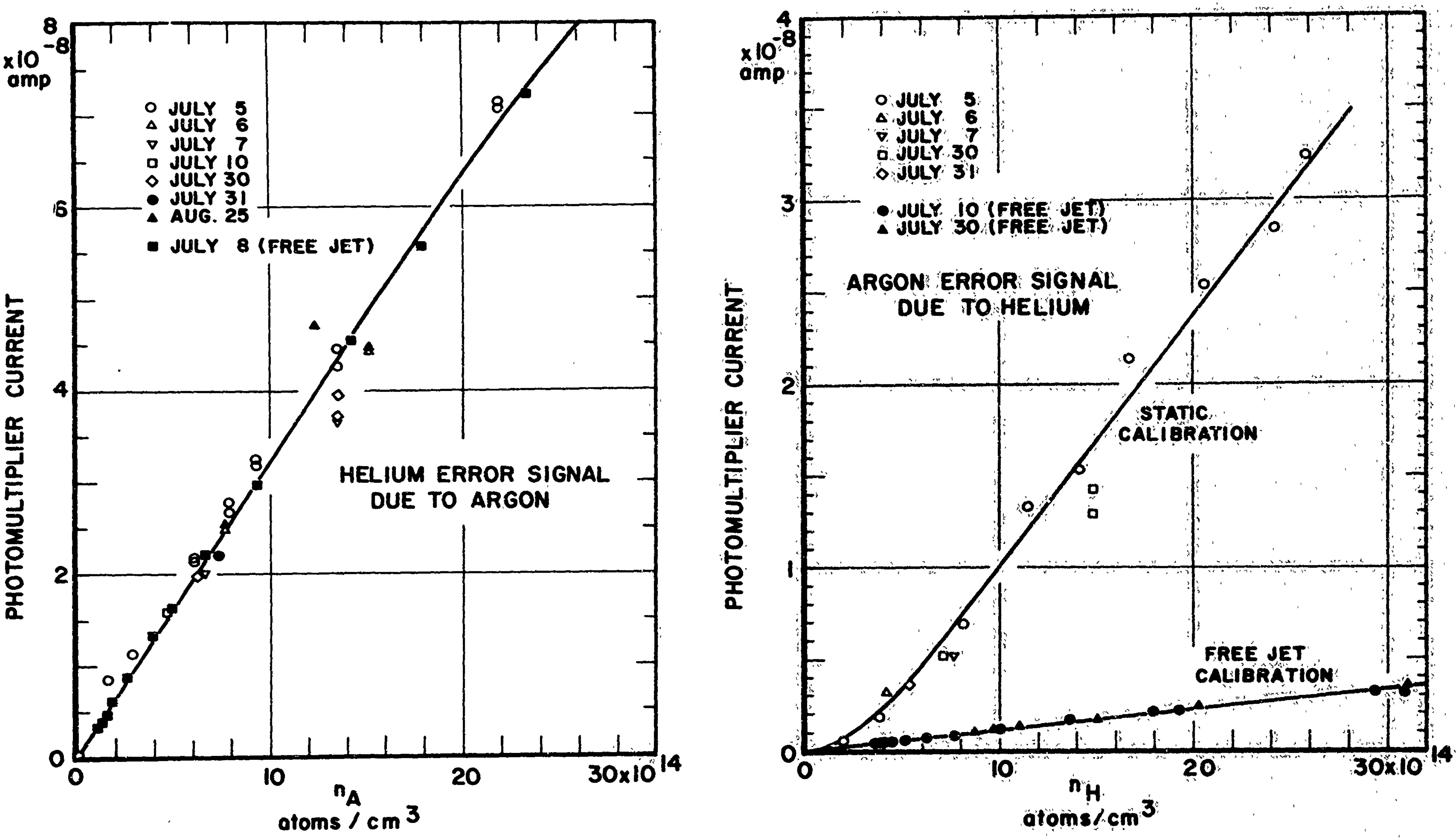

FIG. 5.2 ERROR SIGNAL CALIBRATION CURVES OBTAINED WITH PURE GASES

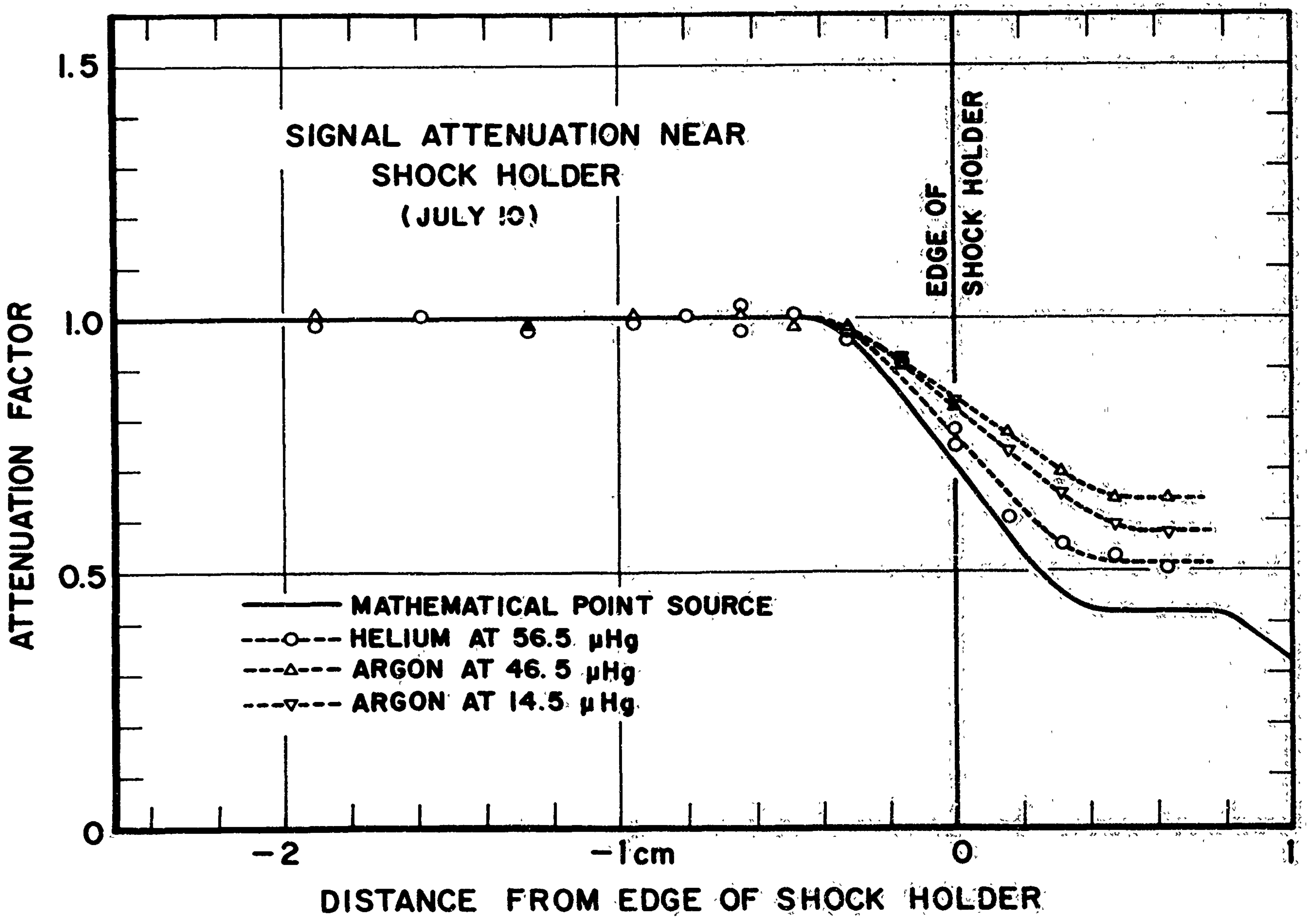

FIG. 5.3 ARGON AND HELIUM SIGNAL ATTENUATION CAUSED BY THE INTERCEPTION AND REFLECTION OF LIGHT BY THE SHOCK HOLDER SURFACES

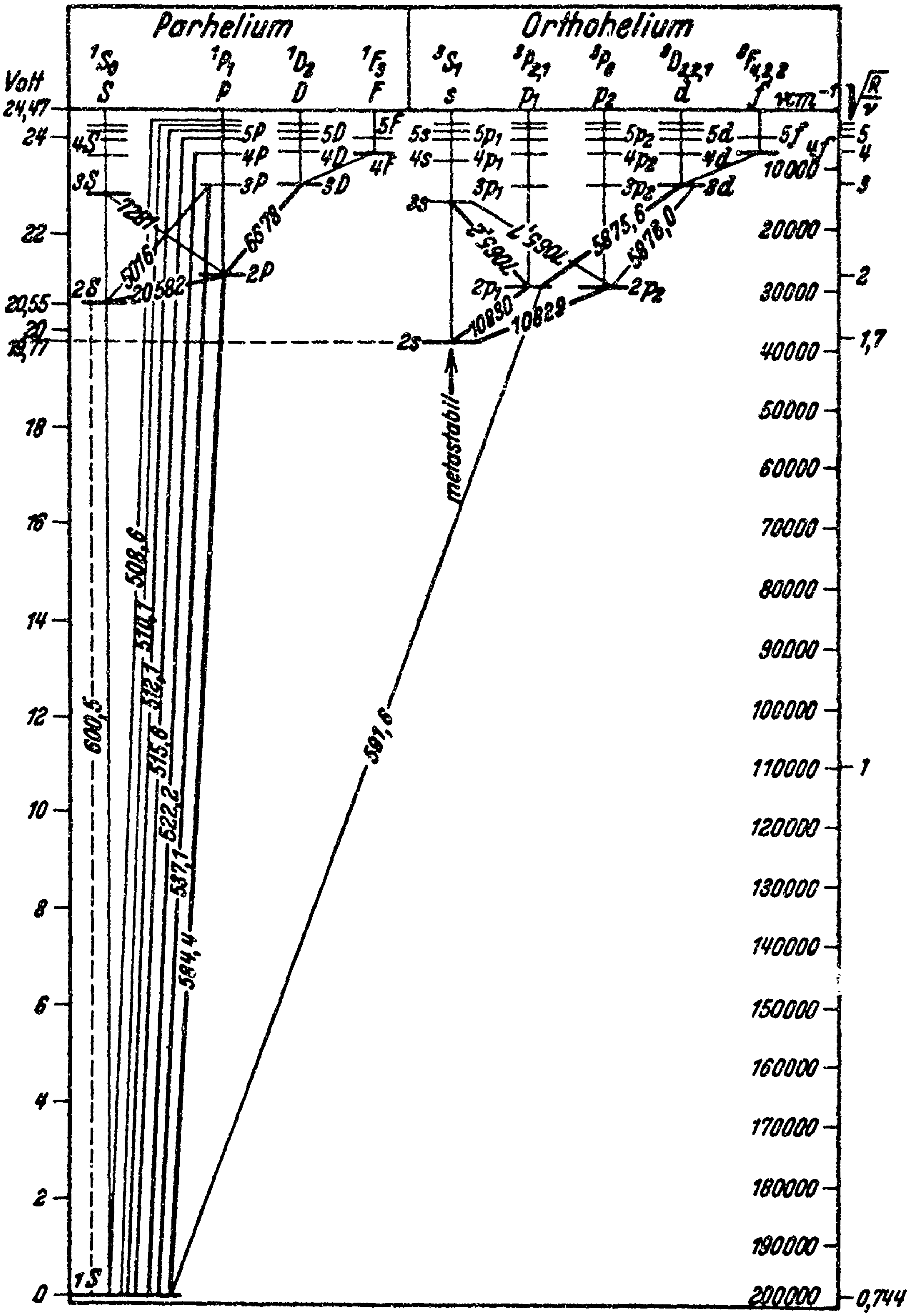

FIG. 5.4 ENERGY LEVEL DIAGRAM FOR NEUTRAL HELIUM (taken from Ref. 24)

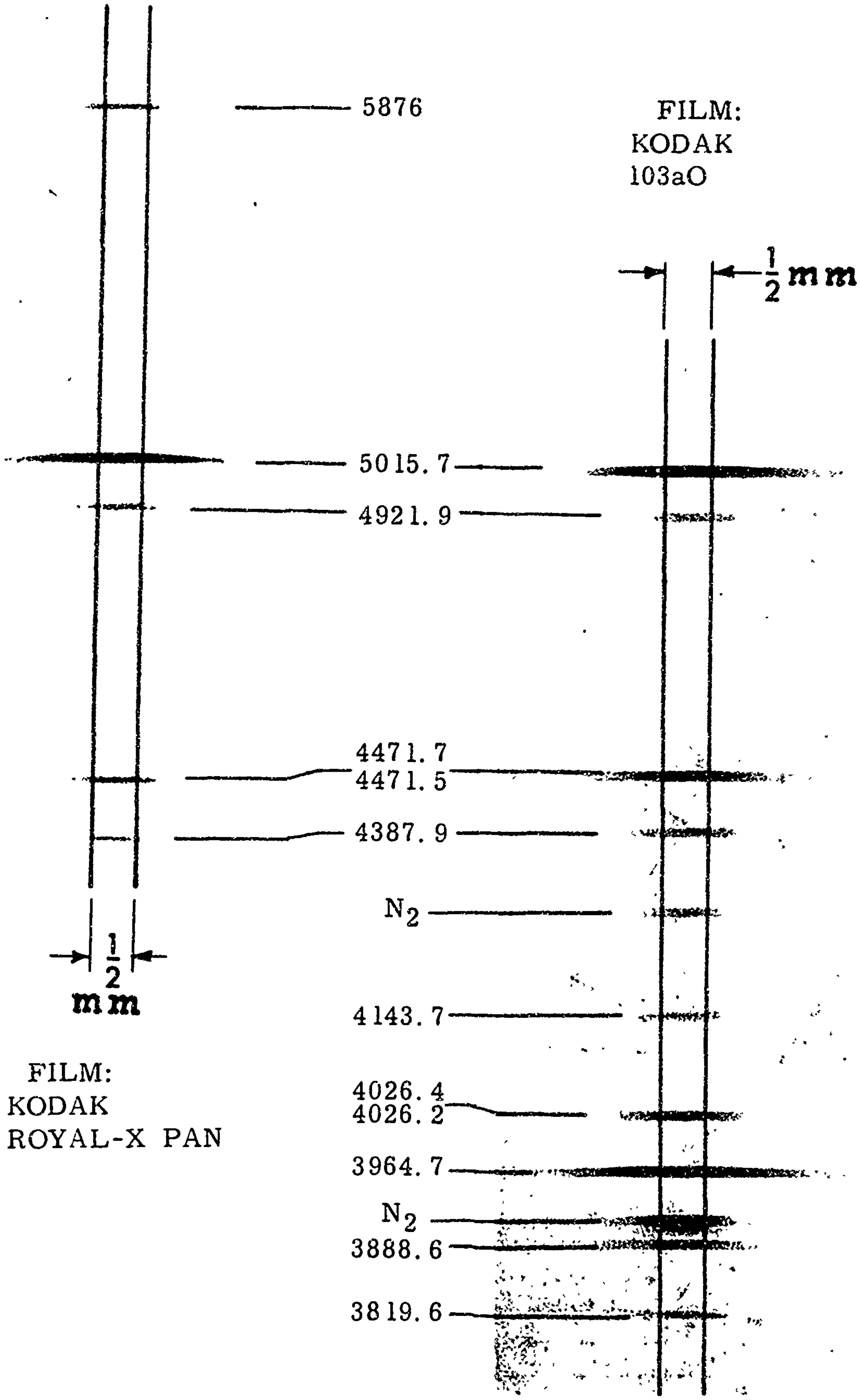

FIG. 5.5 ELECTRON BEAM EXCITED SPECTRUM OF HELIUM.
THE 1/2 mm WIDE ELECTRON BEAM IS AT RIGHT ANGLES TO THE SPECTROGRAPH SLIT
ELECTRON BEAM: 17.5 kv - 200 μ amp
HELIUM PRESSURE: 100 μ Hg

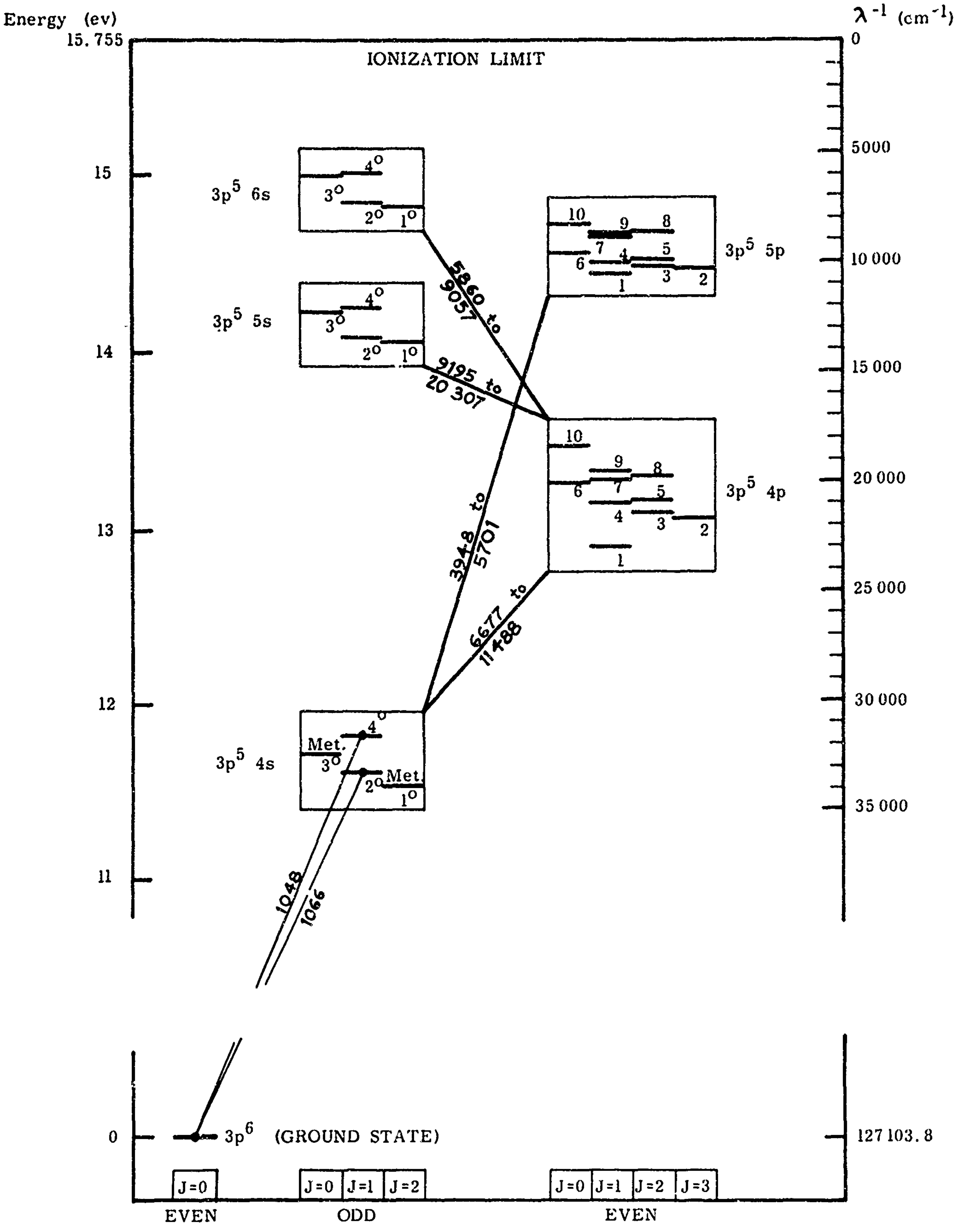

FIG. 5.6 ENERGY LEVEL DIAGRAM FOR NEUTRAL ARGON

UPPER STATES	LOWER STATES			3p⁵ 4s (ODD)			
	ORDER OF LEVELS			Metast. 1^o	2^o	Metast. 3^o	4^o
		TERMS LS	LS	$^3P_2^o$	$^3P_1^o$	$^3P_0^o$	$^1P_1^o$
		LS	jj	$\left(\frac{3}{2}, \frac{1}{2}\right)_2^o$	$\left(\frac{3}{2}, \frac{1}{2}\right)_1^o$	$\left(\frac{1}{2}, \frac{1}{2}\right)_0^o$	$\left(\frac{1}{2}, \frac{1}{2}\right)_1^o$
3p⁵ 4p (EVEN)	1	$^3S_1$	$\left(\frac{3}{2}, \frac{1}{2}\right)_1$	9122.97	9657.78	10470.1	11488.1
	2	$^3D_3$	$\left(\frac{3}{2}, \frac{3}{2}\right)_3$	8115.31	-	-	-
	3	$^3D_2$	$\left(\frac{3}{2}, \frac{3}{2}\right)_2$	8014.79	8424.65	-	9784.50*
	4	$^3D_1$	$\left(\frac{3}{2}, \frac{3}{2}\right)_1$	7723.76	8103.69	8667.94	9354.22*
	5	$^1D_2$	$\left(\frac{3}{2}, \frac{1}{2}\right)_2$	7635.11*	8006.16	-	9224.50
	6	$^3P_0$	$\left(\frac{3}{2}, \frac{3}{2}\right)_0$	-	7514.65*	-	8578.06*
	7	$^1P_1$	$\left(\frac{1}{2}, \frac{1}{2}\right)_1$	7147.04*	7471.18*	7948.18*	8521.44*
	8	$^3P_2$	$\left(\frac{1}{2}, \frac{3}{2}\right)_2$	7067.22*	7383.98*	-	8408.21*
	9	$^3P_1$	$\left(\frac{1}{2}, \frac{3}{2}\right)_1$	6965.43*	7272.94*	7724.21*	8264.52*
	10	$^1S_0$	$\left(\frac{1}{2}, \frac{1}{2}\right)_0$	-	6677.28*	-	7503.87

UPPER STATES	LOWER STATES			3p⁵ 4s (ODD)			
	ORDER OF LEVELS			Metast. 1^o	2^o	Metast. 3^o	4^o
		TERMS LS	LS	$^3P_2^o$	$^3P_1^o$	$^3P_0^o$	$^1P_1^o$
		LS	jj	$\left(\frac{3}{2}, \frac{1}{2}\right)_2^o$	$\left(\frac{3}{2}, \frac{1}{2}\right)_1^o$	$\left(\frac{1}{2}, \frac{1}{2}\right)_0^o$	$\left(\frac{1}{2}, \frac{1}{2}\right)_1^o$
3p⁵ 5p (EVEN)	1	$^3S_1$	$\left(\frac{3}{2}, \frac{1}{2}\right)_1$	4251.19	4363.79	4522.32	5700.86
	2	$^3D_3$	$\left(\frac{3}{2}, \frac{3}{2}\right)_3$	4200.68	-	-	-
	3	$^3D_2$	$\left(\frac{3}{2}, \frac{3}{2}\right)_2$	4190.71	4300.10	-	4628.44
	4	$^3D_1$	$\left(\frac{3}{2}, \frac{3}{2}\right)_1$	4164.18	4272.17	4423.99	4596.10*
	5	$^1D_2$	$\left(\frac{3}{2}, \frac{1}{2}\right)_2$	4158.59*	4266.29*	-	4589.29
	6	$^3P_0$	$\left(\frac{3}{2}, \frac{3}{2}\right)_0$	-	4198.32*	-	4510.73*
	7	$^1P_1$	$\left(\frac{1}{2}, \frac{1}{2}\right)_1$	-	4054.53*	4191.03*	4345.17*
	8	$^3P_2$	$\left(\frac{1}{2}, \frac{3}{2}\right)_2$	3947.50*	4044.42*	-	4333.56*
	9	$^3P_1$	$\left(\frac{1}{2}, \frac{3}{2}\right)_1$	3948.98*	4045.97*	4181.88*	4335.34*
	10	$^1S_0$	$\left(\frac{1}{2}, \frac{1}{2}\right)_0$	-	3979.71*	-	4259.36

* Transitions not allowed under LS-coupling rules

FIG. 5.7 TABLE OF Ar I - LINES FOR TRANSITIONS FROM THE 3p⁵ 4p AND 3p⁵ 5p LEVELS TO THE 3p⁵ 4s LEVELS

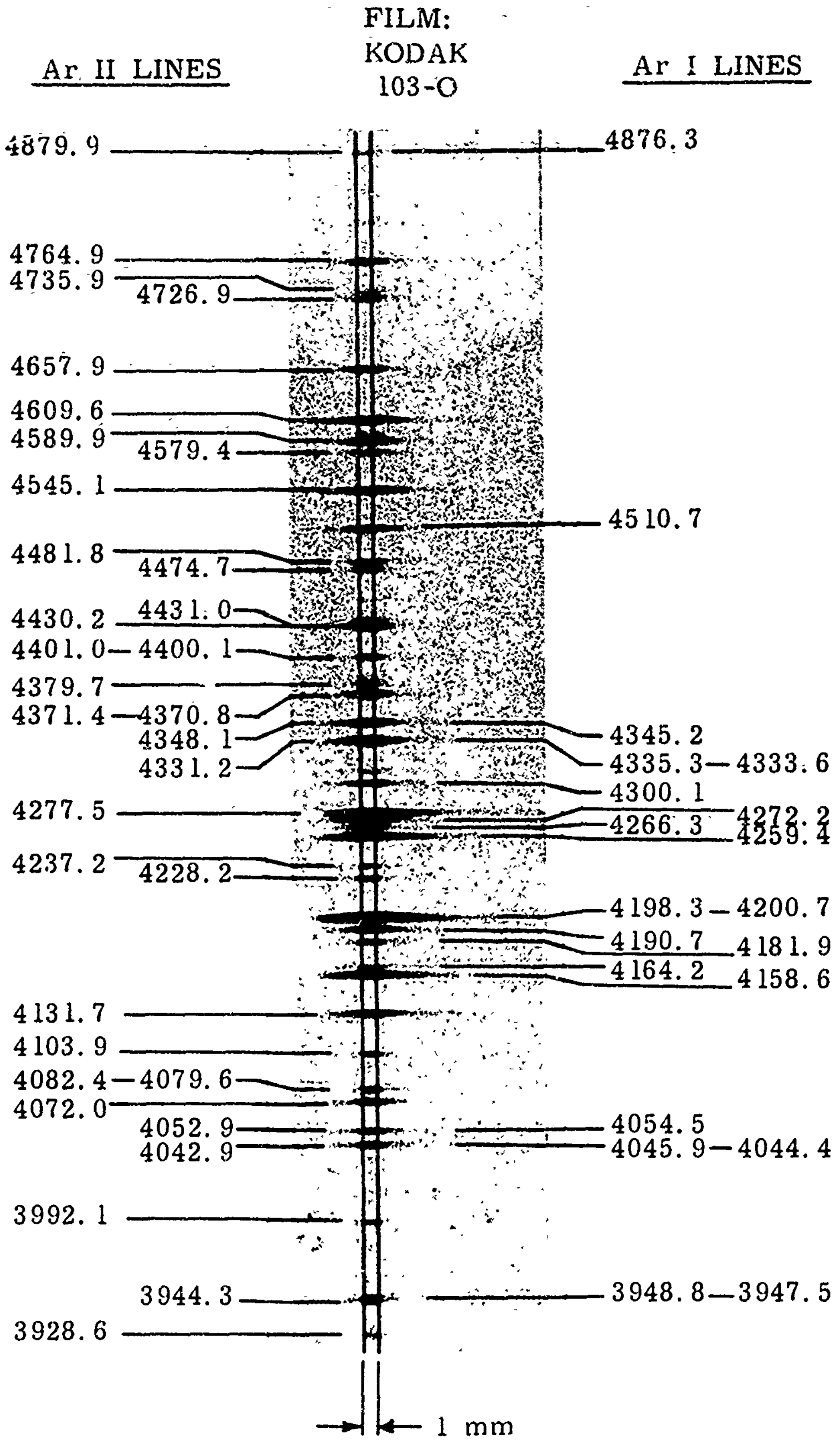

FIG. 5.8 ELECTRON BEAM EXCITED SPECTRUM OF ARGON IN THE SPECTRAL RANGE FROM 3900 Å TO 4900 Å.
THE SPECTROGRAM WAS OBTAINED IN AN UNDEREXPANDED ARGON JET WITH THE 1 mm WIDE ELECTRON BEAM AT RIGHT ANGLES TO THE SPECTROGRAPH SLIT.
THE JET FLOW IS FROM LEFT TO RIGHT

- Spectrogram by D. Marsden, UTIAS -

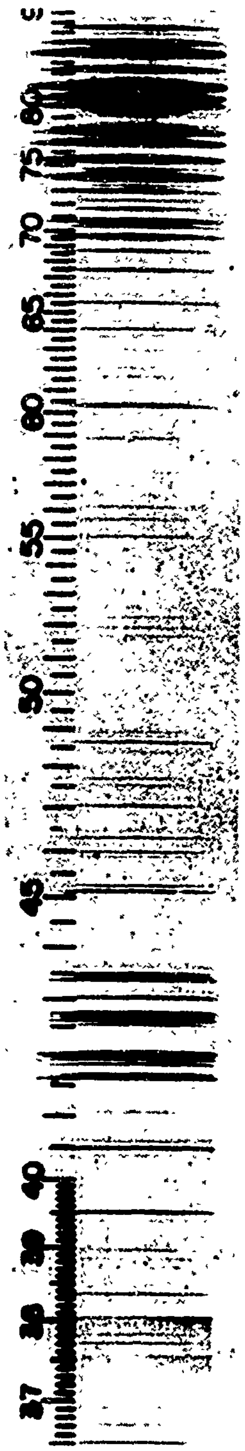

FILM:
KODAK
I-N

FIG. 5.9 A SPECTRUM OF AN ARC HEATED ARGON PLASMA JET
- Spectrogram by D. Marsden, UTIAS -

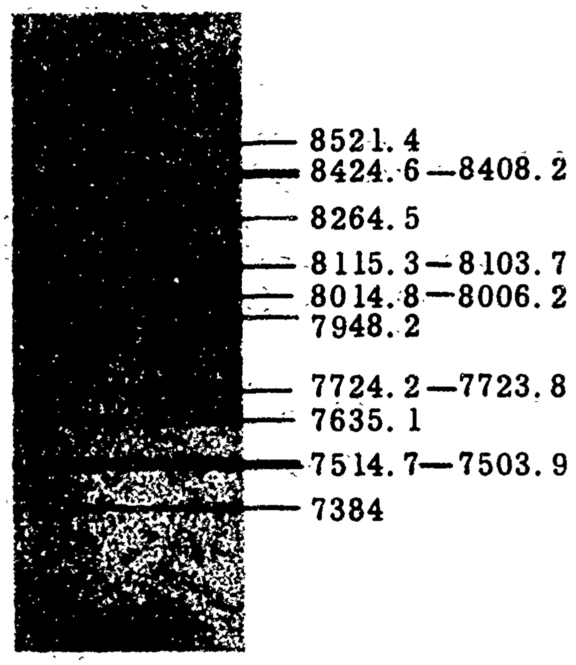

FILM:
KODAK
I-N

FIG. 5.9 B ELECTRON BEAM EXCITED SPECTRUM OF ARGON IN THE FAR RED REGION (ELECTRON BEAM PARALLEL TO SPECTROGRAPH SLIT)

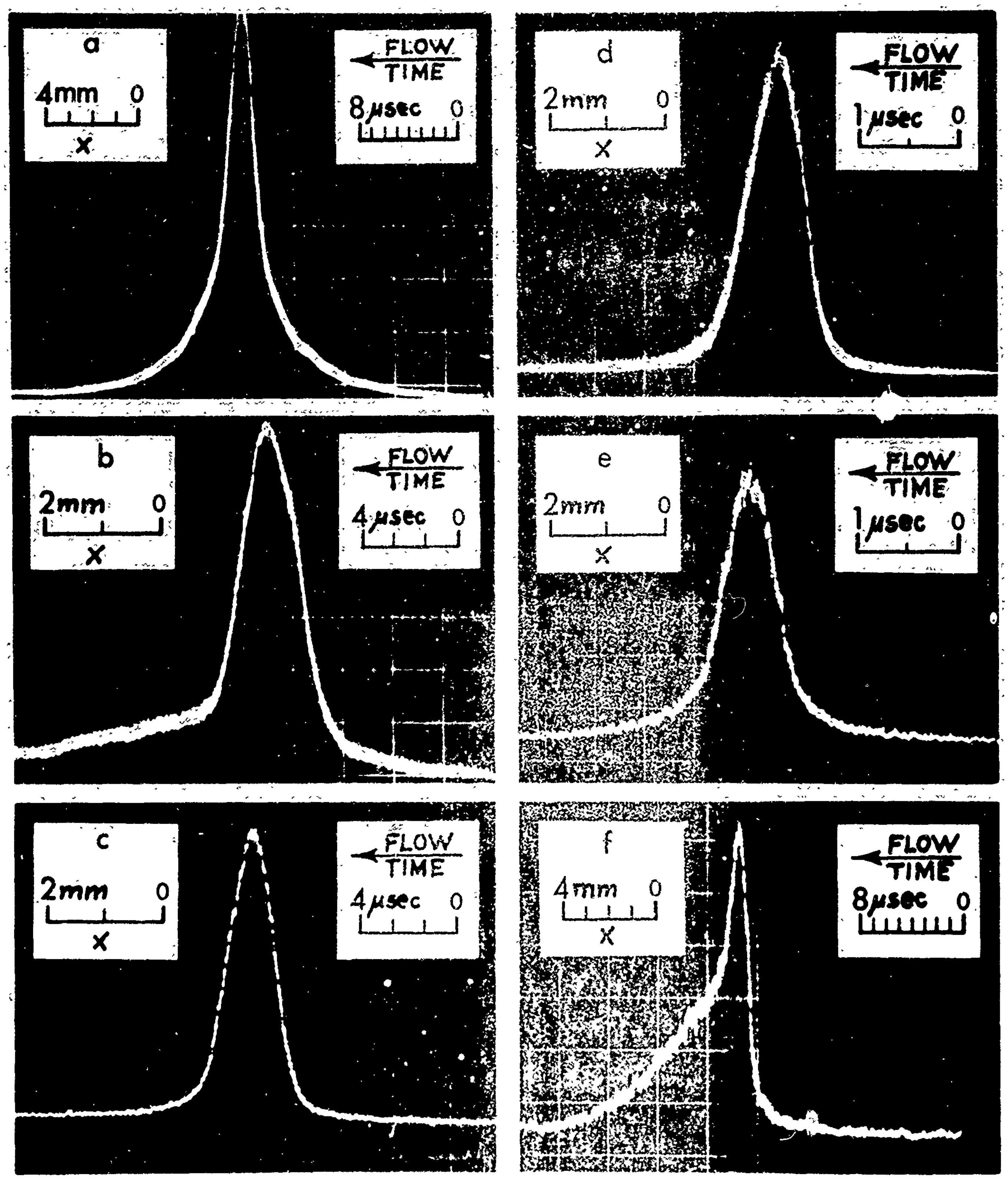

p_o = 25 mm Hg D = 5 mm

Fig.	Gas	Spectral Lines	x/D	M	[illegible]	$(1/n)\partial n/\partial x$ mm^{-1}	u mm/sec
a	Ar I	7200Å-8500Å	2.54	6.52	[illegible]	- 0.17	5.36 X 10^5
b	Ar I	7200Å -8500Å	5.08	9.66	[illegible]	- 0.075	5.50 X 10^5
c	Ar I	7200Å -8500Å	10.16	15.[illegible]	[illegible]	- 0.037	5.56 X 10^5
d	He I	5016Å	5.08	9.66	[illegible]	- 0.075	1.74 X 10^6
e	He I	5016Å	10.16	15.[illegible]	[illegible]	- 0.037	1.76 X 10^6
f	Ar II	5009Å & 5017Å	5.08	9.66	[illegible]	- 0.075	5.50 X10^5

FIG. 5.10 RADIATION PROFILES OF THE ELECTRON BEAM IN ARGON AND HELIUM JETS

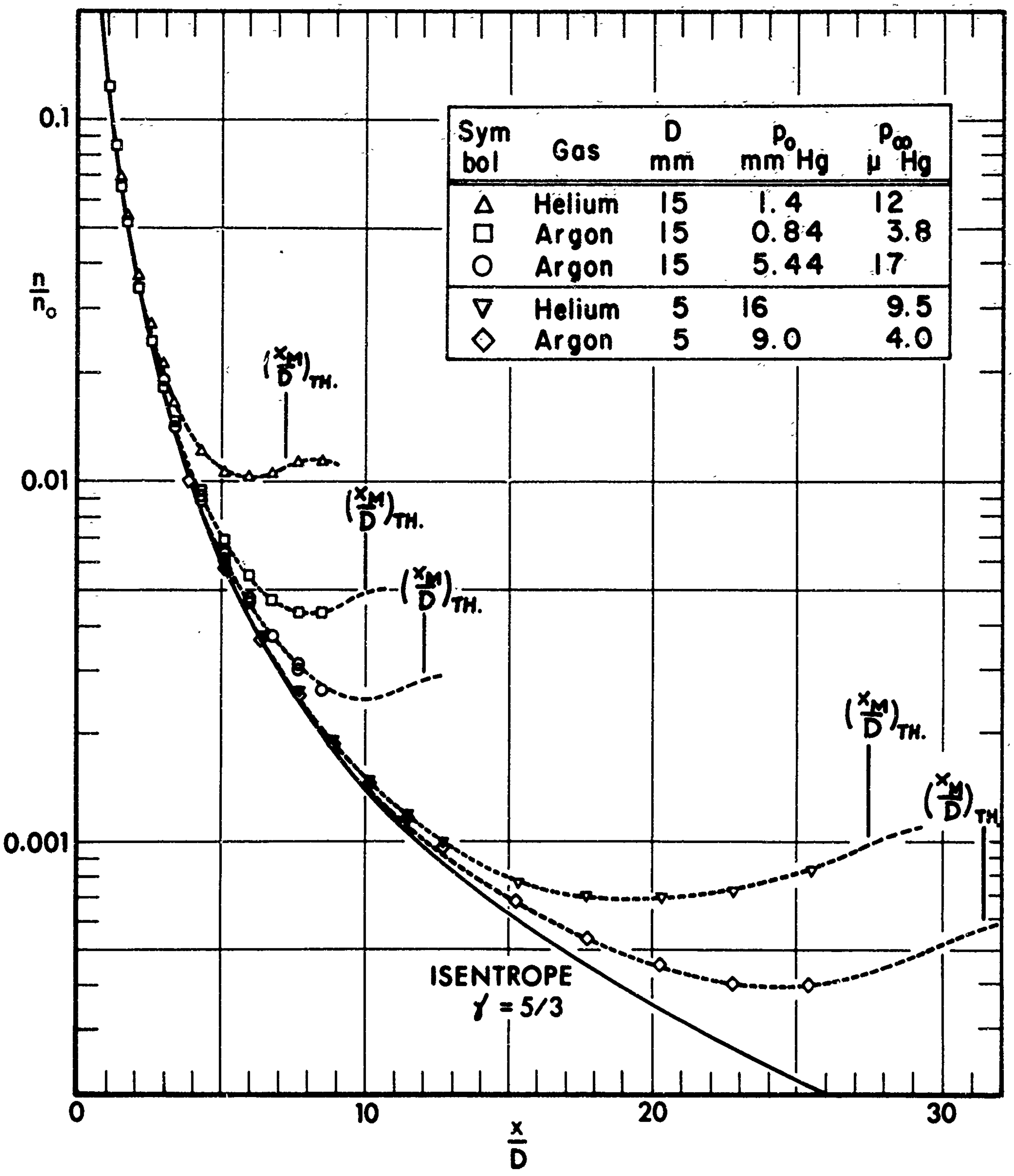

FIG. 5.11 FREE JET DENSITY DATA FOR PURE GASES

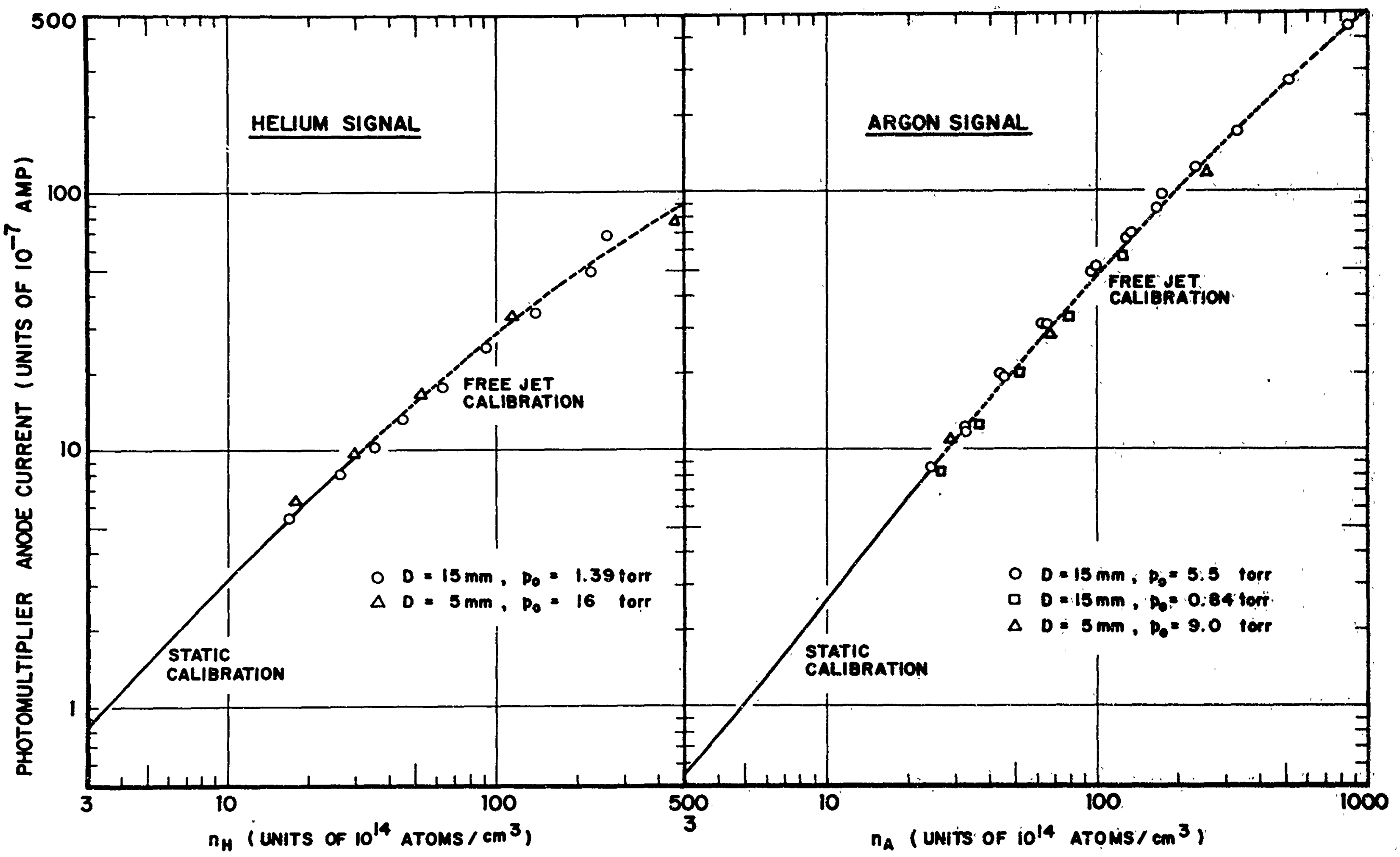

FIG. 5.12 EXTENSION OF CALIBRATION CURVES TO HIGHER DENSITIES

FIG. 5.12 EXTENSION OF CALIBRATION CURVES TO HIGHER DENSITIES

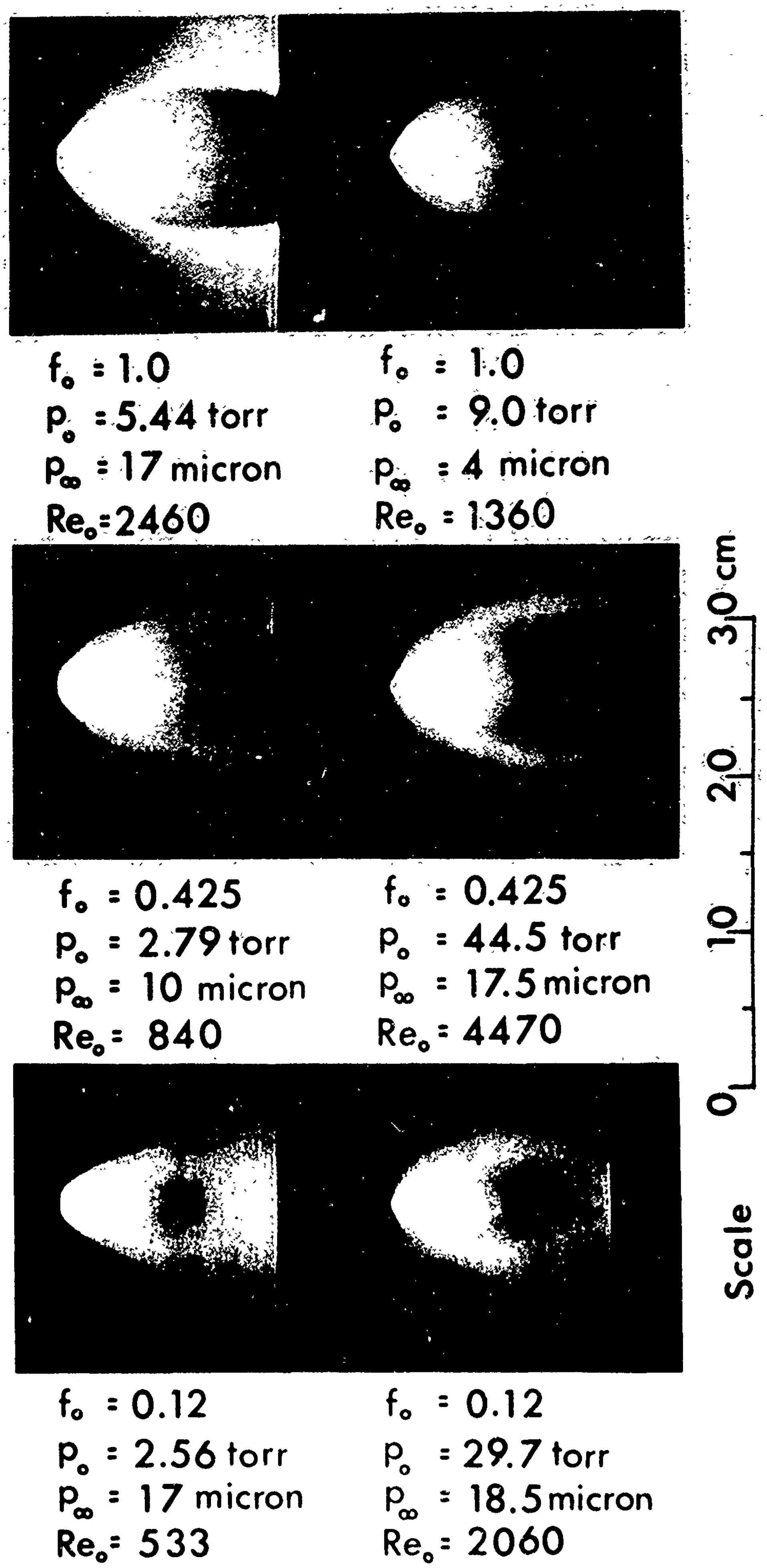

FIG. 5.13 FLOW VISUALIZATION OF SOME OF THE FREE JETS

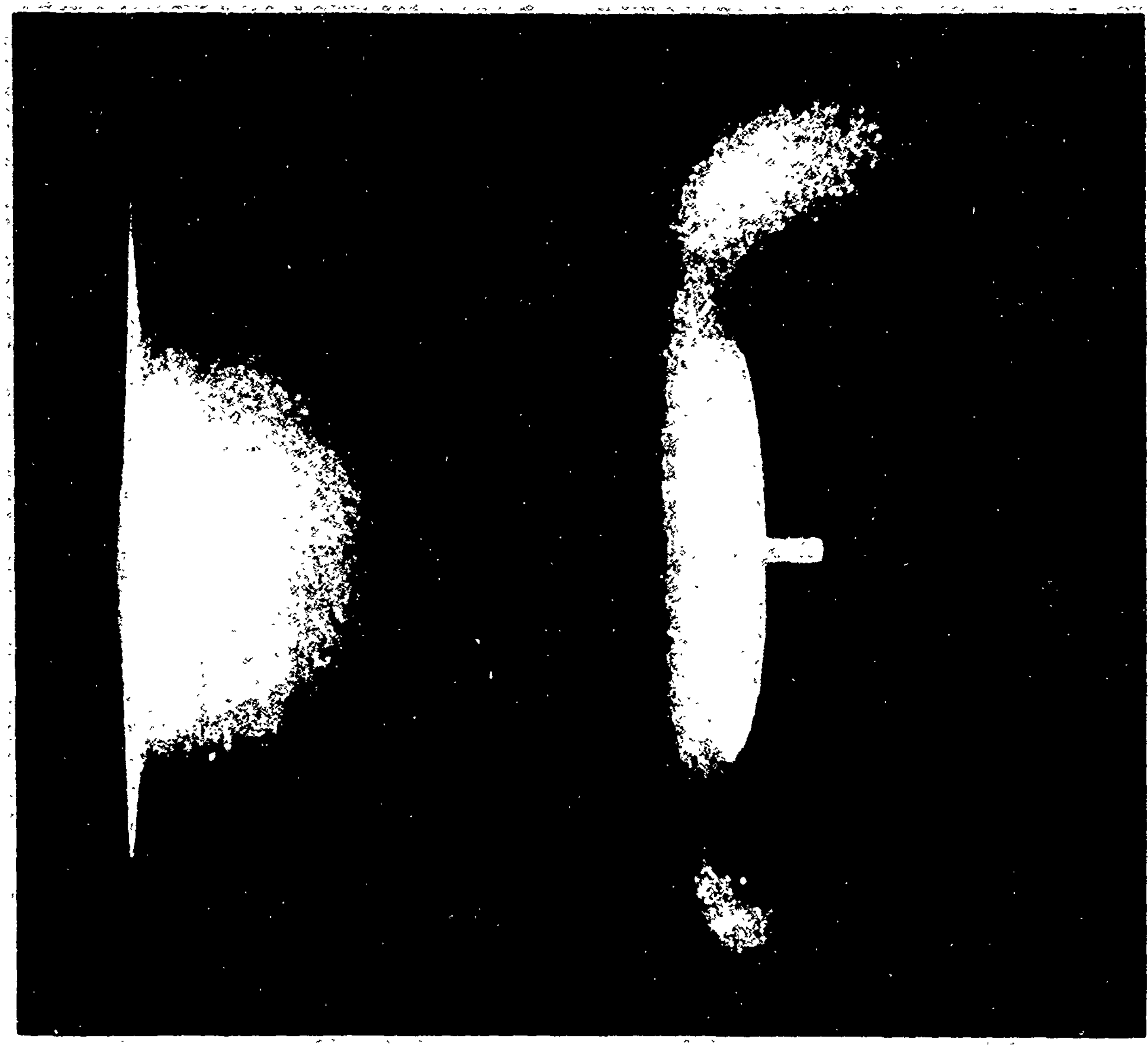

FIG. 5.14 FLOW VISUALIZATION PHOTOGRAPH OF A MACH 4.5 ARGON SHOCK (FLOW IS FROM LEFT TO RIGHT)

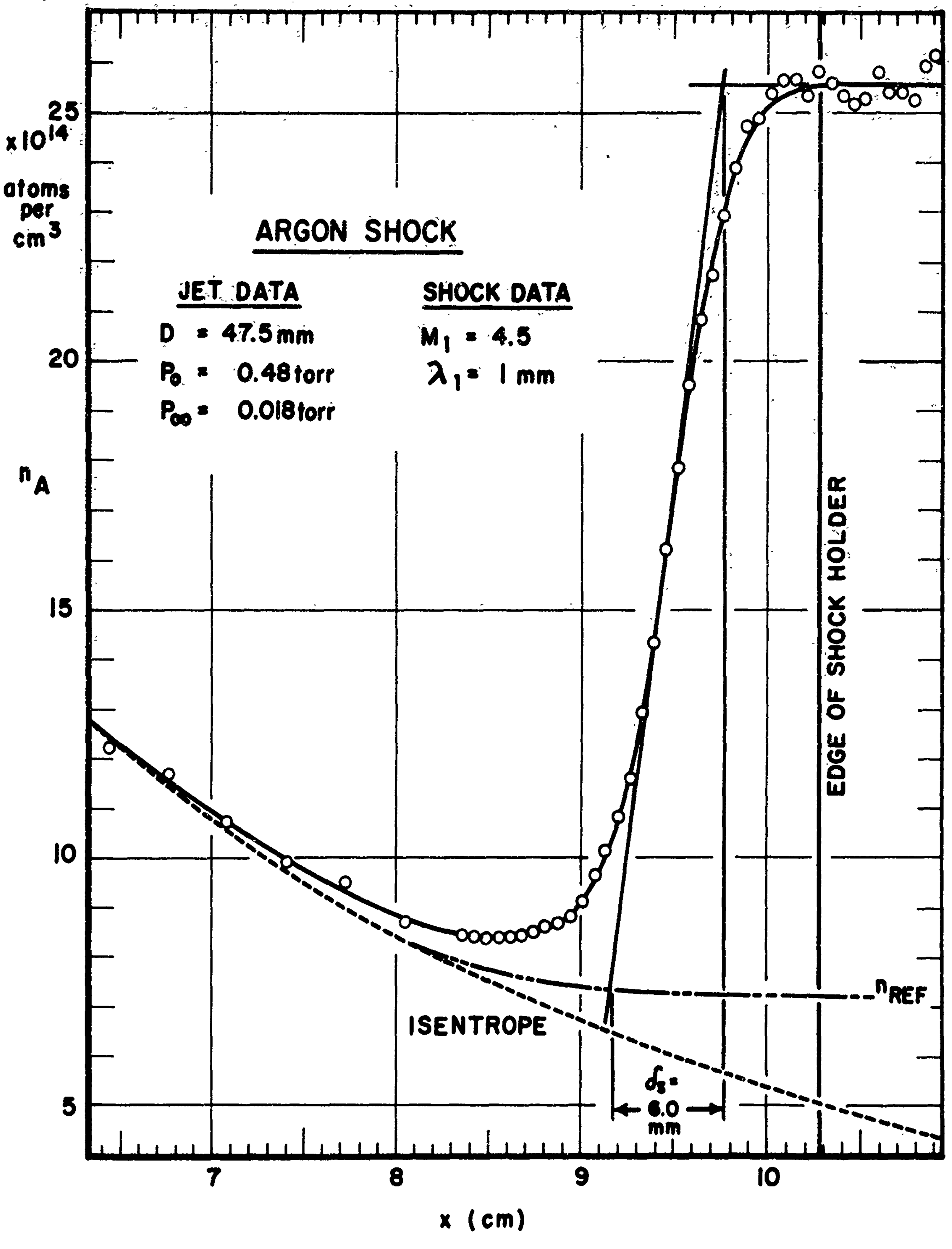

FIG. 5.15 DENSITY PROFILE THROUGH A MACH 4.5 ARGON SHOCK

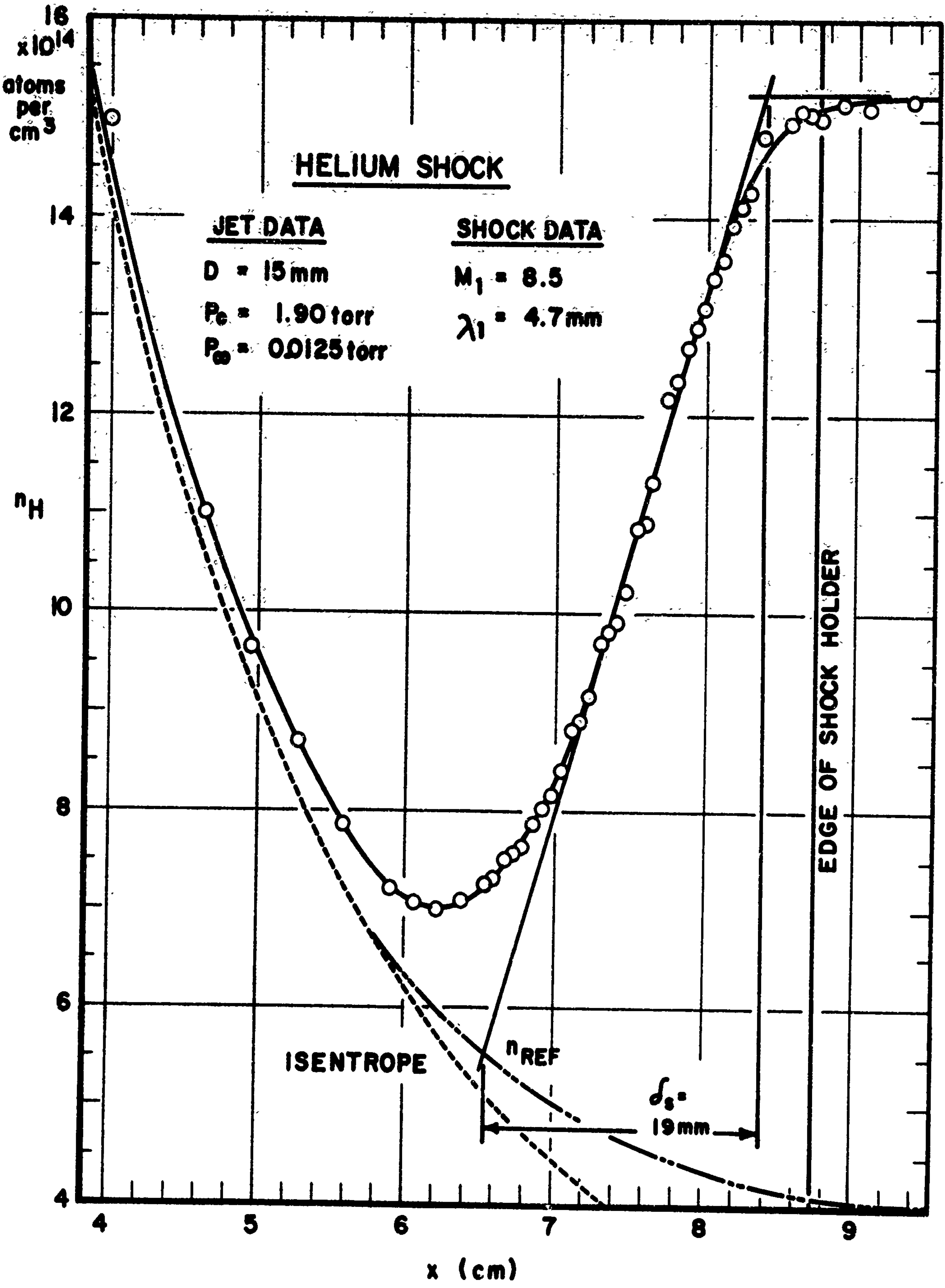

FIG. 5.16 DENSITY PROFILE THROUGH A MACH 8.5 HELIUM SHOCK

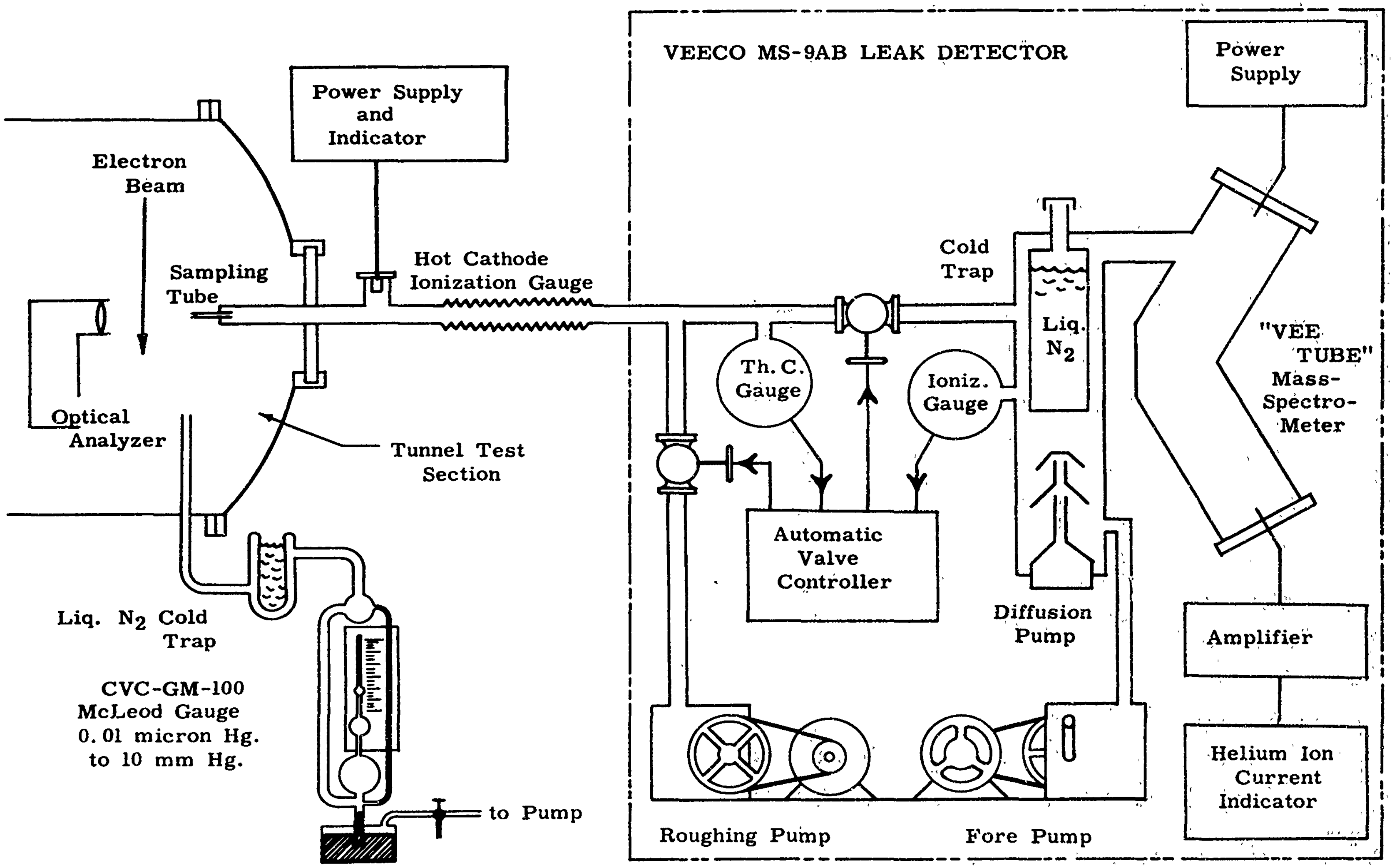

FIG. 5.17A EXPERIMENTAL ARRANGEMENT FOR THE MASS-SPECTROMETER TESTS

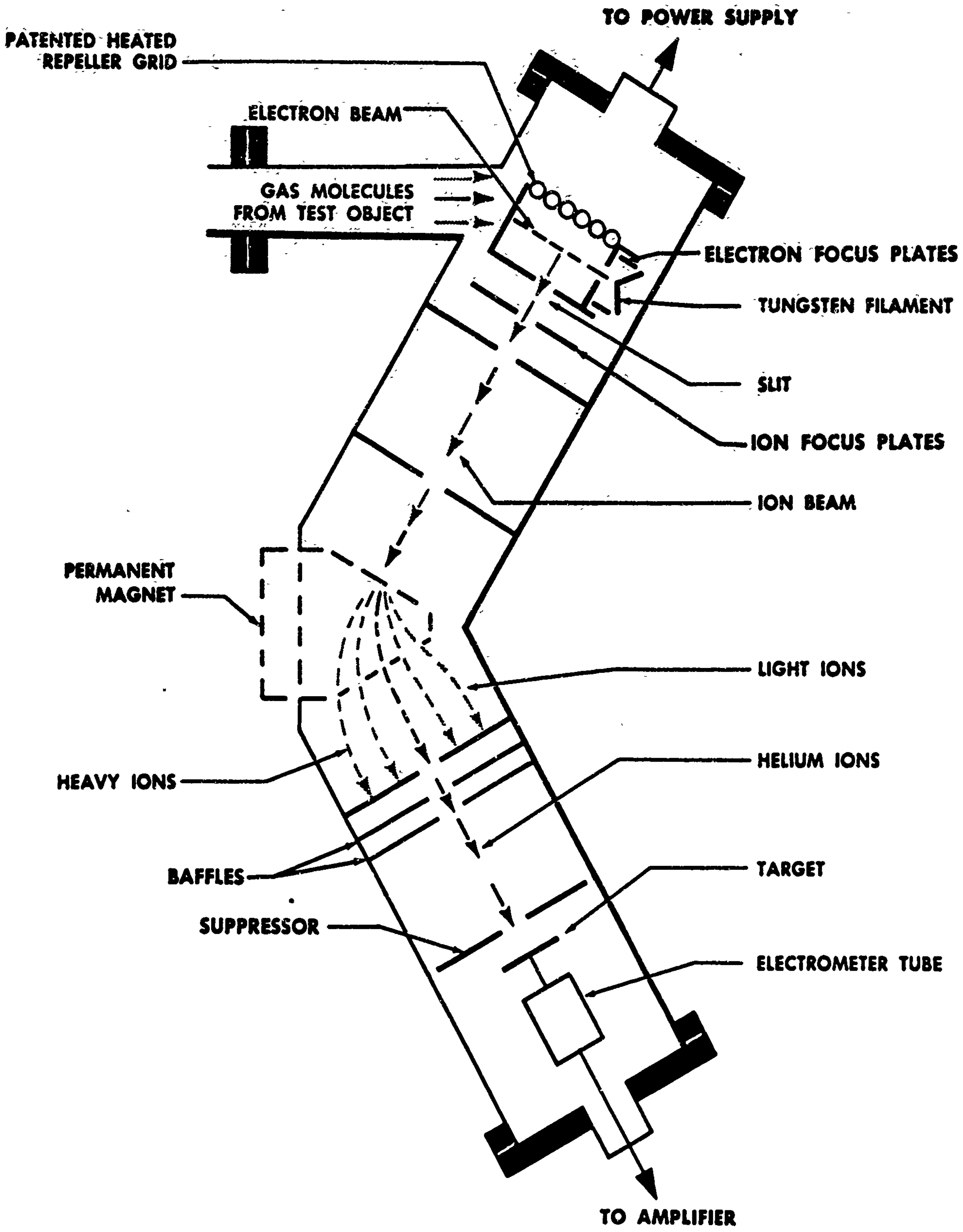

FIG. 5.17B SCHEMATIC OF "VEE TUBE" MASS-SPECTROMETER OF THE VEECO MS-9AB LEAK DETECTOR (Reproduced from VEECO Leak Detector Manual)

LATES

MENT

ATES

TUBE

ER

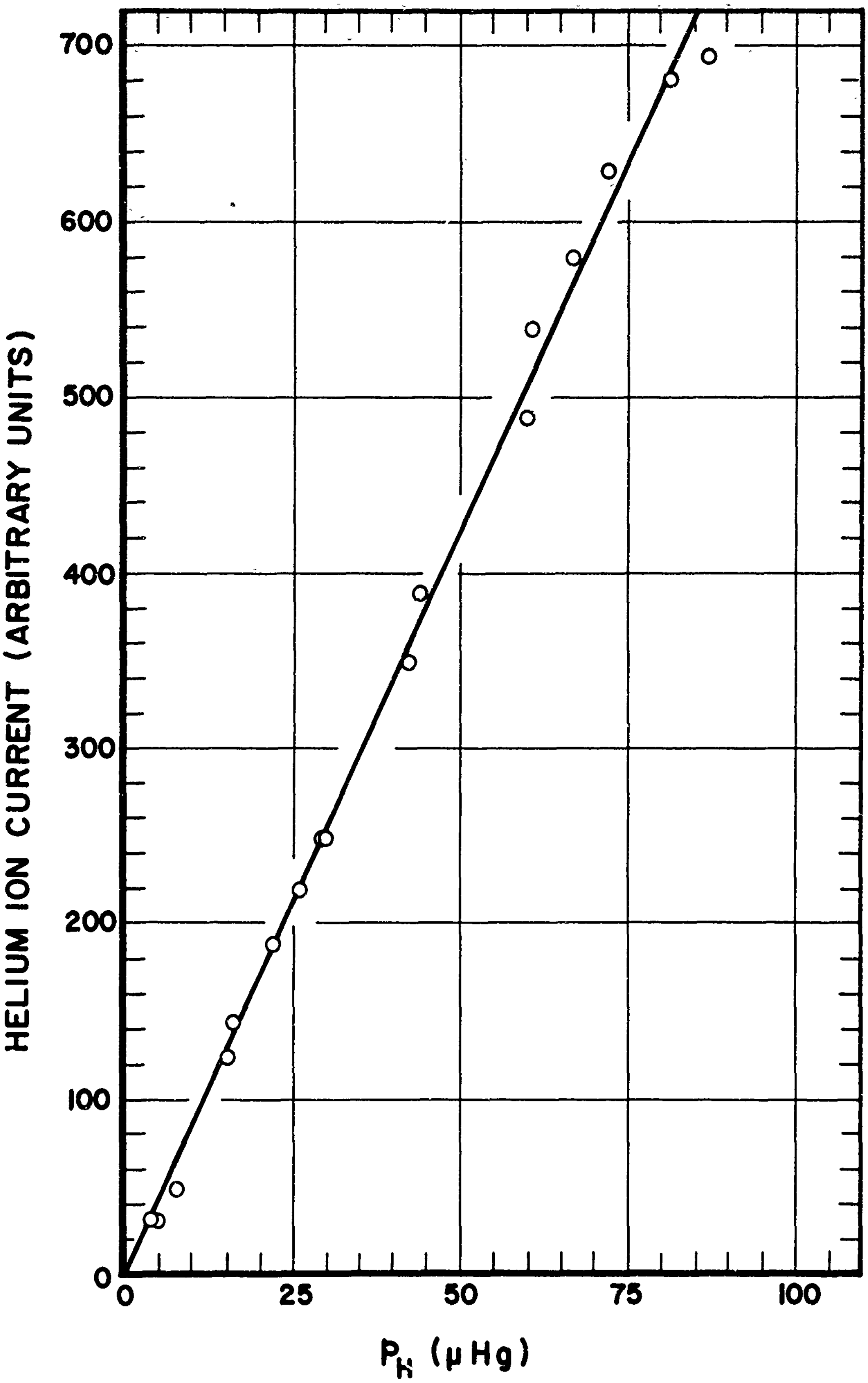

FIG. 5.18 LEAK DETECTOR CALIBRATION CURVE

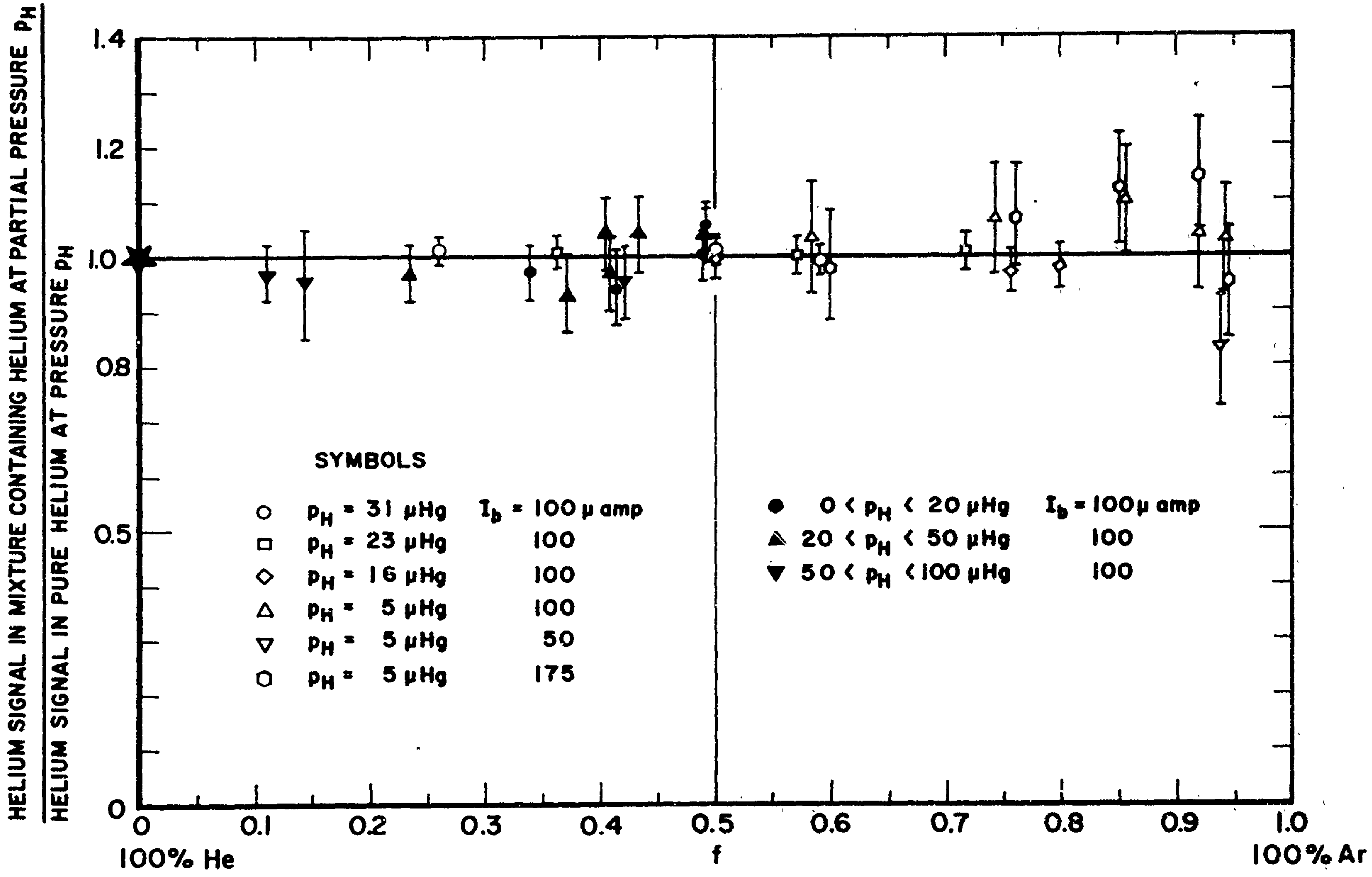

FIG. 5.19 HELIUM SIGNAL IN A HELIUM-ARGON MIXTURE COMPARED WITH THE PURE HELIUM CALIBRATION

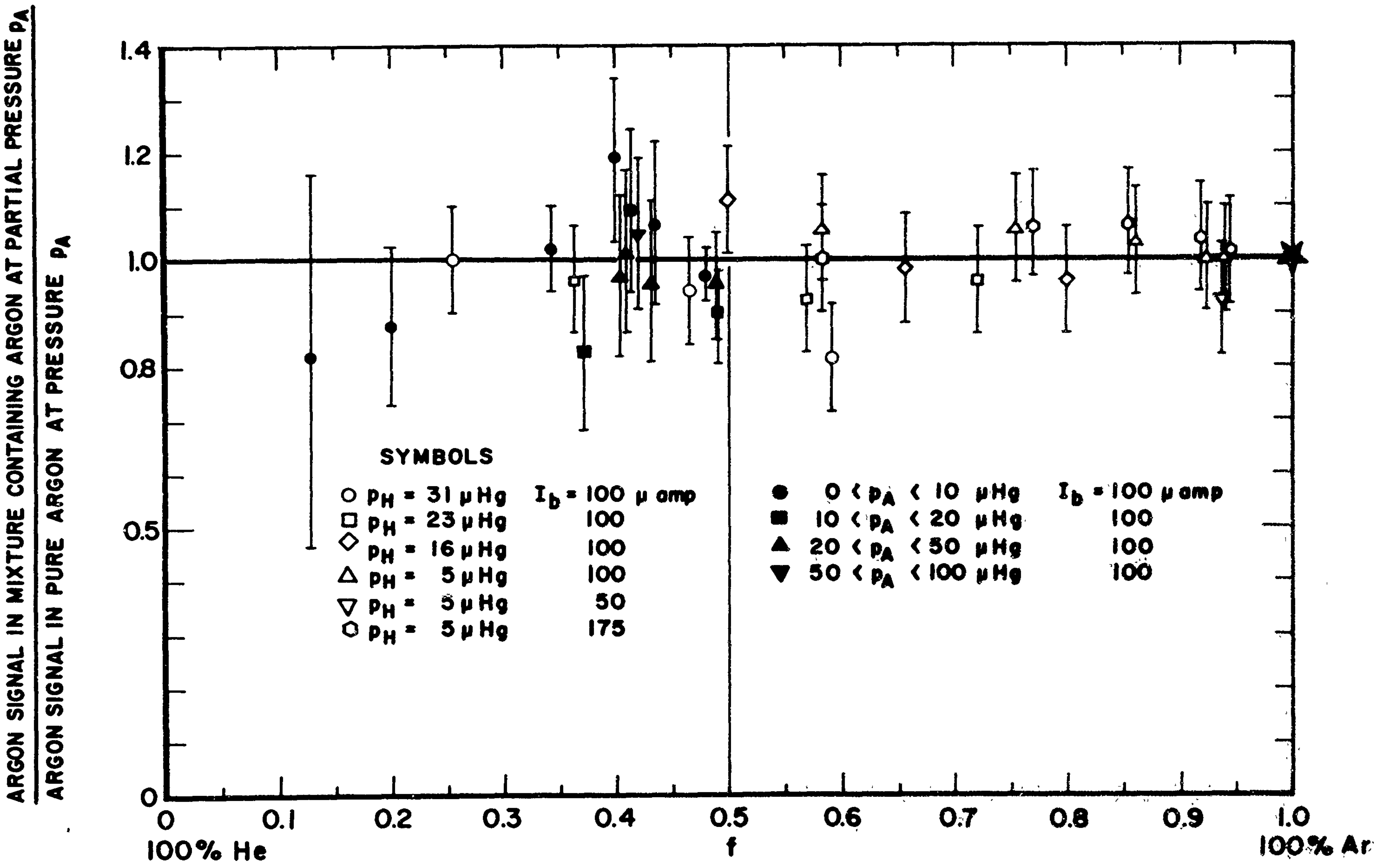

FIG. 5.20 ARGON SIGNAL IN A HELIUM-ARGON MIXTURE COMPARED WITH THE PURE ARGON CALIBRATION

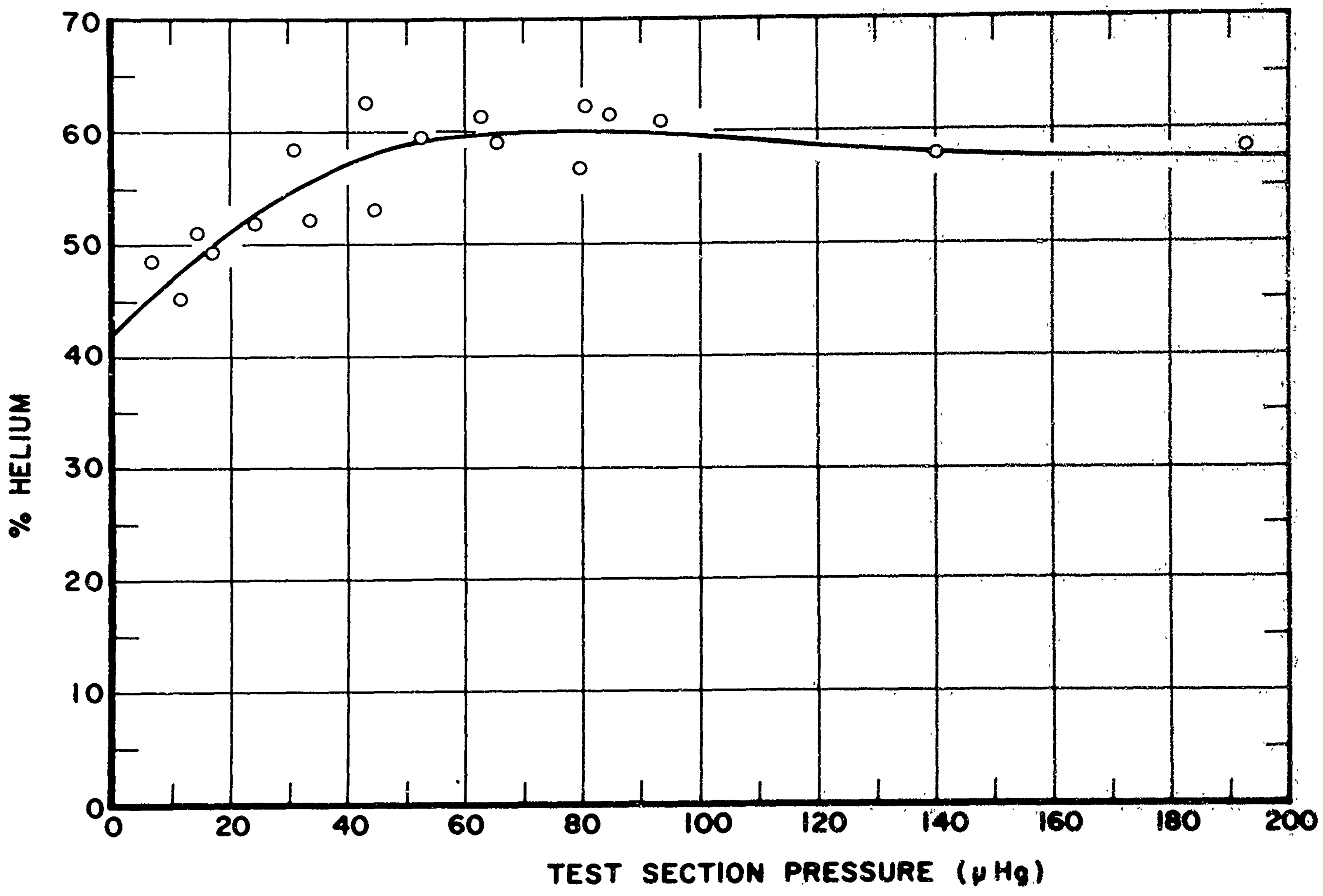

FIG. 5.21 EQUILIBRIUM COMPOSITION IN THE TUNNEL TEST SECTION FOR A 57.5% HELIUM-42.5% ARGON INPUT

COMPOSITION IN THE TUNNEL TEST SECTION FOR A 57.5% HELIUM-42.5% ARGON INPUT

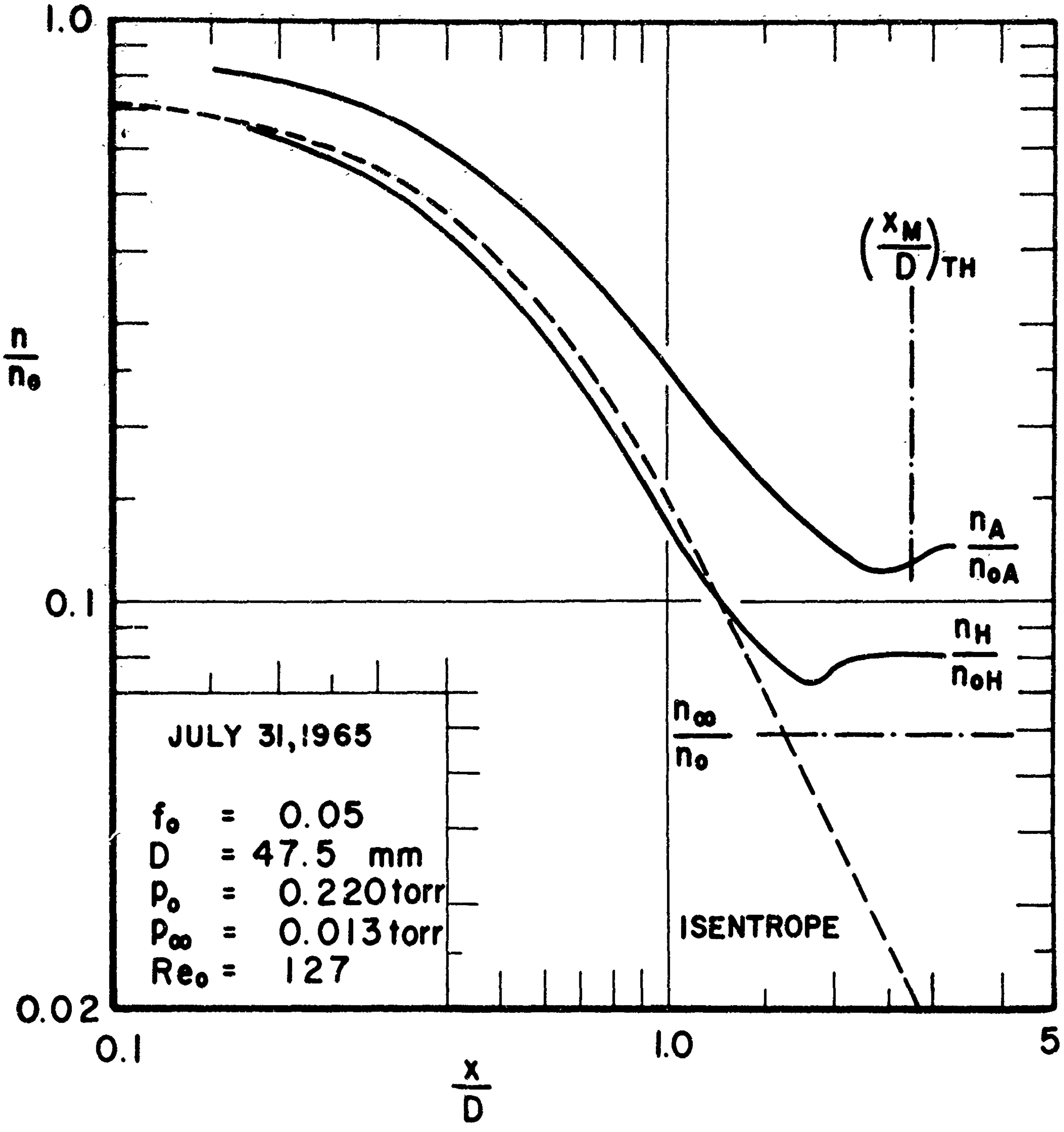

FIG. 7.1 PARTIAL DENSITY PROFILES ALONG THE AXIS OF A FREE JET FOR Re_o = 127 AND f_o = 0.05

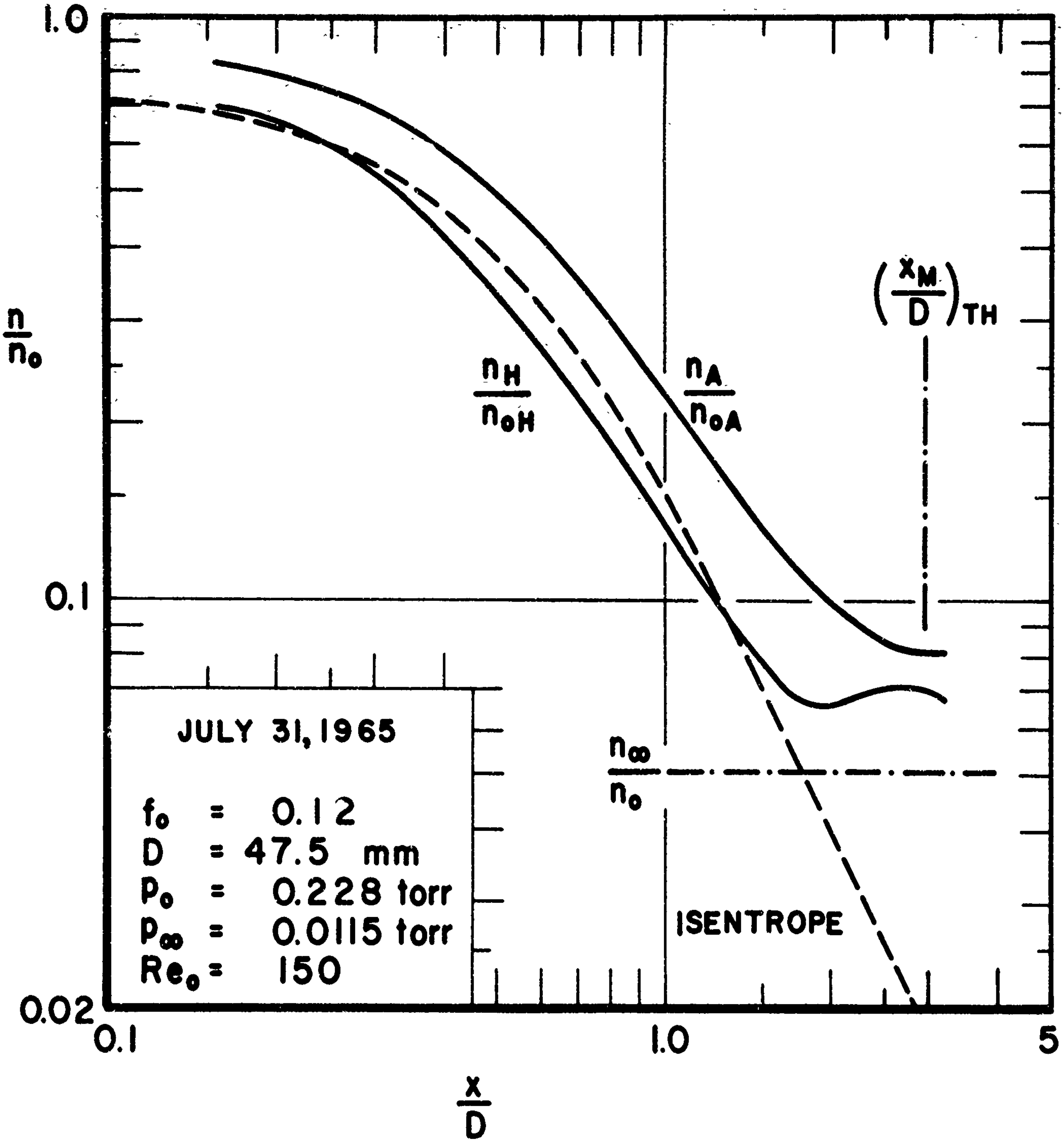

FIG. 7.2 PARTIAL DENSITY PROFILES ALONG THE AXIS OF A FREE JET FOR Re_o = 150 AND f_o = 0.12

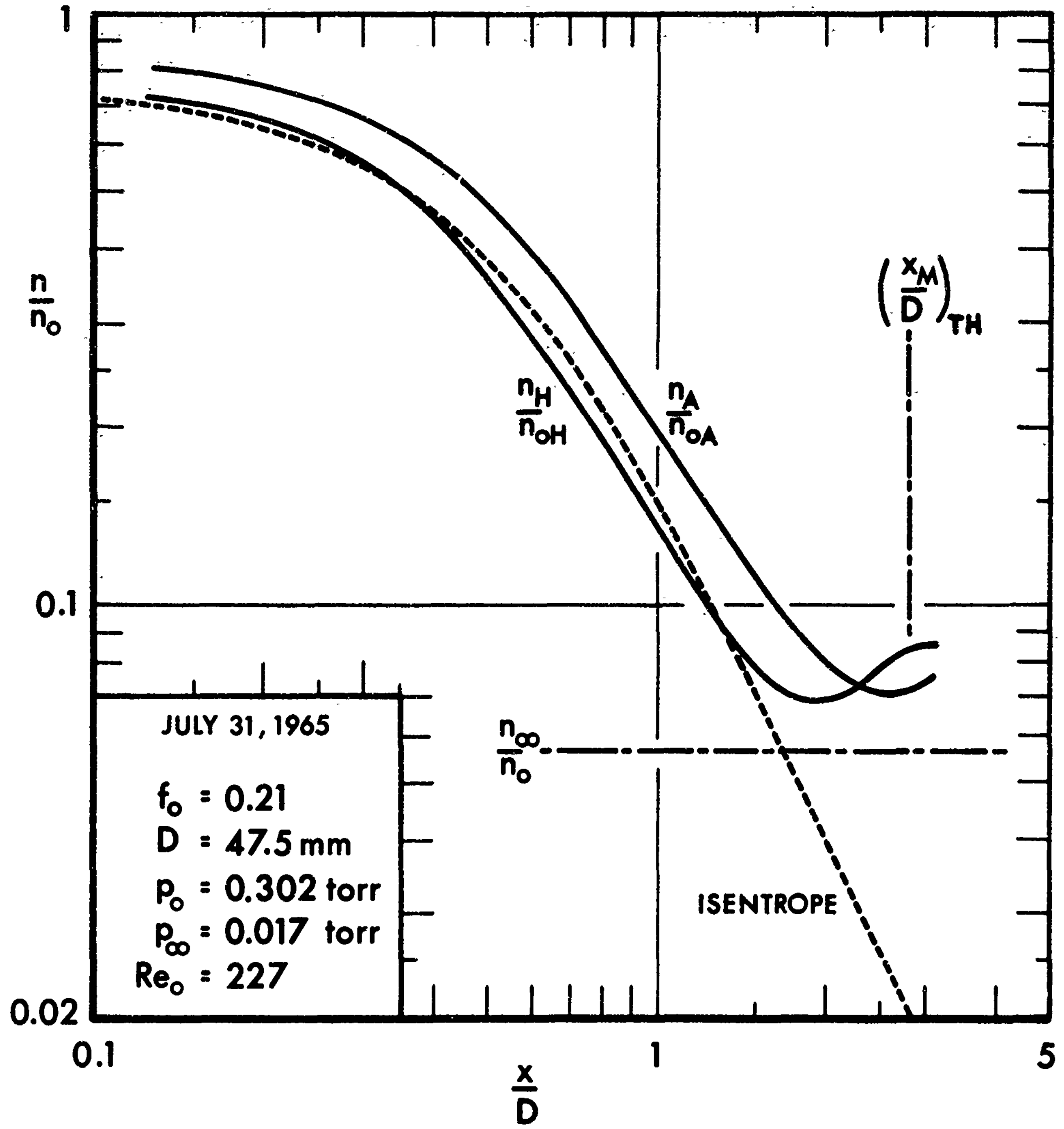

FIG. 7.3 PARTIAL DENSITY PROFILES ALONG THE AXIS OF A FREE JET FOR $Re_o = 227$ AND $f_o = 0.21$

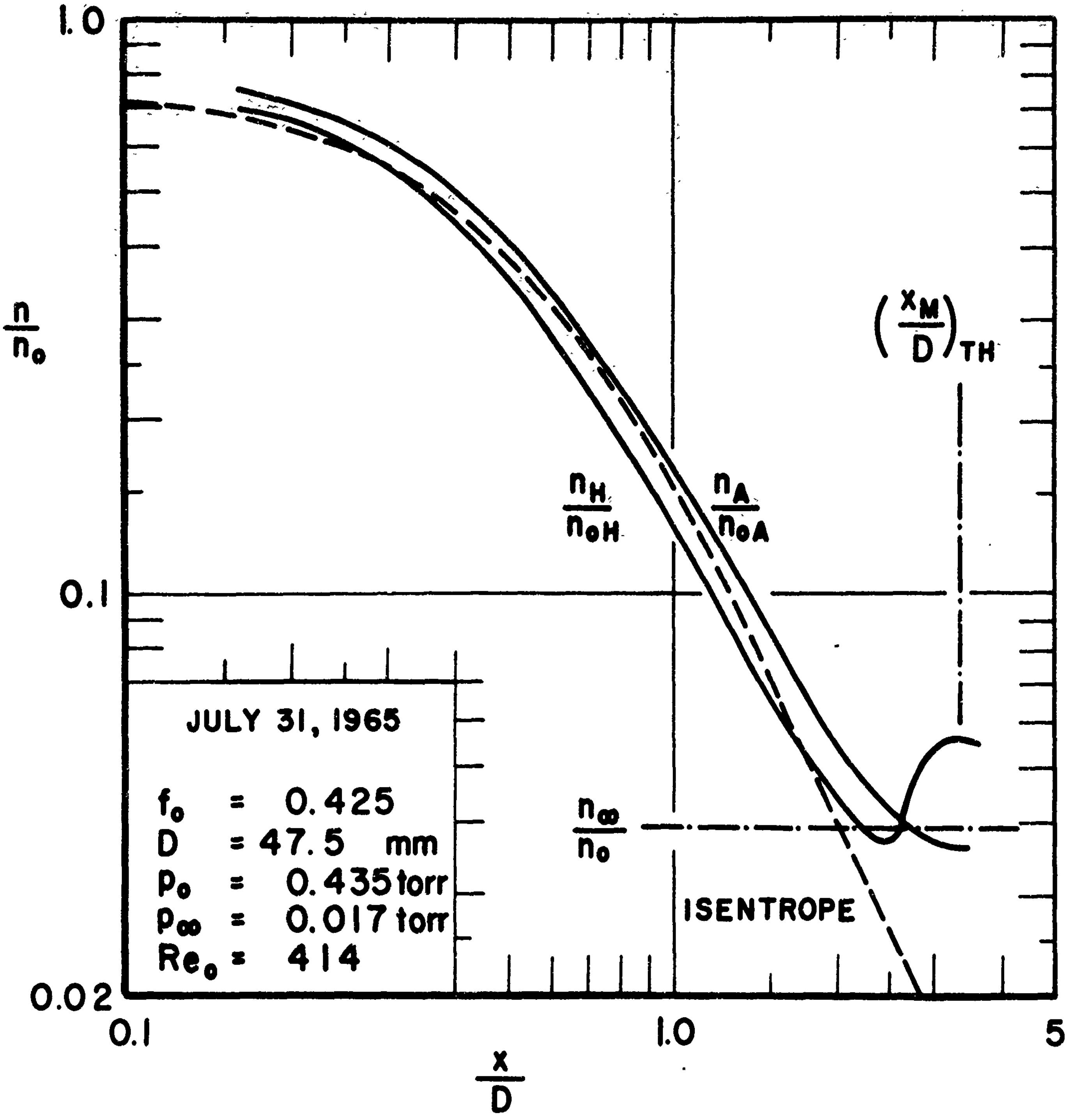

FIG. 7.4 PARTIAL DENSITY PROFILES ALONG THE AXIS OF A FREE JET FOR Re_o = 414 AND f_o = 0.425

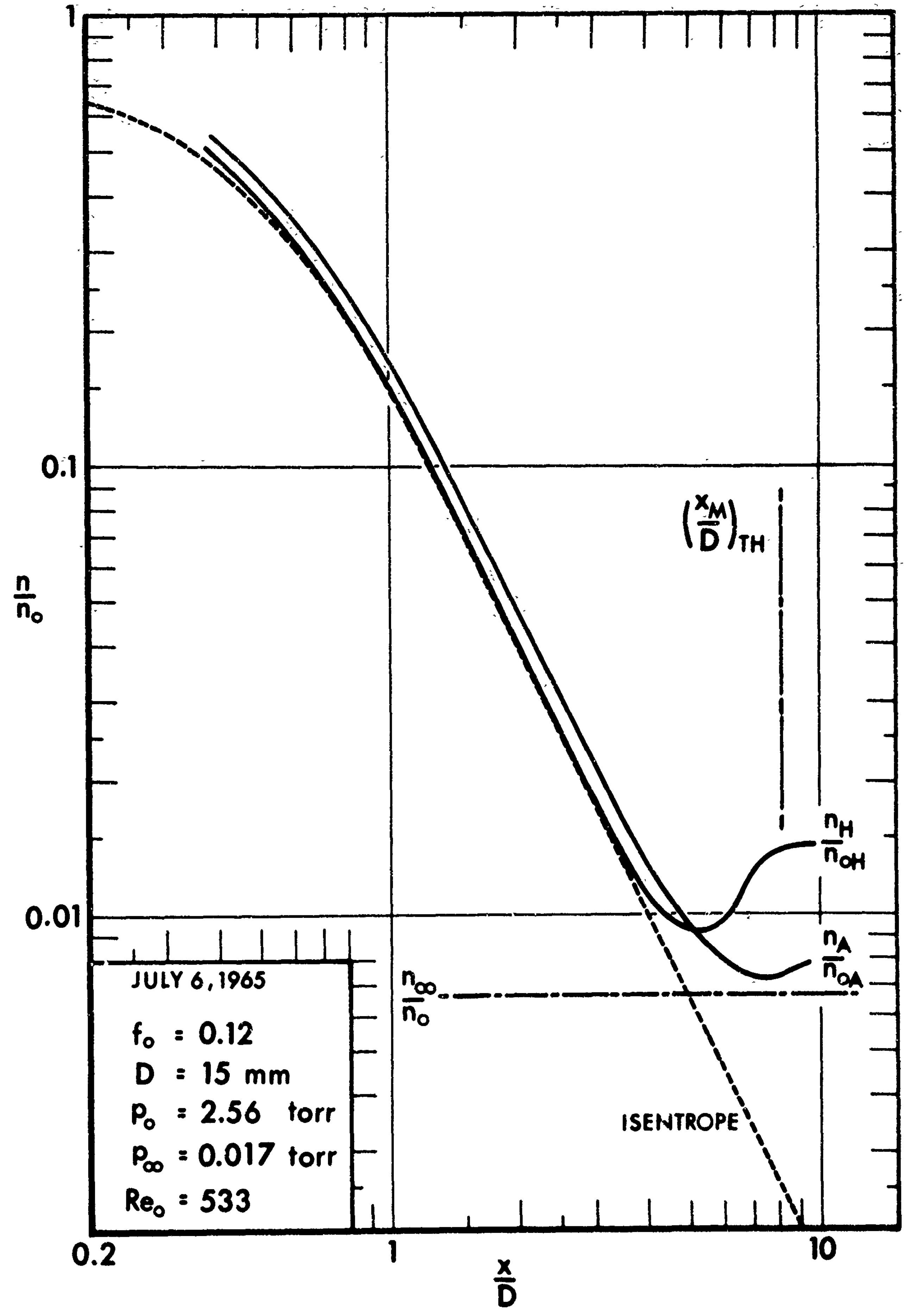

FIG. 7.5 PARTIAL DENSITY PROFILES ALONG THE AXIS OF A FREE JET FOR Re_0 = 533 AND f_0 = 0.12

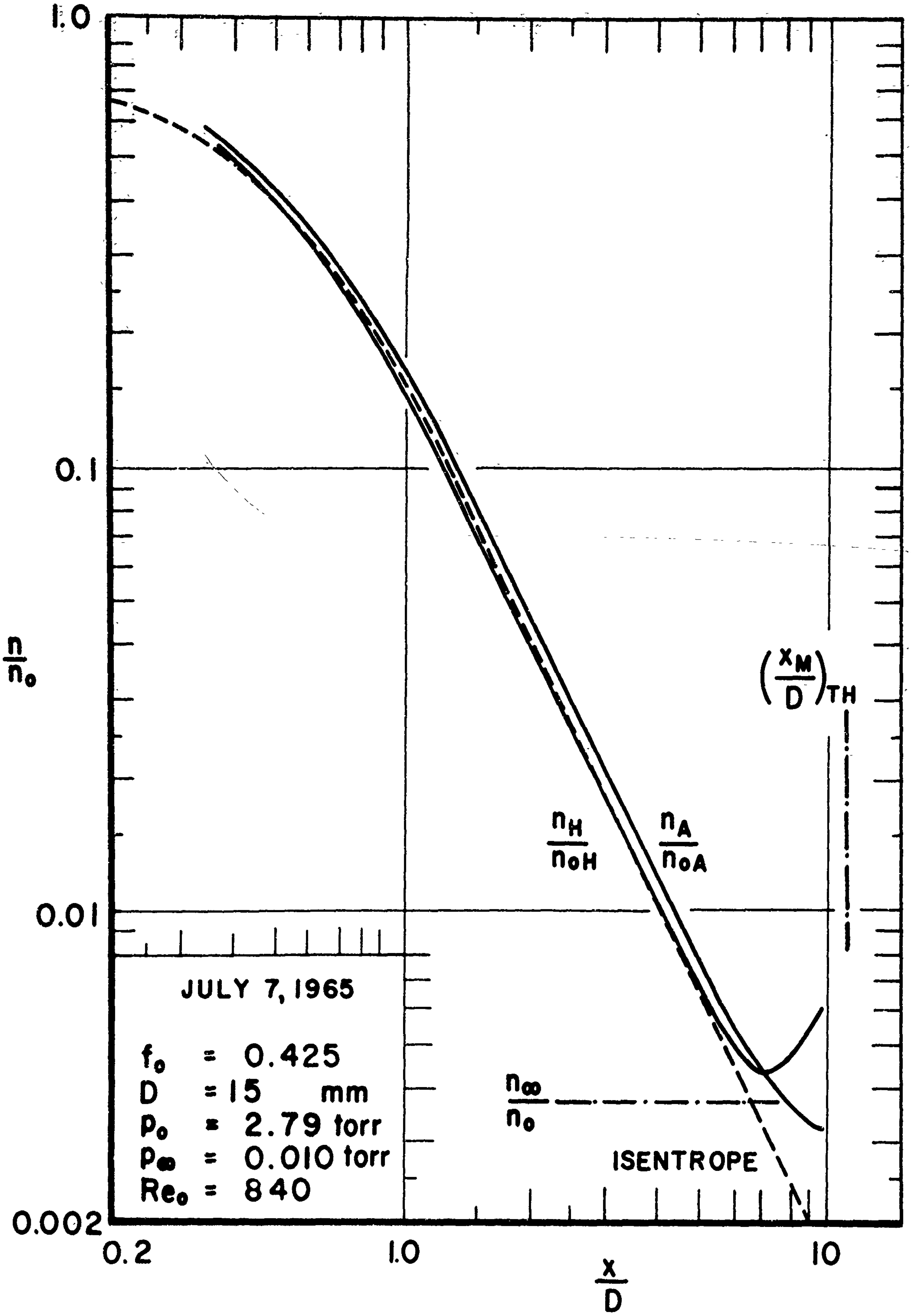

FIG. 7.6 PARTIAL DENSITY PROFILES ALONG THE AXIS OF A FREE JET FOR Re_o = 840 AND f_o = 0.425

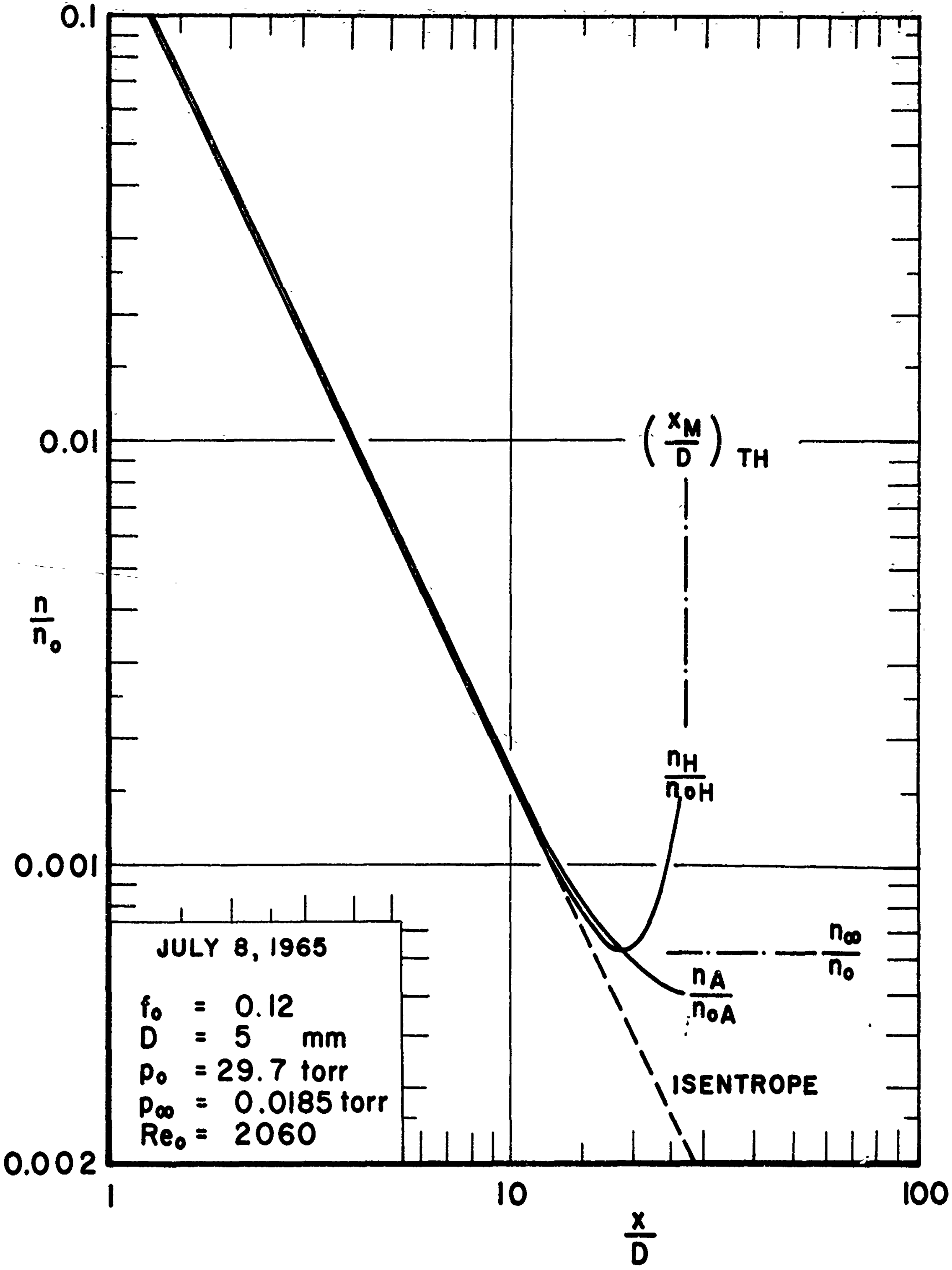

FIG. 7.7 PARTIAL DENSITY PROFILES ALONG THE AXIS OF A FREE JET FOR Re_o = 2060 AND f_o = 0.12

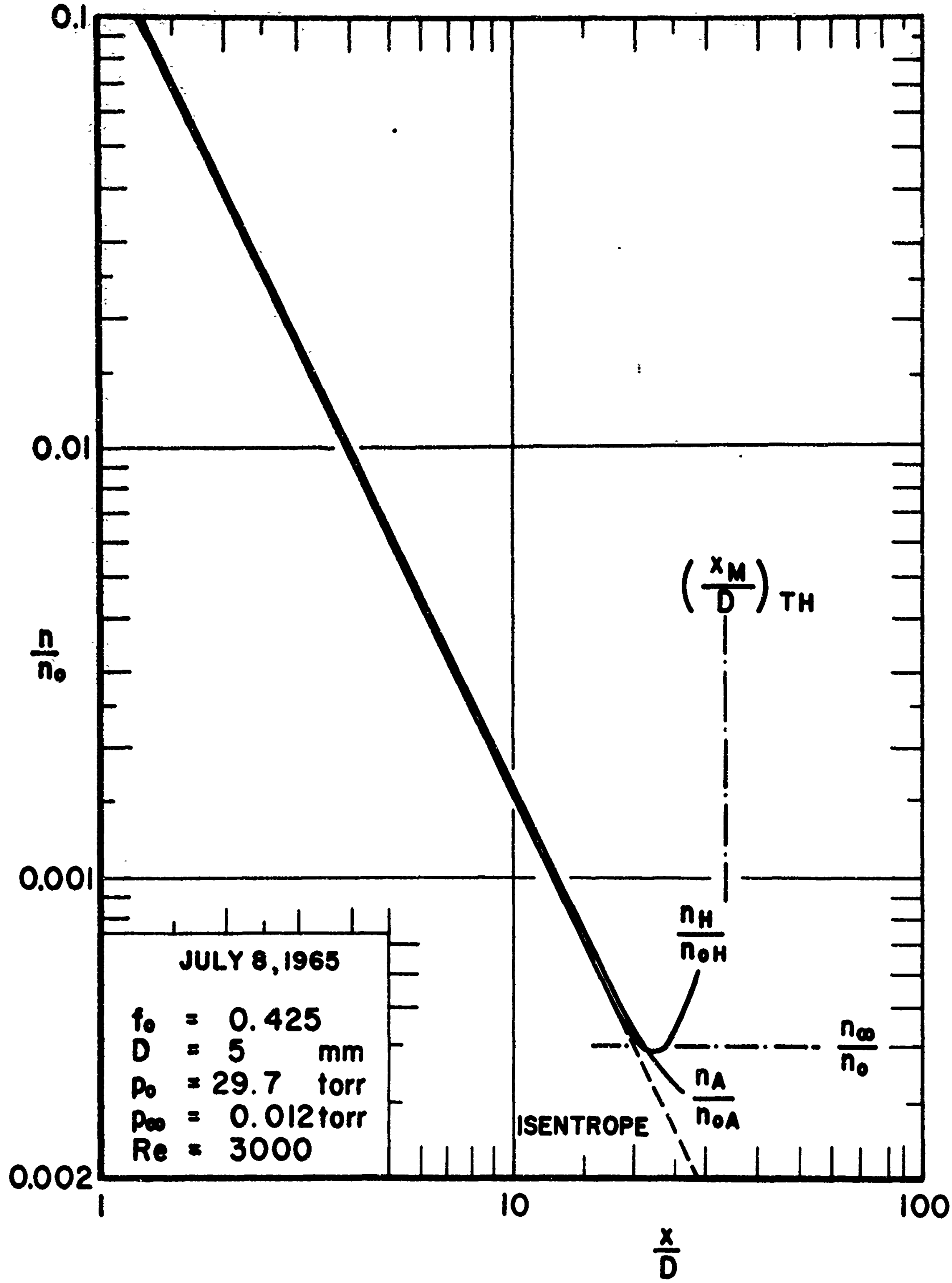

FIG. 7.8 PARTIAL DENSITY PROFILES ALONG THE AXIS OF A FREE JET FOR Re_o = 3000 AND f_o = 0.425

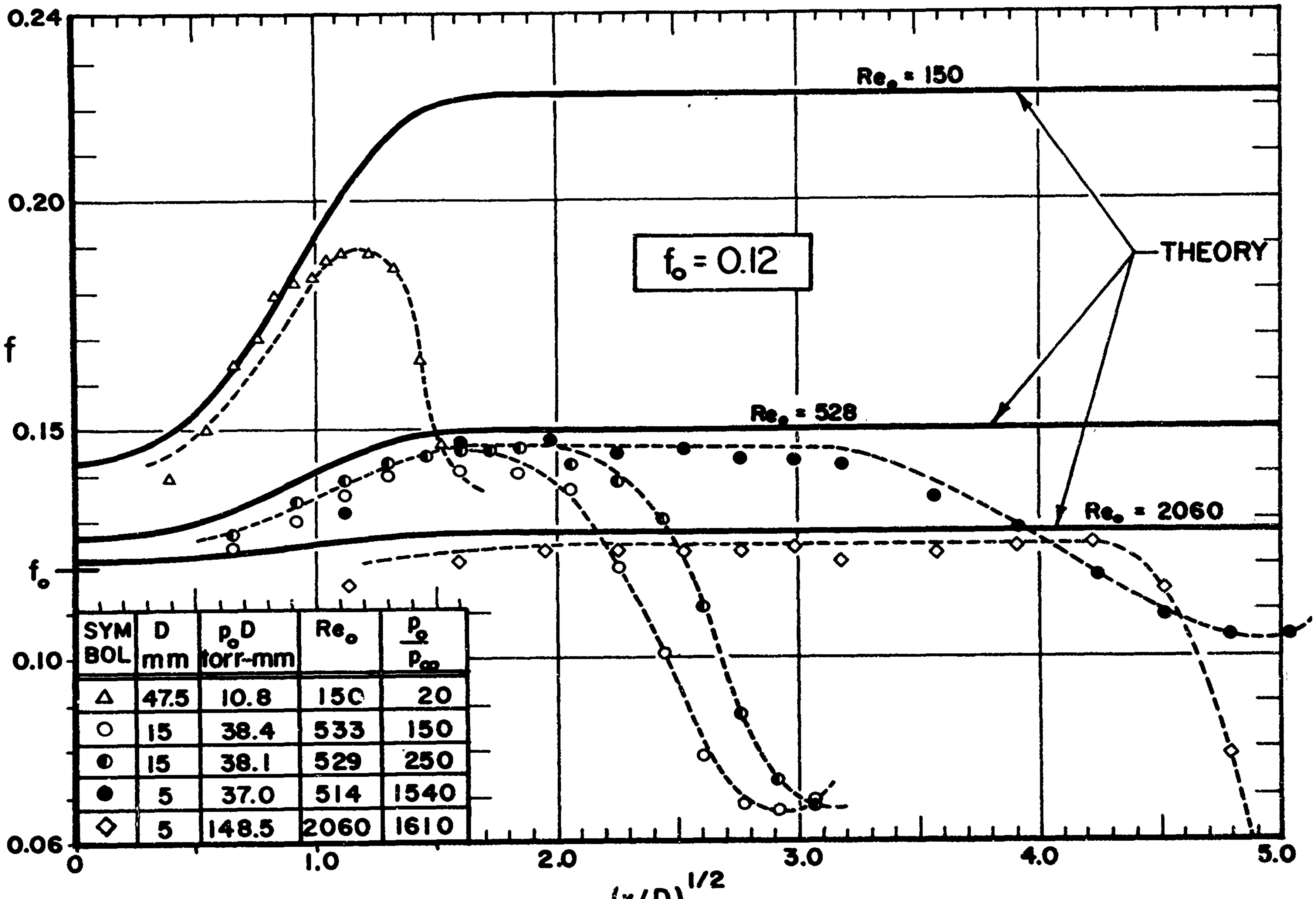

SYM BOL	D mm	p_oD torr-mm	Re_o	$\frac{p_o}{p_\infty}$
△	47.5	10.8	150	20
○	15	38.4	533	150
◐	15	38.1	529	250
●	5	37.0	514	1540
◇	5	148.5	2060	1610

FIG. 7.9 MOLE FRACTION OF ARGON ALONG THE AXES OF VARIOUS FREE JETS (f_o = 0.12)

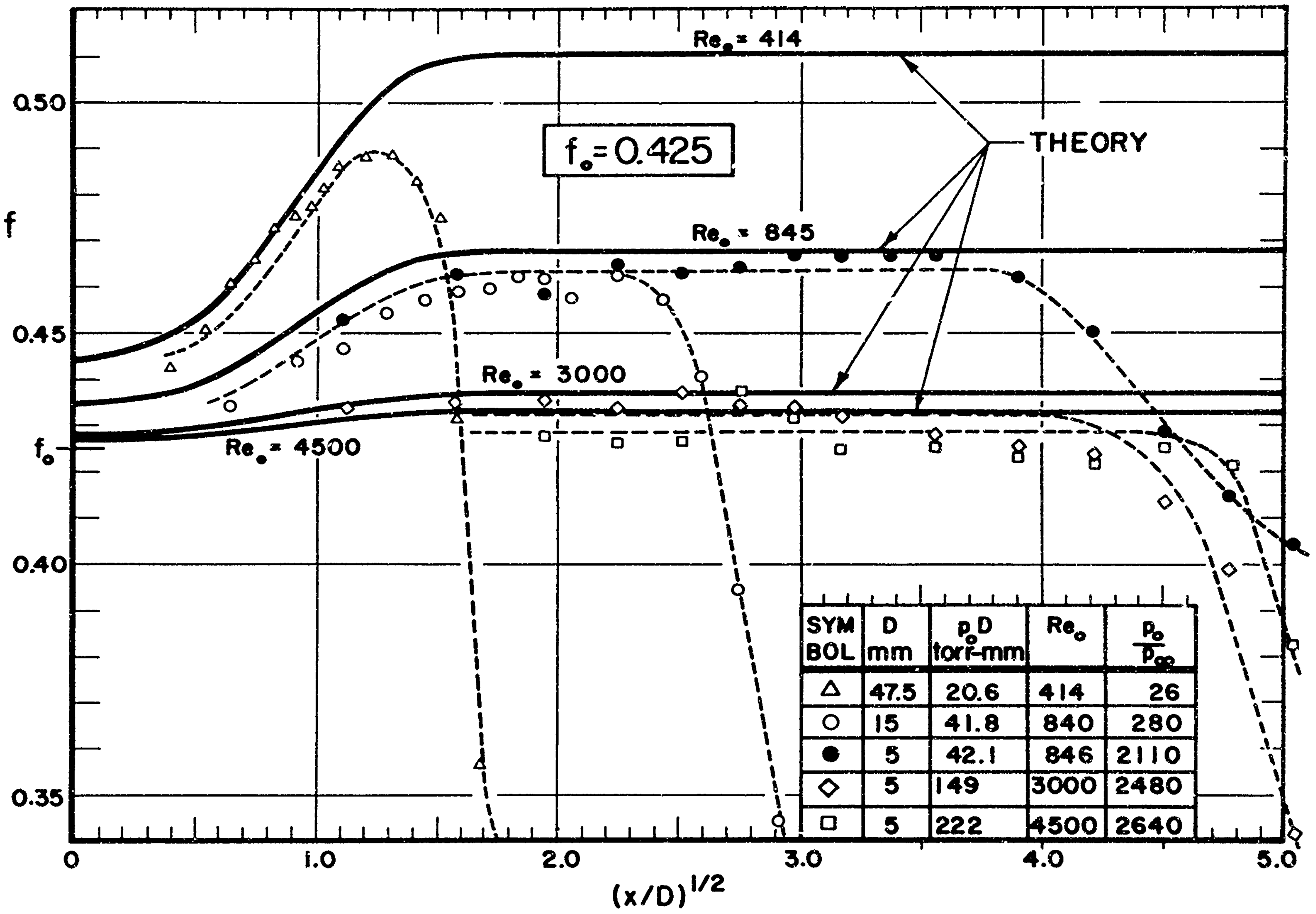

SYM BOL	D mm	p_oD torr-mm	Re$_o$	$\frac{p_o}{p_\infty}$
△	47.5	20.6	414	26
○	15	41.8	840	280
●	5	42.1	846	2110
◇	5	149	3000	2480
□	5	222	4500	2640

FIG. 7.10 MOLE FRACTION OF ARGON ALONG THE AXES OF VARIOUS FREE JETS (f_o = 0.425)

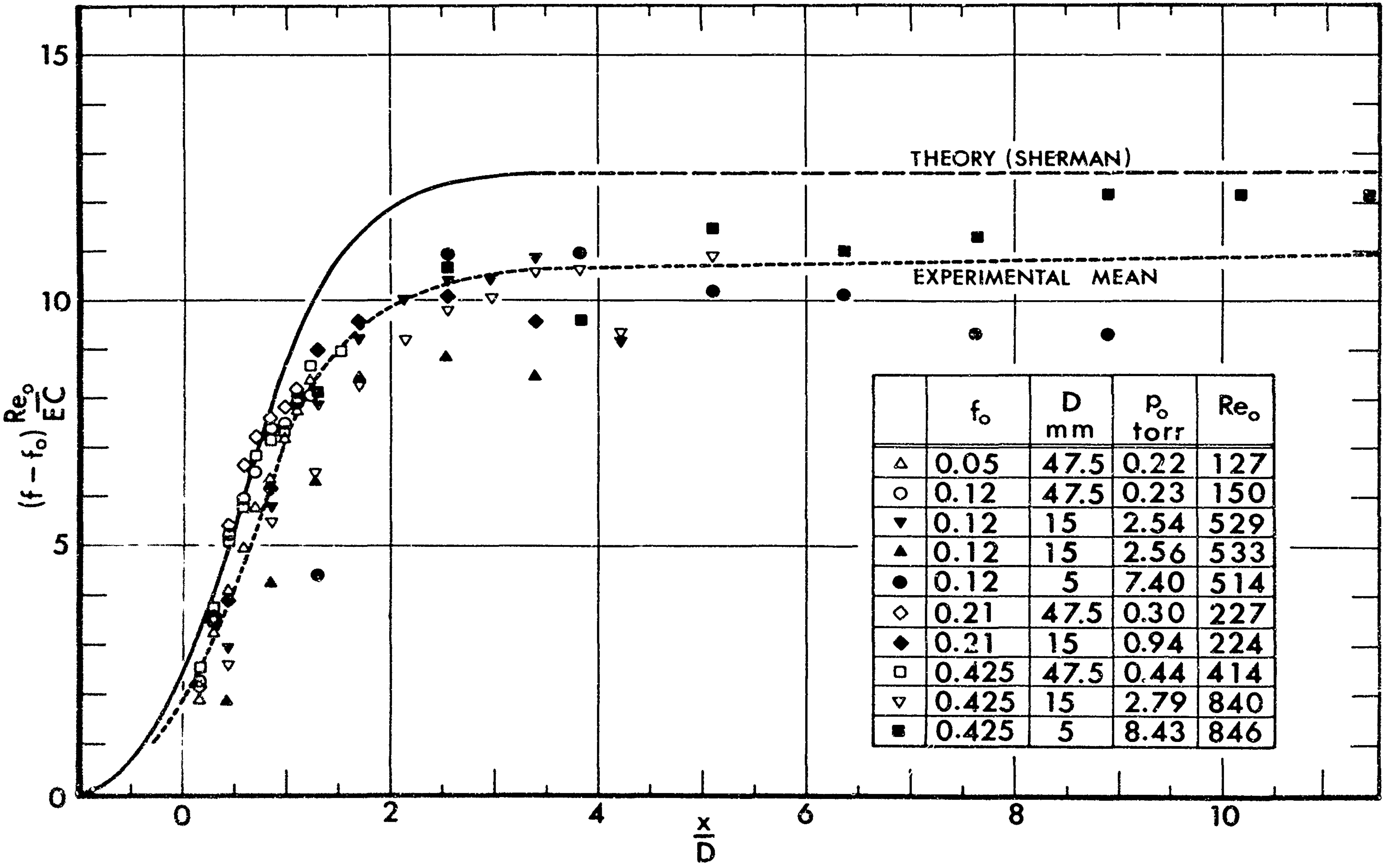

	f_o	D mm	p_o torr	Re_o
△	0.05	47.5	0.22	127
○	0.12	47.5	0.23	150
▼	0.12	15	2.54	529
▲	0.12	15	2.56	533
●	0.12	5	7.40	514
◇	0.21	47.5	0.30	227
◆	0.21	15	0.94	224
□	0.425	47.5	0.44	414
▽	0.425	15	2.79	840
■	0.425	5	8.43	846

FIG. 7 11 SUMMARY OF THE SEPARATION RESULTS ON THE AXIS OF THE FREE JET

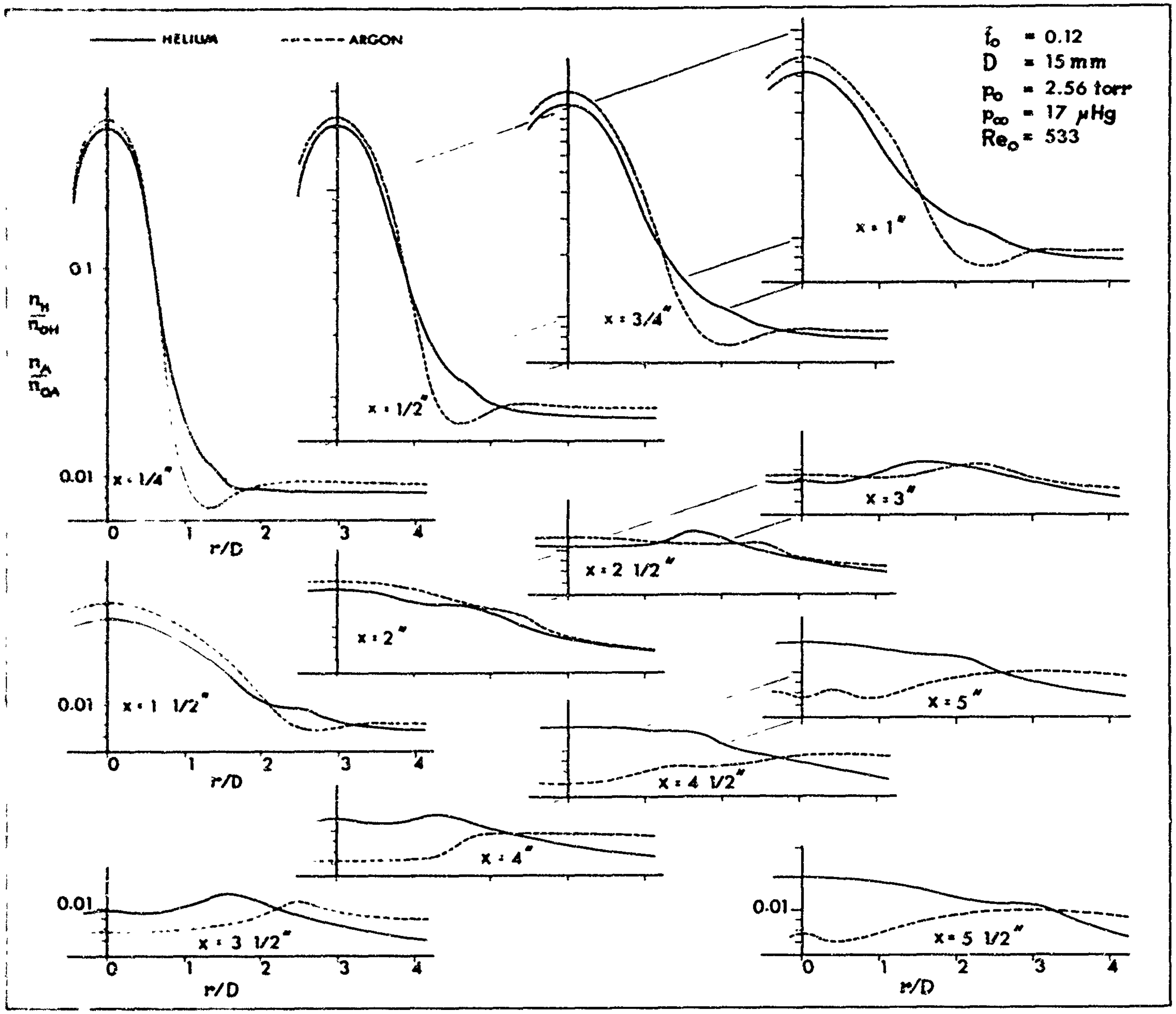

FIG. 7.12 RADIAL PARTIAL DENSITY PROFILES FOR A FREE JET OF Re_o = 533 AND f_o = 0.12

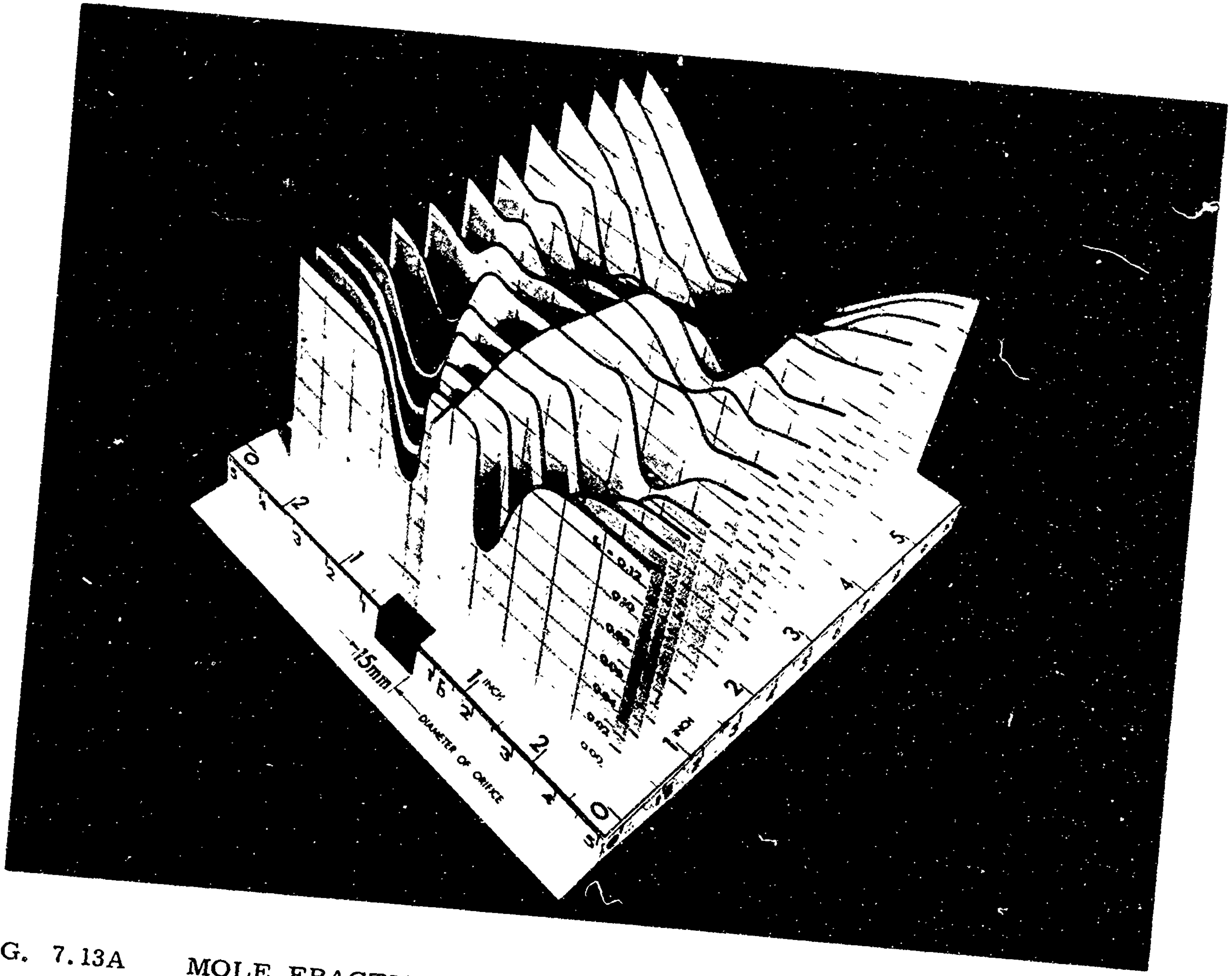

FIG. 7.13A MOLE FRACTION OF ARGON THROUGHOUT THE FLOW FIELD OF A FREE JET FOR $Re_o = 533$ AND $f_o = 0.12$ (VIEW IN DOWNSTREAM DIRECTION)

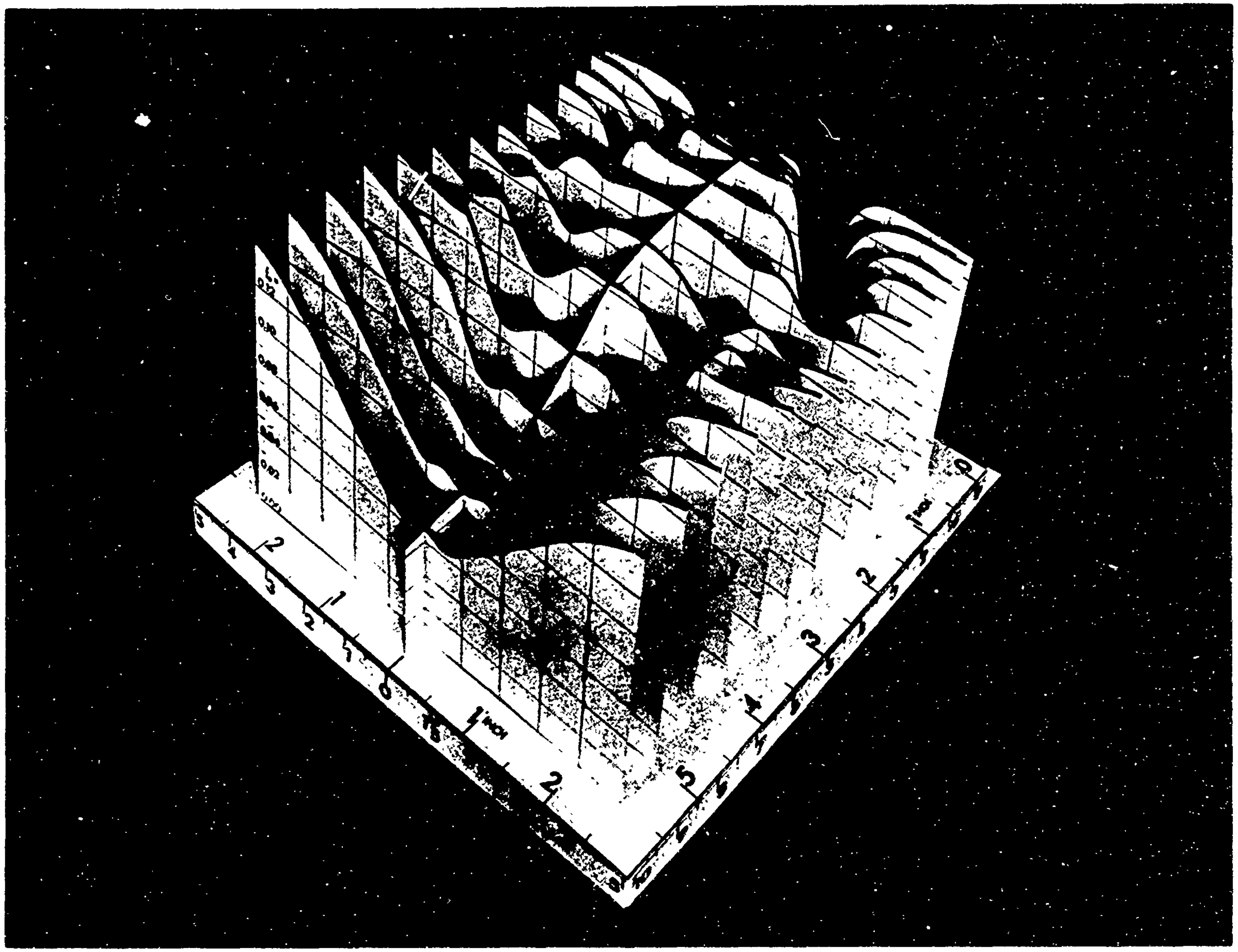

FIG. 7.13B MOLE FRACTION OF ARGON THROUGHOUT THE FLOW FIELD OF A FREE JET FOR Re_o = 533 AND f_o = 0.12 (VIEW IN UPSTREAM DIRECTION)

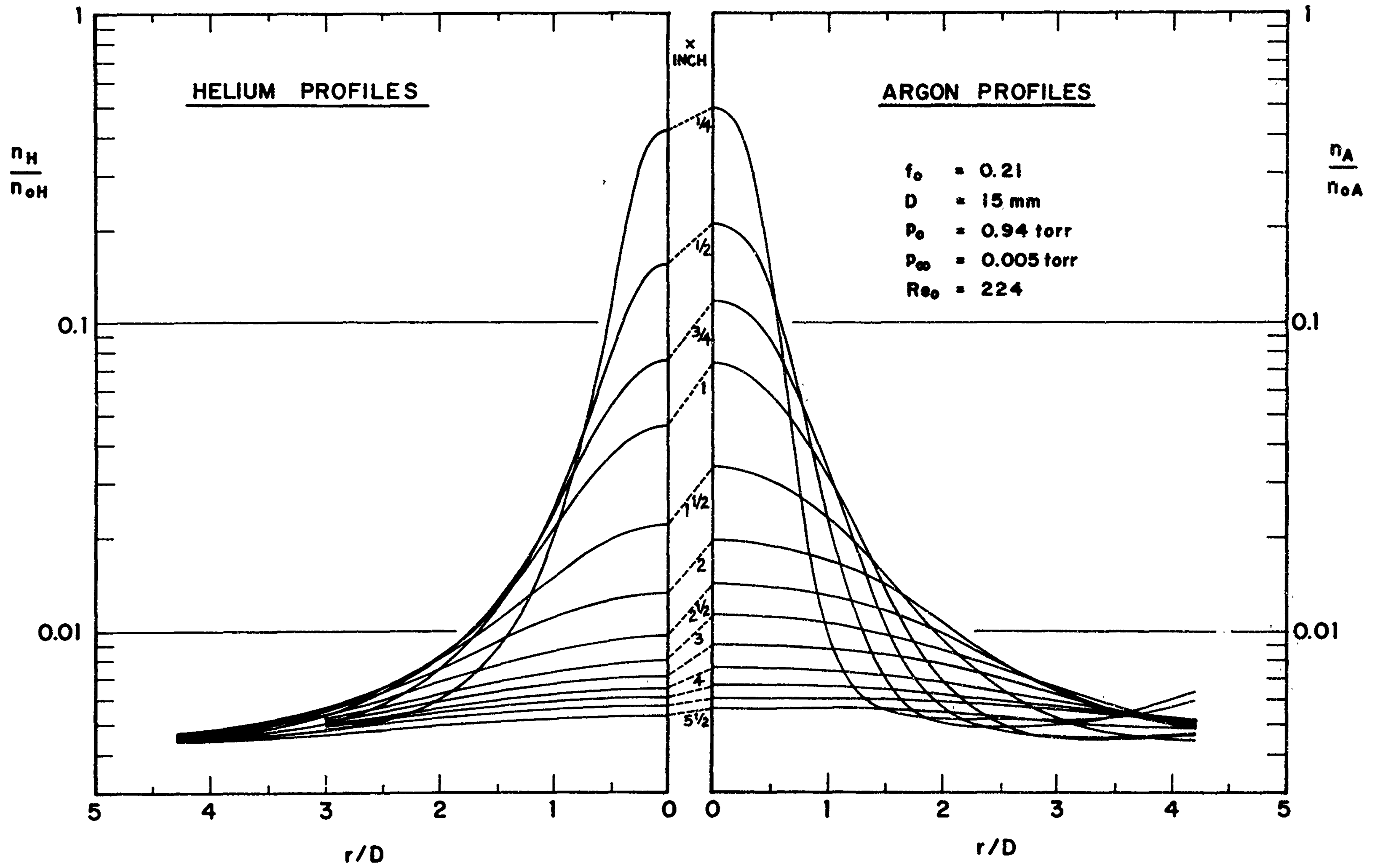

FIG. 7.14 RADIAL PARTIAL DENSITY PROFILES FOR A FREE JET OF Re_o = 224 AND f_o = 0.21

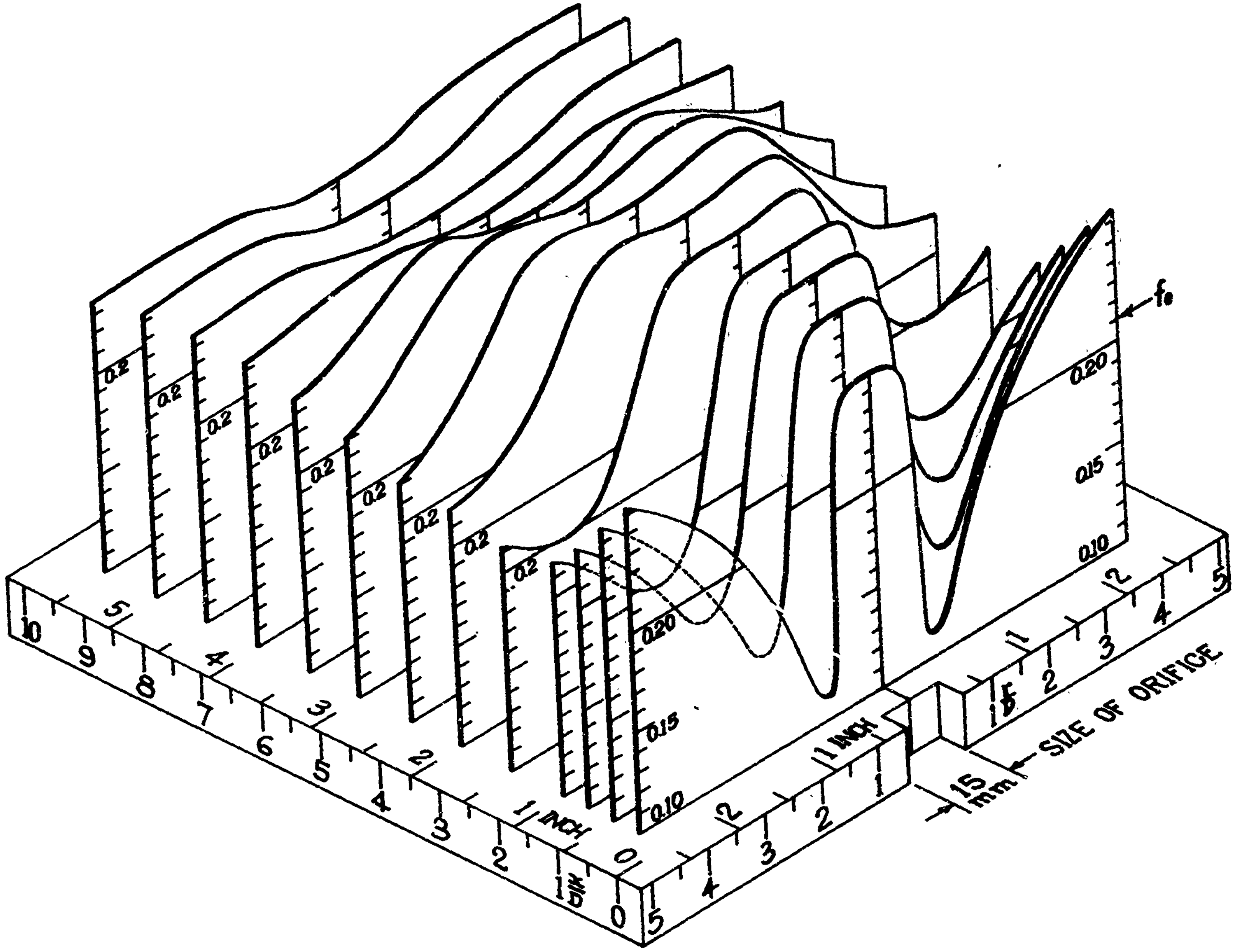

FIG. 7.15 MOLE FRACTION OF ARGON THROUGHOUT THE FLOW FIELD OF A FREE JET FOR $Re_o = 224$ AND $f_o = 0.21$

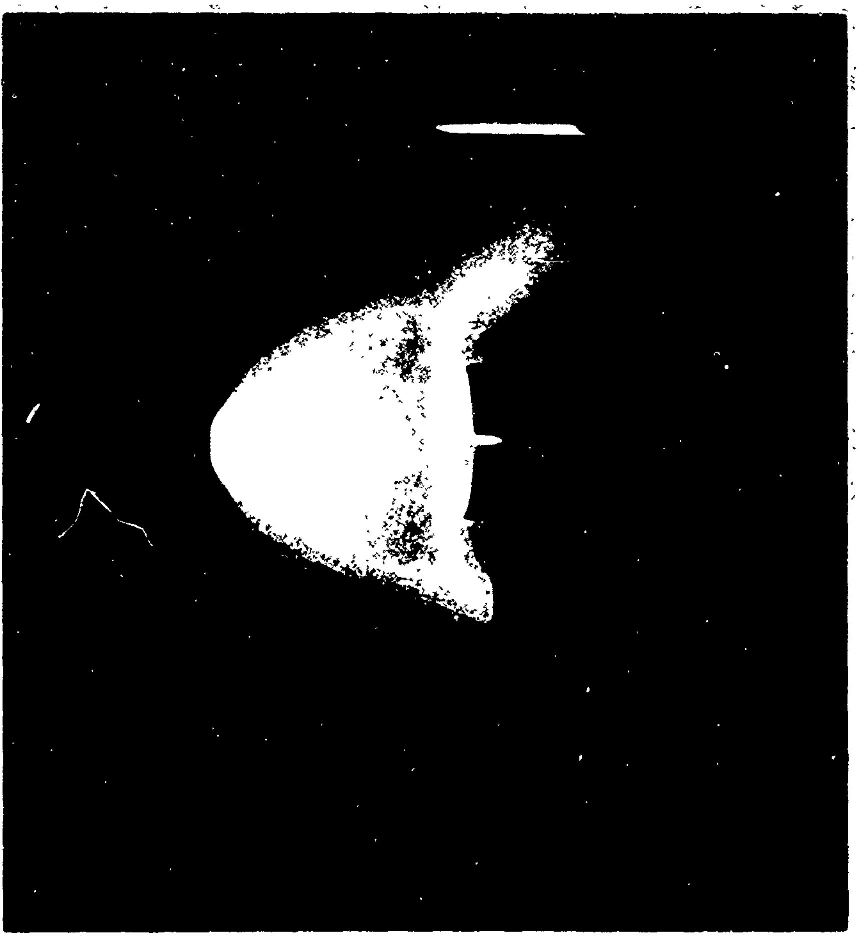

FIG. 8.1 FLOW VISUALIZATION OF A SHOCK WAVE IN FRONT OF THE SHOCK HOLDER (f_o = 0.49, $M_1 \approx 9$)

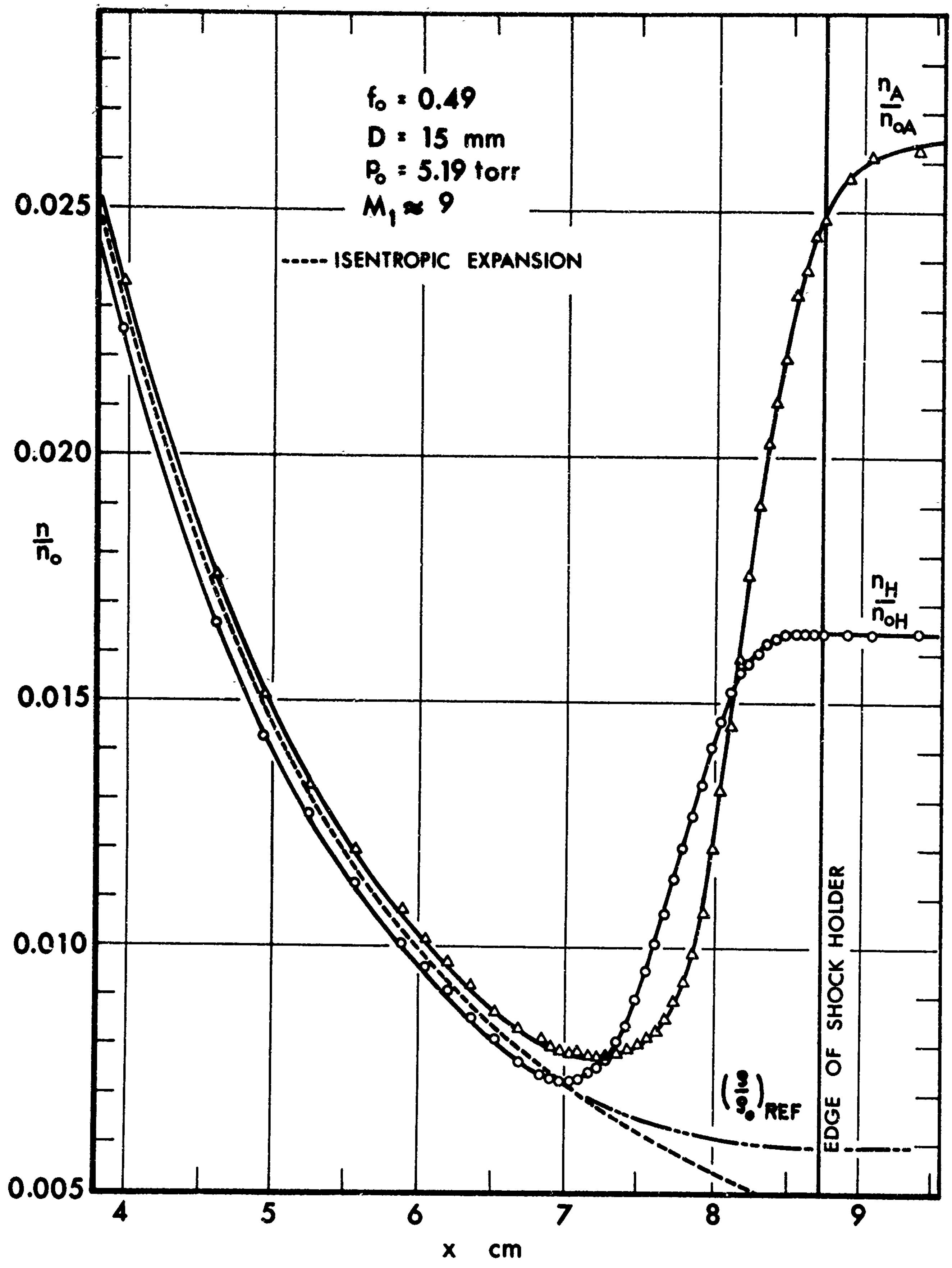

FIG. 8.2 PARTIAL DENSITY PROFILES THROUGH A MACH 9 SHOCK WAVE (f_o = 0. 9)

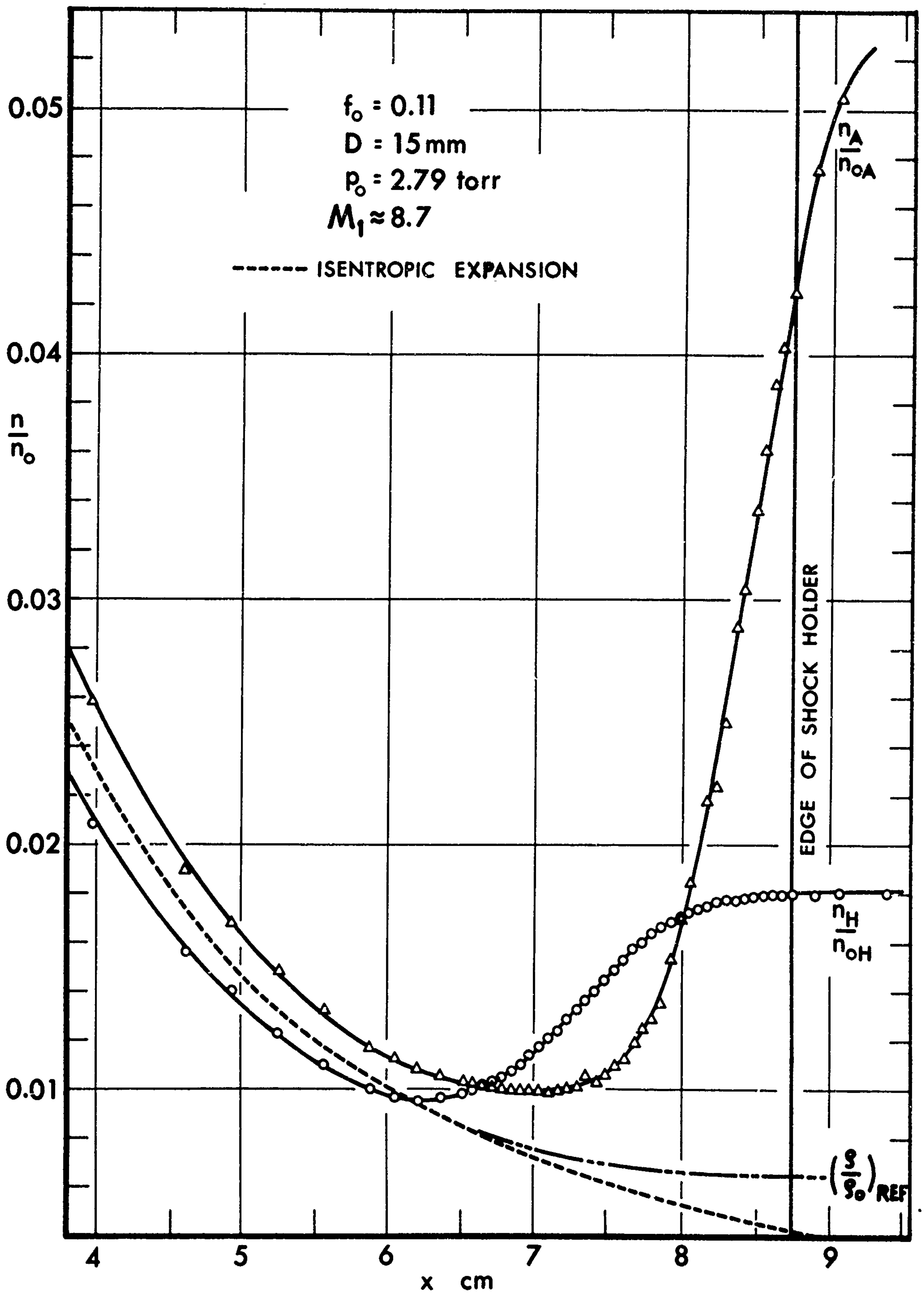

FIG. 8.3 PARTIAL DENSITY PROFILES THROUGH A MACH 8.7 SHOCK WAVE (f_o = 0.11).

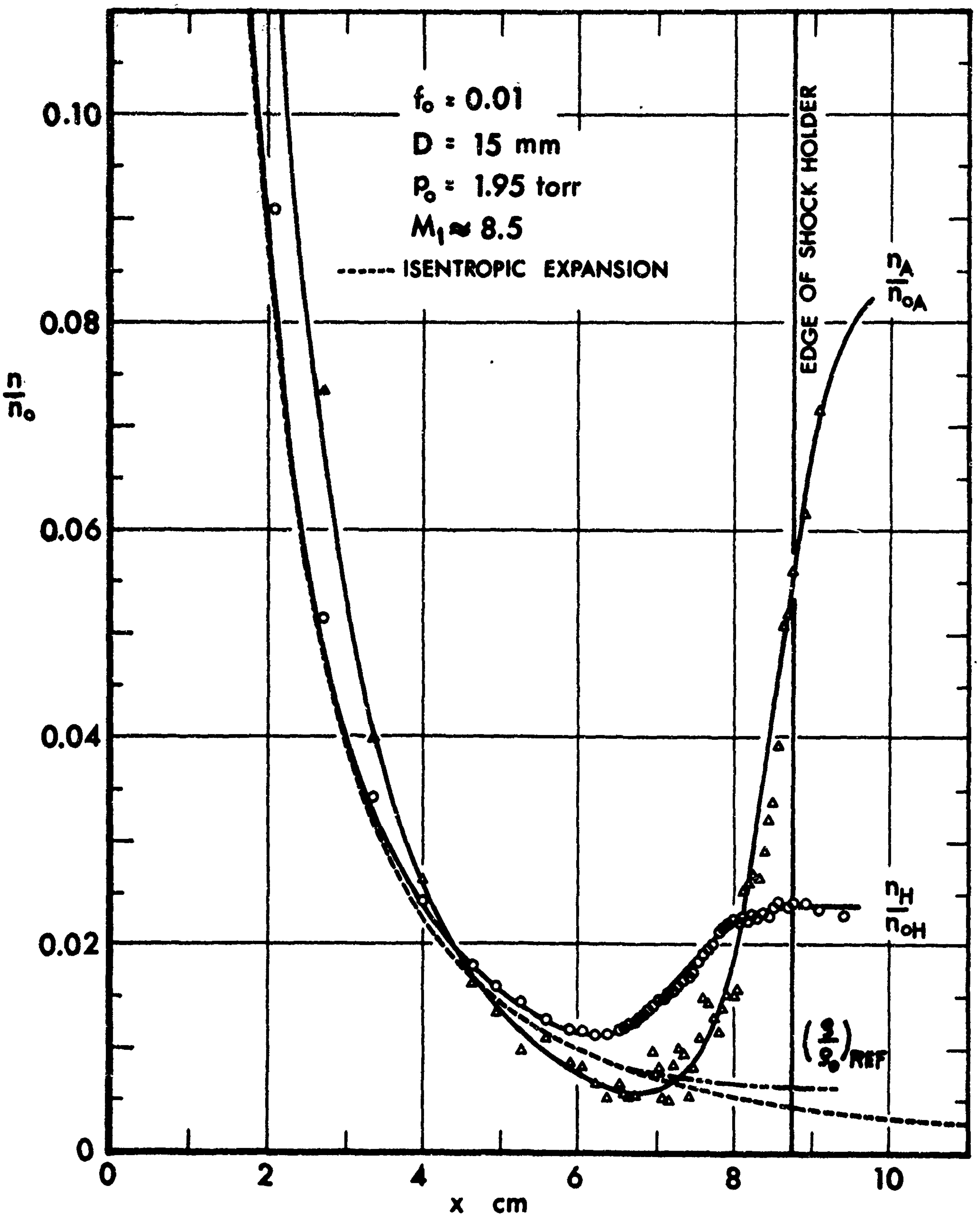

FIG. 8.4 PARTIAL DENSITY PROFILES THROUGH A MACH 8.5 SHOCK WAVE (f_o = 0.01)

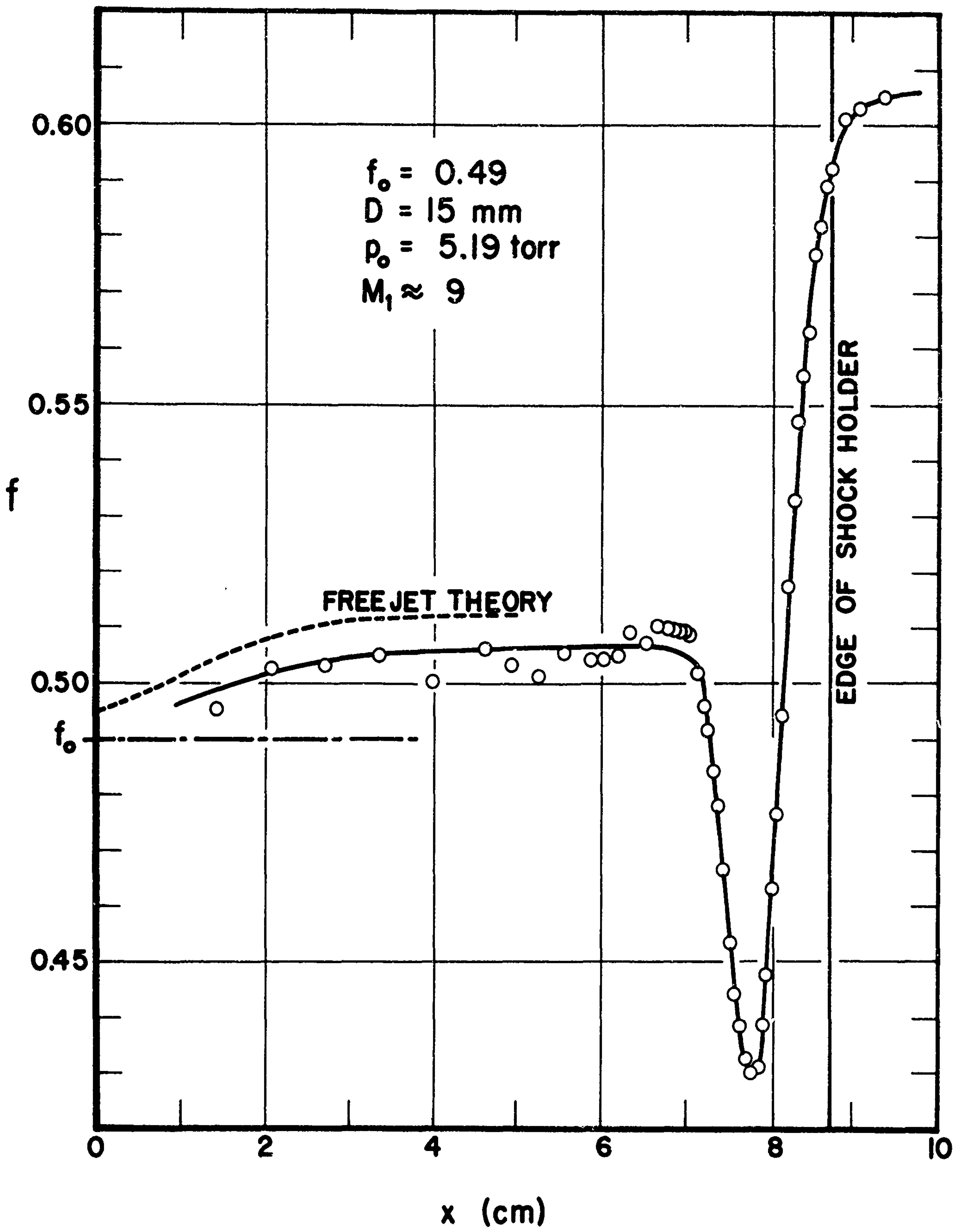

FIG. 8.5 MOLE FRACTION OF ARGON THROUGHOUT SHOCK WAVE ($f_o = 0.49$, $M_1 \approx 9$)

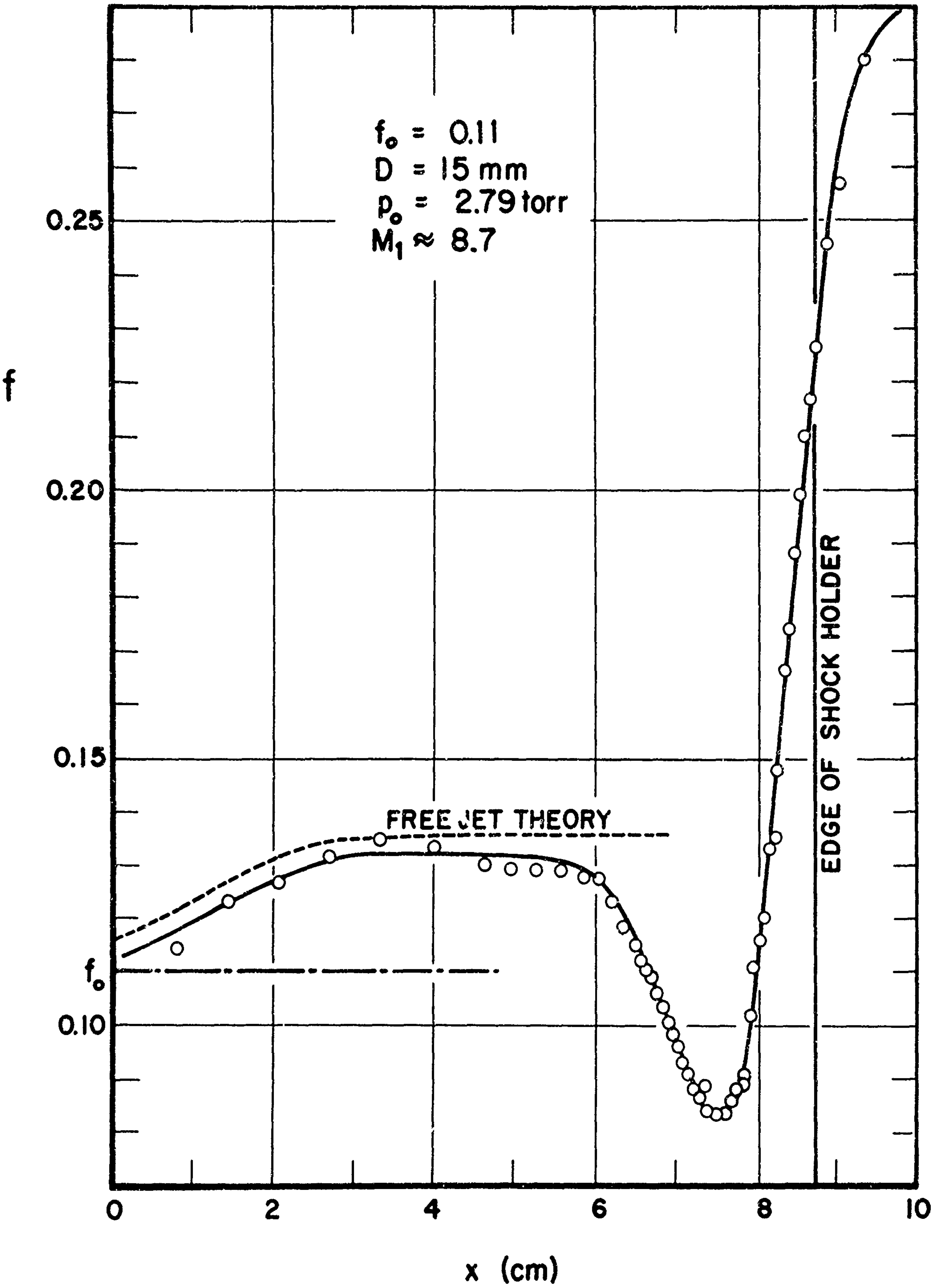

FIG. 8.6 MOLE FRACTION OF ARGON THROUGHOUT SHOCK WAVE (f_o = 0.11, $M_1 \approx$ 8.7)

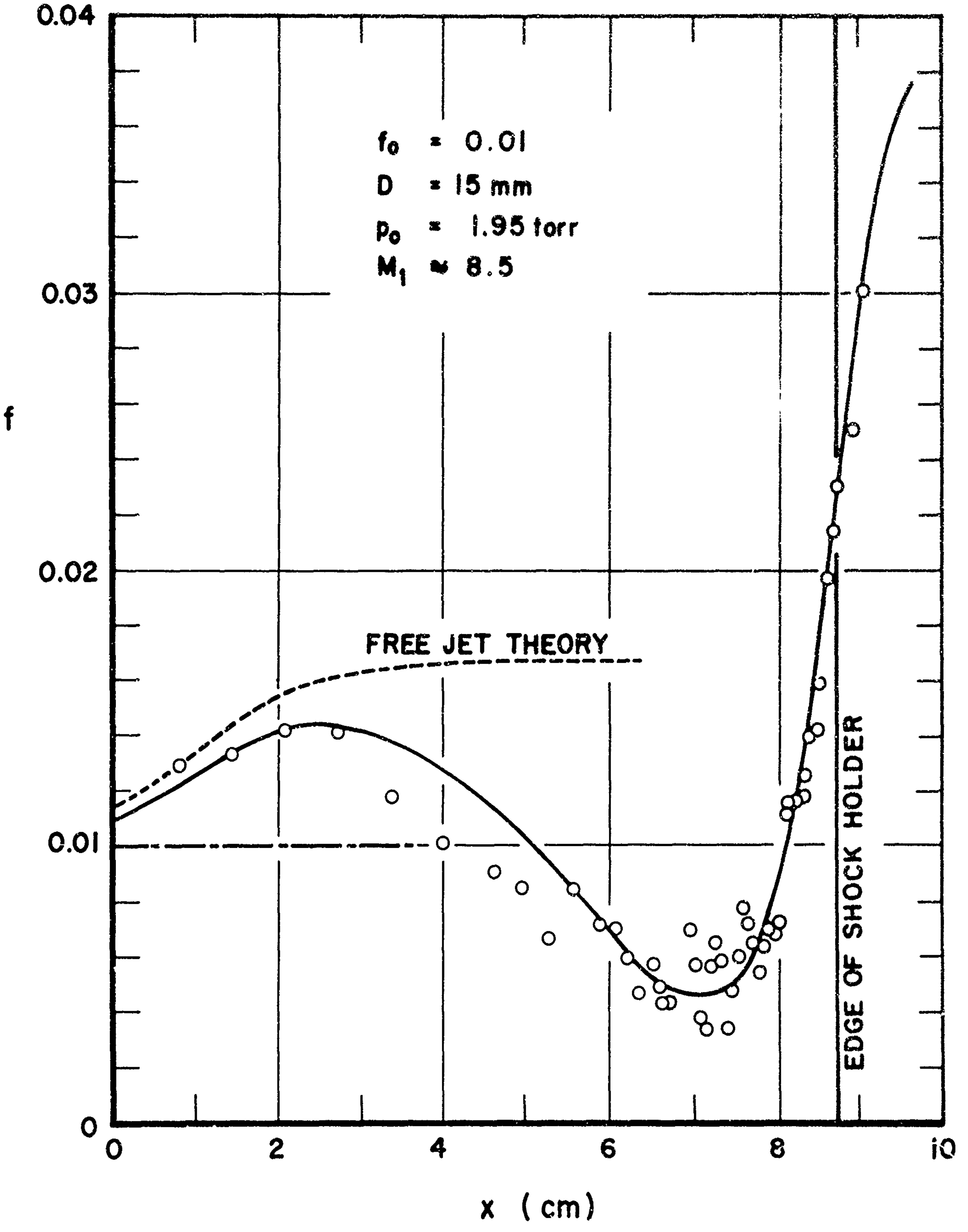

FIG. 8.7 MOLE FRACTION OF ARGON THROUGHOUT SHOCK WAVE ($f_0 = 0.01$, $M_1 \approx 8.5$)

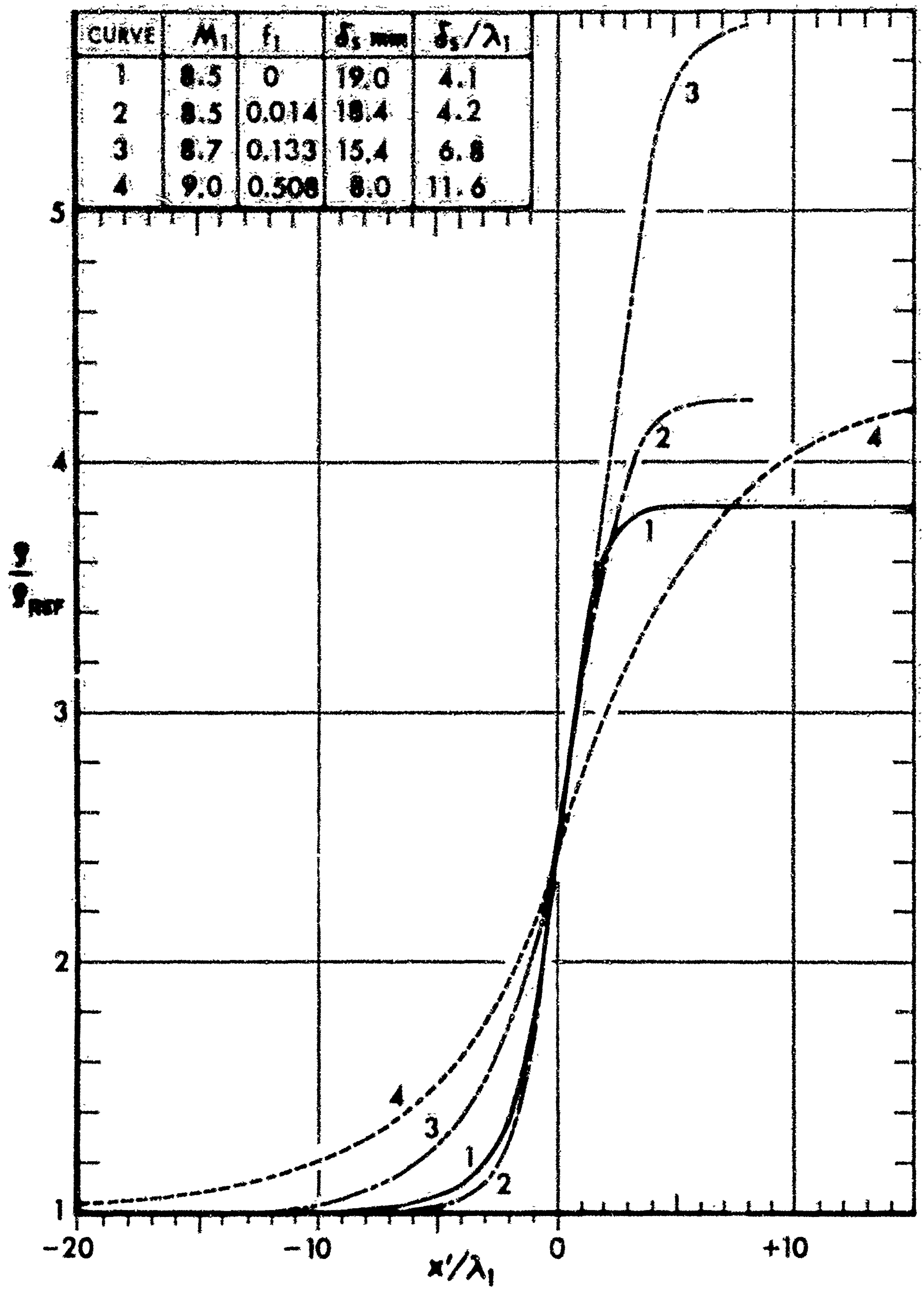

CURVE	M_1	f_1	δ_s mm	δ_s/λ_1
1	8.5	0	19.0	4.1
2	8.5	0.014	18.4	4.2
3	8.7	0.133	15.4	6.8
4	9.0	0.508	8.0	11.6

FIG. 8.8 APPROXIMATE EQUIVALENT ONE-DIMENSIONAL SHOCK PROFILES FOR THE TOTAL MASS DENSITY

APPENDIX A

Analysis of the Bottled Gas Mixtures

The majority of the free jet and shock wave experiments were performed using bottled gas mixtures. After the first free jet results were analyzed, it became clear that the percentage compositions in the supply cylinders were different from the stated values. Consequently, a quantitative analysis of the gas mixtures was performed by making use of the experimental setup available.

Several gas flow meters (floating ball in a conical tube) were calibrated for both argon and helium at 2600 torr using as a standard an "Elster, Wet-Test Model, Research Gas Meter". With the help of these calibrated flow raters pure helium and pure argon could be metered into the tunnel from separate supplies, so that any percentage composition could easily be achieved in the stagnation chamber. The flow through the flow meters was controlled by downstream needle valves, across which most of the pressure drop occurred. From there the gases flowed into a low pressure mixing chamber, which was connected to the stagnation chamber by a tube about 4 m long. In this way the gases were mixed at low pressure (15 torr.), and a good homogeneity could be expected before the gases reached the nozzle.

For the actual calibration run a 5 mm orifice (nozzle) was used, the stagnation chamber pressure was kept constant at 15 torr, and the 100 μ amp electron beam was kept at a fixed position (x = 38 mm) on the axis of the free jet emerging from the orifice. The helium and argon signals from the optical analyzer were recorded. By adjusting the amounts of helium and argon metered in, calibration curves of these photomuliplier signals versus mole fraction of argon in the source were obtained. Because of the relatively large Reynolds number of the jet (between 800 and 2000, depending on the composition) the local mole fractions of argon, calculated from the photomultiplier signals, differed only slightly from those of the input gas.

These calibration curves were then used to determine the mole fraction of argon in the bottled mixtures. The gas cylinders in question were alternately connected to the tube leading to the stagnation chamber (via a pressure regulator, a separate flow meter, and a control valve), and electron beam intensity measurements were made under exactly the same running conditions as during calibration. The helium and argon signals obtained from the optical analyzer then determined the source composition on the calibration curves (see Fig. A.1).

The nominal values of the gas mixtures and the calibrated values were as follows:

	f_o labelled	f_o calibrated
cylinder 1	0.05	0.12
cylinder 2	0.25	0.21
cylinder 3	0.50	0.425
cylinder 4	0.05	0.11
cylinder 5	0.50	0.49

Since these cylinders had been standing in the laboratory for several months before they were used, it is highly unlikely that the gases were not thoroughly mixed. The error obviously occurred during the filling operation of the cylinders (the composition had not been guaranteed by the supplier).

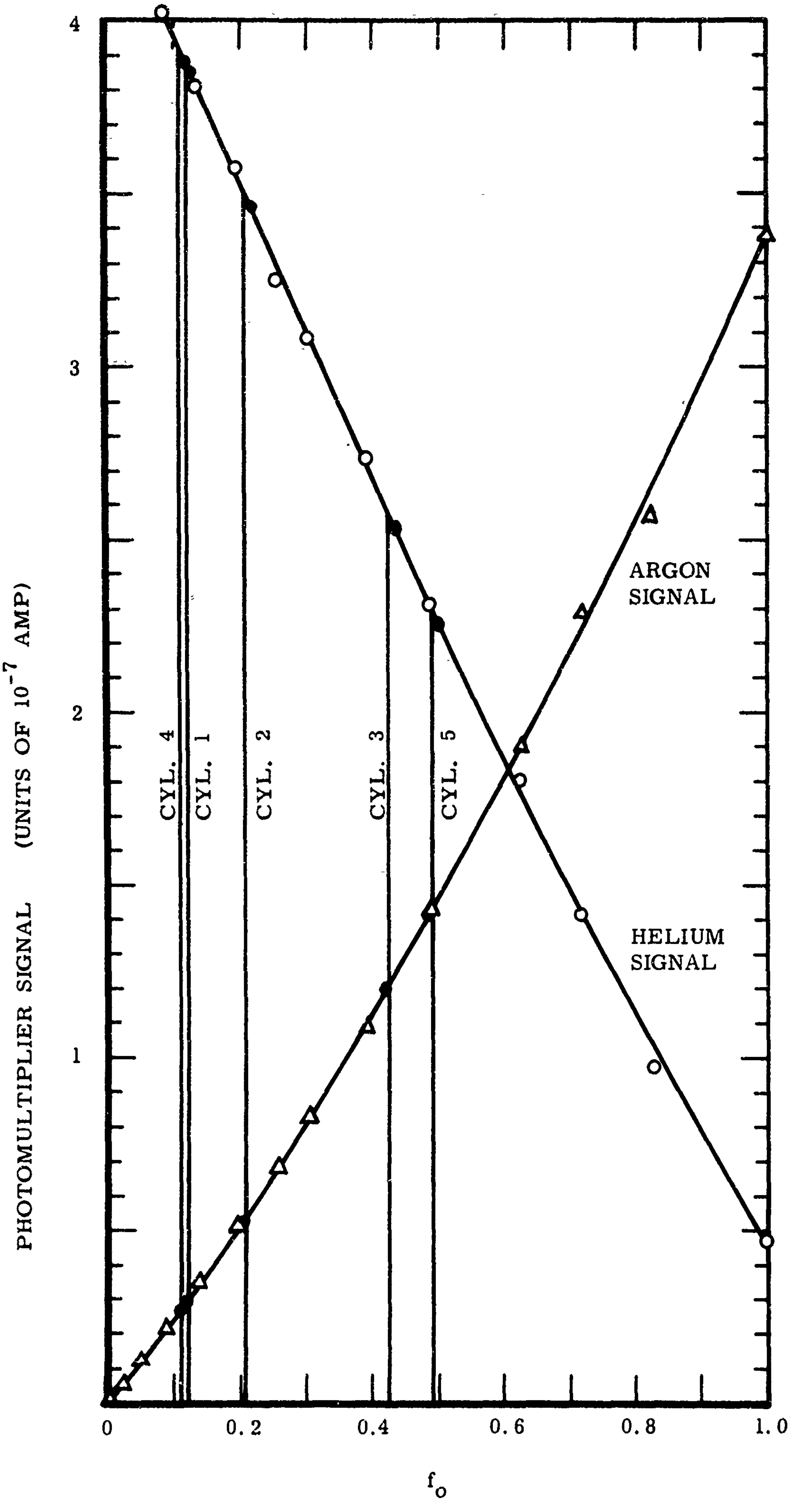

FIG. A.1 DETERMINATION OF THE COMPOSITION OF THE GAS MIXTURES IN THE GAS CYLINDERS

APPENDIX B

Equilibrium Value of f_o in the Stagnation Chamber

The equilibrium value of f_o in the stagnation chamber is equal to the mole fraction of argon in the supply cylinder (or to the volume flow fraction of argon metered into the stagnation chamber) only, if the integral of $\phi - f_o$, integrated across the total flow, is zero, i.e. if

$$\iint_S (\phi - f_o)\, dS = 0 \quad , \tag{B.1}$$

where S is any continuous surface, which is everywhere normal to the streamlines, and which crosses all streamlines going through the orifice. Because of continuity of the mass flow of each species, the surface, S, need not be identical with the sonic surface in the orifice.

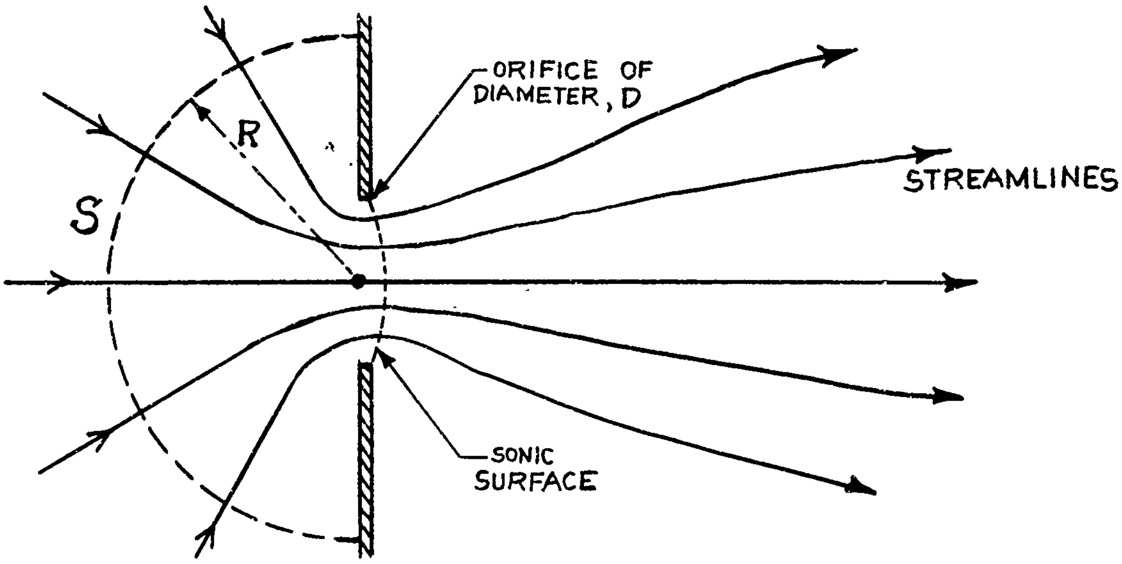

Since the helium expands through the orifice at a faster velocity than the argon, one might expect the above integral to come out negative; the positive contribution of $\phi - f_o$ on the axis being outweighed by the negative contributions from points off the axis. The following argument, however, will show that the above integral vanishes when the flow through the orifice is in the continuum regime ($Re_o > 100$).

Consider following the streamlines backwards through the orifice and into the stagnation chamber. Many orifice diameters (say, more than 10) upstream of the orifice the streamlines become almost straight, and the flow becomes spherically symmetrical and closely resembles a three-dimensional sink flow. Now let the surface, S, over which the integral is to be taken, be a hemisphere* of radius, R ($R > 10D$), centered around the orifice and projecting into the stagnation chamber. Then, by increasing R, the surface area, S, increases as R^2. If it can, therefore, be shown that at every point on this surface the quantity $\phi - f_o$ decreases faster than R^{-2}, as the hemisphere is expanded, then the integral, $\iint (\phi - f_o)\, dS$, must vanish as R becomes infinitely large. Since the surface, S, is quite arbitrary, as long as it is normal to the streamlines and extends across the total flow, the surface integral must also vanish for any permissible finite surface, in particular for the sonic surface in the orifice.

---

* or a surface as close to a hemisphere as permitted by the restrictions on S.

That $\phi - f_o$ decreases at a faster rate than R^{-2} for increasing R can be shown for the flow close to the axis by considering Eq. (16) of Ref. 8. This equation is,

$$(\phi - f_o)\frac{Re_o}{EC(\gamma-1)} = (M^2 - 1)\left(1 + \frac{\gamma-1}{2}M^2\right)^{\frac{5-3\gamma}{2(\gamma-1)}} \frac{dM}{dx} - \frac{1}{2}\int_{-\infty}^{x} \frac{(M^2-1)(3+M^2)}{M}\left(1 + \frac{\gamma-1}{2}M^2\right)^{\frac{7-5\gamma}{2(\gamma-1)}}\left(\frac{dM}{dx}\right)^2 dx \ . \qquad \text{(B.2)}$$

For $R > 10D$ the flow is in the low speed subsonic regime, and the gas behaves as an incompressible fluid. Therefore, the Mach number becomes simply proportional to the flow velocity, which, according to the continuity equation, is inversely proportional to the flow area. Hence, as $R \to \infty$ (or $x \to -\infty$), the Mach number functions occurring in Eq. (B.2) approach zero in the following way:

M decreases proportionally to $(2\pi R^2)^{-1}$; say

$$M = \frac{k}{R^2} \quad \text{, where k is a constant.}$$

Then

$$\frac{dM}{dx} = -\frac{dM}{dR} = \frac{2k}{R^3} \ ,$$

and

$$\left(\frac{dM}{dx}\right)^2 = \frac{4k^2}{R^6} \ ,$$

and

$$\int_{-\infty}^{x} \frac{1}{M}\left(\frac{dM}{dx}\right)^2 dx = -\int_{\infty}^{R} \frac{4k}{R^4}\, dR = \frac{4}{3}\ \frac{k}{R^3} \quad .$$

Equation (B.2) then becomes of the following form for $R \to \infty$.

$$(\phi - f_o)\ \frac{Re_o}{EC(\gamma-1)} \ = -\ \frac{2k}{R^3} + \frac{2k}{R^3} \equiv 0$$

The two terms in Eq. (B.2) individually decrease as R^{-3} as $R \to \infty$. Furthermore, the two terms become exactly equal and opposite in sign in the limit. It can, therefore, be said, that $f - \phi_o$ near the axis goes to zero faster than R^{-3} for R becoming large. Because of the spherical symmetry of the flow at large R, it is unlikely that the behaviour of $\phi - f_o$ can be much different from the axial behaviour in regions away from the axis.

From the above arguments it can be concluded that Eq. (B.1) is satisfied, provided the Reynolds number, Re_o, is large (say, $Re_o > 100$). The latter is the basic assumption underlying Eq. (B.2)

This means that, under these conditions, the number flow rates of argon atoms and helium atoms through the orifice are of the same ratio as the corresponding mole fractions in the stagnation chamber. Hence, the equilibrium value of f_o in the stagnation chamber is equal to the volumetric argon flow fraction metered into the tunnel, which in turn is equal to the mole fraction of argon in the supply cylinder.

APPENDIX C

Relative Thickness of the Mach Disc in a Pure Gas

In order to estimate the Mach disc thickness in terms of the jet Reynolds number and the jet pressure ratio across the orifice, it is first necessary to find the state of the gas in front of the Mach disc as a function of the stagnation chamber conditions and the ambient pressure, p_∞. A good estimate of the Mach number, M_1, in front of the Mach disc can be obtained by making the following two assumptions:

(1) The gas flowing along the axis of the free jet expands isentropically up to the Mach disc, then compresses to a pressure $p_2 > p_\infty$ through a normal shock wave.

(2) The pressure behind the Mach disc is simply related to the ambient pressure, such that $p_2 = \epsilon(\gamma) p_\infty$, where $\epsilon(\gamma)$ is independent of p_o/p_∞.

If M_1 were known, the static pressure in front of the Mach disc would then be given by the isentropic relation.

$$\frac{p_o}{p_1} = \left(1 + \frac{\gamma - 1}{2} M_1^2\right)^{\gamma/(\gamma-1)} . \tag{C.1}$$

The pressure p_1 is related to p_2 by the Rankine-Hugoniot relations for a normal shock.

$$\frac{p_2}{p_1} = \frac{2\gamma M_1^2 - \gamma + 1}{\gamma + 1} = \frac{\epsilon(\gamma)\, p_\infty}{p_1} . \tag{C.2}$$

Dividing Eq. (C.1) by Eq. (C.2) an explicit relation is obtained for the orifice pressure ratio required to achieve a Mach number, M_1, in front of the Mach disc.

$$\frac{p_o}{p_\infty} \quad \frac{\epsilon(\gamma)\left(1 + \frac{\gamma-1}{2} M_1^2\right)^{\gamma/(\gamma-1)} (\gamma+1)}{2\gamma M_1^2 - \gamma + 1} . \tag{C.3}$$

Alternately, knowing the jet pressure ratio, M_1 can be obtained from this equation. But an accurate value of M_1 can also be found independently from Wolff's calculations (Ref. 13) combined with the semi-empirical Mach disc location, given by Eq. (1) of the main text. The M_1 values obtained from Eq. (C.3), in the range $M_1 > 4$, can be brought into good agreement with those given by the characteristics solution of Wolff and Eq. (1), by simply assuming that

$$\epsilon(\gamma) = \frac{\gamma + 1}{2} . \tag{C.4}$$

There exists no direct justification for this assumption, except that it facilitates fitting Eq. (C.3) to the calculations of Wolff.

It is now possible to combine Eqs. (C.3) and (C.4) with Eq. (1) in order to obtain a semi-empirical relation for the axial variation of Mach number in the free jet. The result is,

$$\left(\frac{x}{D}\right)^2 = \frac{2(\gamma+1)^2}{9}\left(1 + \frac{\gamma-1}{2}M^2\right)^{\gamma/(\gamma-1)}\left(2\gamma M^2 - \gamma + 1\right)^{-1}$$

$$\approx \frac{(\gamma+1)^2}{9\gamma M^2}\left(1 + \frac{\gamma-1}{2}M^2\right)^{\gamma/(\gamma-1)} , \tag{C.5}$$

which agrees quite well with Wolff's results for $x/D > 2$.

Using the isentropic relations to eliminate M from Eq. (C.5), the state of the gas is found in terms of the stagnation state for any point on the jet axis. For $x/D > 2$ one may thus write

$$\frac{\rho}{\rho_o}\left[1 - \left(\frac{\rho}{\rho_o}\right)^{\gamma-1}\right] = \left(\frac{T}{T_o}\right)^{1/(\gamma-1)}\left[1 - \frac{T}{T_o}\right]$$

$$= \left(\frac{p}{p_o}\right)^{1/\gamma}\left[1 - \left(\frac{p}{p_o}\right)^{\frac{\gamma-1}{\gamma}}\right] \tag{C.6}$$

$$= \frac{(\gamma+1)^2(\gamma-1)}{18\gamma\,(x/D)^2} .$$

Far downstream of the orifice the static temperature becomes very much smaller than T_o, and Eq. (C.6) can be written as

$$\frac{\rho}{\rho_o} = \left(\frac{p}{p_o}\right)^{1/\gamma} = \left(\frac{T}{T_o}\right)^{1/(\gamma-1)} = \frac{(\gamma+1)^2(\gamma-1)}{18\gamma\,(x/D)^2} , \tag{C.7}$$

which is valid only at large x/D.

Equation (C.7) predicts that at high Mach numbers, many orifice diameters away from the orifice, the gas density decreases inversely as the square of the distance from the orifice. This is in agreement with Sherman's source flow model (Refs. 13 and 15), which predicts

$$\frac{\rho}{\rho_o} = B\left(\frac{x-x_o}{D}\right)^{-2} \quad ; \quad x_o = \text{location of hypothetical source near the orifice,}$$

which for large x/D goes to

$$\frac{\rho}{\rho_o} = B\left(\frac{x}{D}\right)^{-2} ,$$

where the constant, B, is chosen such as to fit Wolff's data. As will be seen from the following table, the values of B are reasonably well predicted by Eq. (C.7)

γ	B (Sherman)	$(\gamma+1)^2(\gamma-1)/18\gamma$
5/3	0.161	0.158
7/5	0.0893	0.0915
9/7	0.0615	0.0645

The Mach disc thickness can now be estimated using Eq. (C.7), if it can be assumed that x_M/D is large. In this case M_1 is of the order of 10 or larger. Experimental shock thicknesses in this range are about equal to 4.5 mean free paths ahead of the shock (see e.g. Ref. 34). Therefore, let the Mach disc thickness be

$$\delta = 4.5 \ \lambda_1 \quad . \tag{C.8}$$

But,

$$\lambda_1 = \frac{16}{5}\left(\frac{\gamma}{2\pi}\right)^{\frac{1}{2}} \mu_1/\rho_1 \, a_1 \quad . \tag{14}$$

Therefore,

$$\delta = \frac{72}{5}\left(\frac{\gamma}{2\pi}\right)^{\frac{1}{2}} \mu_1/\rho_1 \, a_1$$

$$= \frac{72}{5}\left(\frac{\gamma}{2\pi}\right)^{\frac{1}{2}} Re_o^{-1}(\mu_1/\mu_o)(a_o/a_1)(\rho_o/\rho_1)D.$$

Using now Eq. (C.7) and $\mu_1/\mu_o = (T_1/T_o)^{\nu}$, this equation can be re-written as

$$\frac{\delta}{x_M} = \frac{1296}{5\sqrt{2\pi}} \quad \frac{\gamma^{3/2}}{(\gamma+1)^2(\gamma-1)} \, Re_o^{-1} \left(\frac{T_1}{T_o}\right)^{\nu-\frac{1}{2}}\left(\frac{x_M}{D}\right) .$$

Substituting Eq. (1) and assuming $\nu = 1/2$ the relative Mach disc thickness becomes

$$\frac{\delta}{x_M} = 69 \quad \frac{\gamma^{3/2}}{(\gamma+1)^2(\gamma-1)} \quad Re_o^{-1}\left(\frac{p_o}{p_\infty}\right)^{1/2} . \tag{13}$$

Security Classification

DOCUMENT CONTROL DATA - R&D

(Security classification of title, body of abstract and indexing annotation must be entered when the overall report is classified)

1. ORIGINATING ACTIVITY *(Corporate author)* Institute for Aerospace Studies, University of Toronto, Toronto 5, Ontario	**2a. REPORT SECURITY CLASSIFICATION** Unclassified **2b. GROUP**

3. REPORT TITLE

ELECTRON BEAM STUDIES OF THE DIFFUSIVE SEPARATION OF HELIUM-ARGON MIXTURES IN FREE JETS AND SHOCK WAVES

4. DESCRIPTIVE NOTES *(Type of report and inclusive dates)*

UTIAS Technical Report

5. AUTHOR(S) *(Last name, first name, initial)*

D. E. Rothe

6. REPORT DATE July 1966	**7a. TOTAL NO. OF PAGES** 96	**7b. NO. OF REFS** 39

8a. CONTRACT OR GRANT NO. AF AFOSR 276-65 **b. PROJECT NO.** **c.** **d.**	**9a. ORIGINATOR'S REPORT NUMBER(S)** UTIAS Report No. 114 **9b. OTHER REPORT NO(S)** *(Any other numbers that may be assigned this report)*

10. AVAILABILITY/LIMITATION NOTICES

Institute for Aerospace Studies,
University of Toronto, Toronto 5, Ont.

11. SUPPLEMENTARY NOTES	**12. SPONSORING MILITARY ACTIVITY** Air Force Office of Scientific Research SREM

13. ABSTRACT

A narrow electron beam was used to selectively determine the component densities in rarefied helium-argon flows by spectrally analyzing the beam's luminescence. After a systematic study of the electron beam fluorescence in helium and argon had been made in a series of preliminary experiments, point-by-point measurements were made along and off the axes of underexpanded free jets and through normal shock waves produced by shock holders placed in the jets. Various argon mole fractions were used, and the jet Reynolds numbers ranged from 100 to 10,000. The argon enrichment found along the jet axis agrees well with a theory recently proposed by F.S. Sherman. Off axis tests show an argon deficiency near the jet boundary. The experimental shock profiles agree only qualitatively with one-dimensional theories. Radial diffusion destroyed the otherwise approximate one-dimensionality of the shock waves, resulting in a significant argon enrichment inside the partially stagnated shock holder.

DD FORM 1 JAN 64 1473

Security Classification

14. KEY WORDS	LINK A		LINK B		LINK C	
	ROLE	WT	ROLE	WT	ROLE	WT
Diffusive separation						
Free Jet						
Argon-helium mixtures						
Electron beam densitometer						
Shock mixture						

INSTRUCTIONS

1. ORIGINATING ACTIVITY: Enter the name and address of the contractor, subcontractor, grantee, Department of Defense activity or other organization *(corporate author)* issuing the report.

2*a*. REPORT SECURITY CLASSIFICATION: Enter the overall security classification of the report. Indicate whether "Restricted Data" is included. Marking is to be in accordance with appropriate security regulations.

2*b*. GROUP: Automatic downgrading is specified in DoD Directive 5200.10 and Armed Forces Industrial Manual. Enter the group number. Also, when applicable, show that optional markings have been used for Group 3 and Group 4 as authorized.

3. REPORT TITLE: Enter the complete report title in all capital letters. Titles in all cases should be unclassified. If a meaningful title cannot be selected without classification, show title classification in all capitals in parenthesis immediately following the title.

4. DESCRIPTIVE NOTES: If appropriate, enter the type of report, e.g., interim, progress, summary, annual, or final. Give the inclusive dates when a specific reporting period is covered.

5. AUTHOR(S): Enter the name(s) of author(s) as shown on or in the report. Enter last name, first name, middle initial. If military, show rank and branch of service. The name of the principal author is an absolute minimum requirement.

6. REPORT DATE: Enter the date of the report as day, month, year; or month, year. If more than one date appears on the report, use date of publication.

7*a*. TOTAL NUMBER OF PAGES: The total page count should follow normal pagination procedures, i.e., enter the number of pages containing information.

7*b*. NUMBER OF REFERENCES: Enter the total number of references cited in the report.

8*a*. CONTRACT OR GRANT NUMBER: If appropriate, enter the applicable number of the contract or grant under which the report was written.

8*b*, 8*c*, & 8*d*. PROJECT NUMBER: Enter the appropriate military department identification, such as project number, subproject number, system numbers, task number, etc.

9*a*. ORIGINATOR'S REPORT NUMBER(S): Enter the official report number by which the document will be identified and controlled by the originating activity. This number must be unique to this report.

9*b*. OTHER REPORT NUMBER(S): If the report has been assigned any other report numbers *(either by the originator or by the sponsor)*, also enter this number(s).

10. AVAILABILITY/LIMITATION NOTICES: Enter any limitations on further dissemination of the report, other than those imposed by security classification, using standard statements such as:

(1) "Qualified requesters may obtain copies of this report from DDC."

(2) "Foreign announcement and dissemination of this report by DDC is not authorized."

(3) "U. S. Government agencies may obtain copies of this report directly from DDC. Other qualified DDC users shall request through

____________________________________ ."

(4) "U. S. military agencies may obtain copies of this report directly from DDC. Other qualified users shall request through

____________________________________ ."

(5) "All distribution of this report is controlled. Qualified DDC users shall request through

____________________________________ ."

If the report has been furnished to the Office of Technical Services, Department of Commerce, for sale to the public, indicate this fact and enter the price, if known.

11. SUPPLEMENTARY NOTES: Use for additional explanatory notes.

12. SPONSORING MILITARY ACTIVITY: Enter the name of the departmental project office or laboratory sponsoring *(paying for)* the research and development. Include address.

13. ABSTRACT: Enter an abstract giving a brief and factual summary of the document indicative of the report, even though it may also appear elsewhere in the body of the technical report. If additional space is required, a continuation sheet shall be attached.

It is highly desirable that the abstract of classified reports be unclassified. Each paragraph of the abstract shall end with an indication of the military security classification of the information in the paragraph, represented as *(TS)*, *(S)*, *(C)*, or *(U)*.

There is no limitation on the length of the abstract. However, the suggested length is from 150 to 225 words.

14. KEY WORDS: Key words are technically meaningful terms or short phrases that characterize a report and may be used as index entries for cataloging the report. Key words must be selected so that no security classification is required. Identifiers, such as equipment model designation, trade name, military project code name, geographic location, may be used as key words but will be followed by an indication of technical context. The assignment of links, rules, and weights is optional